INVESTIGATION OF TOKAMAK

SOLID DIVERTOR TARGET OPTIONS

by

J. McMurray
N. Todreas
B. Mikic
P. Gierszewski

PFC/RR - 81 - 23

INVESTIGATION OF TOKAMAK

SOLID DIVERTOR TARGET OPTIONS

by

JOHN M. MCMURRAY

Submitted to the Department of Nuclear Engineering on May 26, 1981 in partial fulfillment of the requirements for the Degrees of Master of Science in Nuclear Engineering and Master of Science in Mechanical Engineering

ABSTRACT

Analysis of survival constraints on the design of solid targets for tokamak bundle divertors is presented. Previous target design efforts are reviewed. Considerations of heat removal, surface erosion, and fatigue life are included in a generalized design window methodology which facilitates target selection. Using subcooled water as coolant, eight possible target materials are evaluated for use in tubular and plate targets as substrates, coatings, and claddings. Subject to the severe environment of the tokamak plasma, the most promising conventional designs are identified. A thermally bonded, mechanically unbonded laminated design is proposed and evaluated as a target design well suited to the divertor target environment. Due to fatigue and sputtering erosion this configuration has limited life, but appears to constitute an upper bound for the capabilities of a solid target design. Needs for experimental work are identified.

Thesis Supervisor: Prof. Neil E. Todreas

ACKNOWLEDGEMENT

The author appreciates the patience and assistance of the many who have helped make this project possible. In particular, the wisdom and suggestions of my advisors, Professor B.B. Mikic and Professor N.E. Todreas, were priceless aids. The vigor, insight, and helpfulness of Paul Gierszewski knows no equal. Ted Yang and Bruce Montgomery offered support and key direction in the formulation of this project.

TABLE OF CONTENTS

	Title Page	1
	Abstract	2
	Acknowledgement	3
	Table of Contents	4
	Nomenclature	6
I.	Introduction	7
	A. Functions of Divertor	7
	B. Focus of Work	10
	C. Summary of Other Divertor Work to Date	12
	D. Base Case Parameters	15
II.	Thermo-Hydraulics	17
	A. Coolant Survey	17
	B. Determination of Applicable CHF Correlations	17
	C. Pressure Drop Limitations	23
	D. Heat Transfer Coefficient	27
	E. Swirl and Mixed Flow Schemes	28
	F. Effect of Asymmetric Heating	29
III.	Surface Interactions	39
	A. Sputtering and Plasma Contamination	39
	B. Internal Erosion	42
IV.	Thermo-Mechanics	49
	A. Pressure Stress	49
	B. Thermal Stress	50
	C. Fatigue	51
	D. Thermal Shock	54
	E. Temperature Limits	55
	F. Graphical Materials Data	56
V.	Evaluation of Design Options	67
	A. Possible Geometries	67
	B. Materials	67
	1. Functional Requirements	67
	2. Limits of Data Base	68
	C. Particle Load vs. Lifetime Tradeoff	68
	D. Single Material Analysis	70
	1. Tube Design	70
	2. Plate Design	72
	E. Composite Material Analysis	73
	1. Coated Tube Design	73
	2. Armored Plate Design	75

3. Mechanically Unbonded Layered Plate Design 77

VI. Sensitivity Analysis 92
A. Pulse Length and Fatigue Constraint 92
B. Sputtering Characteristics 93
C. CHF Limit 94
D. Pumping Power Limit 95
E. Inlet Temperature 96
F. Pressure 96
G. Tube Length 97
H. Thickness 97
I. Heat Flux 98

VII. Conclusions 109

VIII. Recommendations 111

References 113

Appendix A: Materials Properties 118

Appendix B: Methodology Summary 121

NOMENCLATURE

a_t	Thermal diffusivity
a	Tube inner radius
b	Tube outer radius
c_p	Specific heat
C	Target capacity factor (fraction of year exposed to plasma)
D	Channel hydraulic diameter
E	Modulus of elasticity
f	Friction factor
g_c	Gravitation constant
G	Mass flux
h	Heat transfer coefficient
h_{fg}	Enthalpy of evaporation
I_{max}	Max allowable impurity in plasma (%)
J_i	Particle flux for i'th isotope
k	Thermal conductivity
k_B	Boltzmann's constant
L	Channel length
m	Mass
$\dot{m}$	Mass flow rate
M	Atomic weight
N	Particle current
N_A	Avogadro's Number
p	Pressure
P	Power
q"	Heat flux
r	Channel inner radius
S_i	Sputtering coefficient (atom/ion)
S_{mt}	Allowable stress intensity
S.F.	CHF safety factor
t	Wall thickness
T	Temperature
T_i	Ion Temperature
T_{in}	Fluid inlet Temperature
ΔT_{1-2}	Temperature rise in coolant from inlet to outlet
V	Coolant velocity
W_p	Pumping power to heat transfer ratio
y	Tape twist ratio (inside dia./ 180° twist)
α	Thermal expansion coefficient
ϵ	Strain
θ	Angle from normal
μ	Viscosity
ν	Poisson's ratio
ρ	Density
σ	Stress
τ	Time
ω	Period of heat load oscillation

Subscripts:

b	Bulk fluid
c	Critical
s	Surface
w	Fluid at wall temperature

I. INTRODUCTION

A. Functions of the Divertor

In order to advance toward eventual commercial power output from tokamak fusion machines, methods must be devised to permit uninterrupted operation of devices over long periods of time. Only in this way can reliable and steady electrical energy be supplied to the distribution grid. Current experimental machines are capable of fusion pulses of durations less than one second. Pulse duration is presently limited by the flux swing in the magnet power supply. If this obstacle can be overcome, two secondary limits on extending the pulse duration result from (a) the generation by the fusion process of helium, which quenches the plasma burn by displacing hydrogen fuel, and from (b) the sputtering of impurity atoms from the chamber first wall, which quench the plasma by greatly enhanced line radiation. An additional related constraint is the damage sustained by the first wall itself due to sputtering, necessitating frequent and costly refurbishment.

The development of the divertor provides a potential remedy for these problems. In general, a divertor must serve as both a "helium exhaust" system and an "impurity-filter" system for the tokamak plasma. An outer sheath of the toroidal plasma column is magnetically diverted

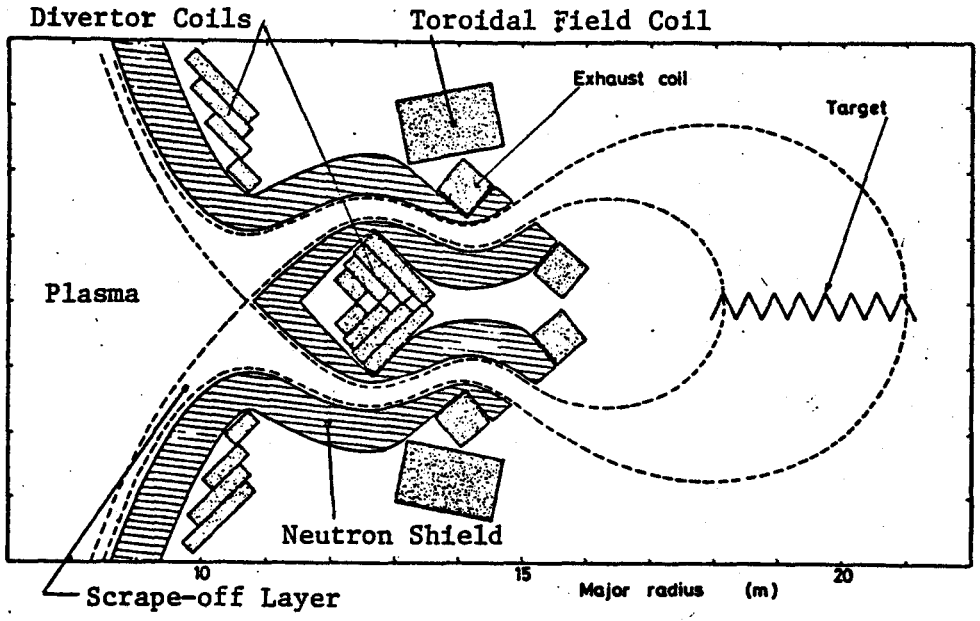

Figure I-1: Horizontal section of bundle divertor showing two additional exhaust coils to expand the diverted flux bundle. (Ref. 1)

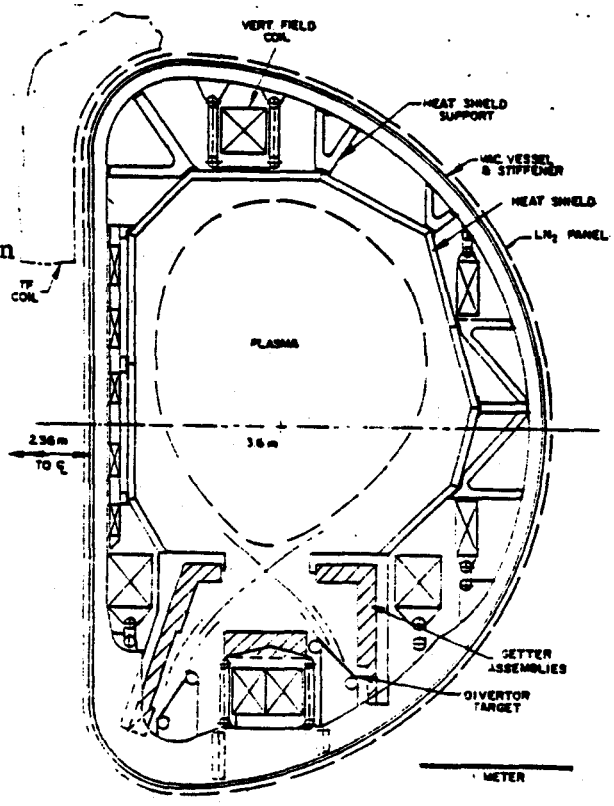

Figure I-2: Vertical section showing single null poloidal divertor, coil and structure detail.

to a separate chamber, where these vital particle handling functions may be undertaken by impingement on an appropriate target. (See Figs. I-1,I-2.) Helium is continuously collected as it diffuses outward from the reacting plasma core; impurities are filtered before they can penetrate to the energetic core, and the rate of damage to the chamber first wall is significantly reduced. The reason for a divertor's existence, then, is this particle handling function. Numerous methods have been proposed to carry out this task, including chemical and mechanical gettering, diffusion of light atoms through metals, and neutral gas pumping. Each method implies use of some target machanism which intercepts the diverted plasma.

The environment in which the divertor target must perform will be extremely severe. Though estimates vary, heat loads on the order of 1 kw/cm^2, particle loads of 10^{22} $particles/m^2$-sec, and particle energies from 1 to 10 keV are anticipated to impinge on the target. In order to permit economical long term operation of the fusion device, the system must be designed to avoid excessive down times for target refurbishment. The McDonnell-Douglas study of tokamak maintainability suggests a minimum period between maintenance shutdowns of one year as essential to fusion's economic viability.(Ref. 2) Thus, a prerequisite to fulfilling the particle handling

function is the ability to survive the extreme environment for at least a one year period. To facilitate development of a workable divertor target, designs which appear to have adequate longevity will be sought. The particle handling function can then be added to a sufficiently durable target. This decoupling of energy absorption from particle handling may prove attractive in future designs.

B. Focus of Work

While possibilities for divertor target design include novel concepts such as liquid targets, gas targets, and curtains of moving pellets, (see Ref. 3) the conventional design encompasses a solid target material which acts at a minimum to absorb energy, and possibly also to trap particles. This paper will concentrate on various arrangements of solid target materials under active cooling in an effort to develop a more comprehensive knowledge of design tradeoffs among conventional solid target options. A design window approach will help define the possible operating configurations. The major constraints on survivability are heat removal, surface erosion rates, and fatigue life. Known data and materials behavior for eight selected materials will be incorporated in developing a design methodology for optimizing target life subject to heat load and pumping power constraints, and for optimizing the allowable heat load subject to lifetime constraints.

The eight candidate elements and alloys are: Beryllium, Graphite, Aluminum, Titanium Alloy (Ti-6Al-4V), Vanadium Alloy (V-25Cr-8Ti), Copper Alloy (ZAC-2), Niobium Alloy (D-43), and Molybdenum Alloy (TZM).

In considering heat removal, several thermo-hydraulic concerns must be addressed. The operating limits imposed by critical heat flux, fluid pressure drop, and heat transfer coefficient must be defined. The potential benefits of swirl and mixed flow schemes and the impact of axisymmetric heating will be assessed. A survey of possible coolants indicates that subcooled water offers advantages over other coolants in handling high heat fluxes. Water coolant boasts the broadest range of correlated behavior, and will be used exclusively for this study.

Sputtering rates based on controlled, single incident-species experiments will be extrapolated to the projected environment of the next generation tokamak experiments to indicate the severity of this major constraint on the target design process. The impact on the plasma and on particle handling requirements will also be examined.

Thermo-mechanics of solid targets will be treated in accordance with guidelines of the ASME Pressure Vessel Code for Nuclear Components. Tube and flat plate geometries will be evaluated for cases of a single

material, and for cases of a coating or cladding over a substrate.

The divertor target design procedures developed here should be applicable, with minor modification, to the development of actively cooled limiters and divertor duct walls.

C. Summary of Other Divertor Work to Date

Several detailed solid divertor target designs have been produced to date. These range in intended use from developmental programs with low capacity factors to commercial power reactors with stringent availability requirements. Each is currently subject to some doubt as to survivability at the commercial scale.

The Poloidal Divertor Experiment is now operating at Princeton to assess the feasibility of employing divertors as impurity and exhaust control devices. Using titanium plates as particle collectors, the experiment has successfully performed the divertor functions for very low energy plasma edge particles (20 to 30 eV).

The category of developmental systems includes the proposals of Grumman (SLPX, Ref. 4), Oak Ridge (ETF, Ref. 5), and the U.S. INTOR report (Ref. 6). The Grumman design for the conceptual Superconducting Long Pulse Experiment at Princeton envisions a solid poloidal divertor which incorporates swirl water flow in a ladder-like tube array to cool a total heat load of 40 MW. Pulse durations are

30 seconds. Average heat flux on the tubes is 1.5 kw/cm^2. Gettering of reflected particles and regeneration heating is the projected particle handling method. The heat removal system employs a design previously demonstrated to handle a heat load of 3.2 kw/cm^2 (Ref. 7), but no consideration of surface sputtering or fatigue failure is made. The Oak Ridge design handles a total heat load of 50 MW, an average heat load of 1.1 kw/cm^2, and a pulse length of 100 seconds. It will undergo 5 x 10^4 cycles per year. The INTOR design proposes tungsten protective tile brazed over water cooled copper plates to accomodate an average heat load of 0.5 kw/cm^2. The one centimeter thick tiles are projected to last two years in the sputtering environment, but the effect of sputtered tungsten on plasma energy is a major unanswered question.

In a more generalized category of divertor target design is the proposal of Westinghouse (Ref. 8), a bundle divertor target consisting of sloped tube arrays which handle heat fluxes up to 3.2 kw/cm^2. Special considerations to protect tube bends exposed to cyclic thermal stresses and sputtering have not been provided for.

On the commercial scale, UWMAK III advocates a poloidal divertor with energy absorbing TZM collector plates. Sodium coolant is used to handle an average heat load of 0.589 kw/cm^2. Burn length is 30 minutes. Energetic incident particles impinge on a thin sacrificial

TZM sheet which must be replaced in-situ every 17 hours. Particle collection is then achieved by a series of cryopumps.

Facilities are in existence which handle heat fluxes from 2 to 12 kw/cm^2 for specific non-tokamak configurations, notably those of NASA-Ames (Ref. 9), McDonnell-Douglas (Ref. 10), and RCA (Ref. 11). Fatigue and sputtering constraints are not major concerns for these devices.

Investigations into first wall cooling capabilities have been made, resulting in specific design points for high heat flux situations. Notable is the report of Hoffman, et al. (Ref. 12), which predicts safe heat flux capabilities of 3.3 kw/cm^2 for thin walled, 1 cm inner diameter, 1 meter long tubes heated on one side. Their anticipated pumping power to heat transfer ratio is 3%. No provision is made for sputtering or fatigue.

Input from the Divertor Workshop at MIT, April 1980, and the Plasma Materials Workshop at Sandia-Albuquerque, June 1980, led to selection of a design heat load of 1 kw/cm^2 as reasonable for the divertor target plate, based on existing materials constraints. Off normal conditions resulting in temporary heat loads up to 2 kw/cm^2 were deemed possible. Experimentation is today under way at Sandia-Albuquerque to achieve acceptable operation under a 2 kw/cm^2 heat load.

The recent STARFIRE proposal of Argonne National Laboratory (Ref. 13) is of interest to divertor designers, even though the proposed commercial-scale reactor employs a toroidally mounted limiter to fulfill the divertor functions. Survival of the particle collecting plates is greatly enhanced by extracting a greater fraction of the plasma energy as radiation and by requiring a relatively low particle load on the surface. The anticipated peak heat loads of 0.4 kw/cm^2 make survivability quite possible. Continuous operation also enhances survival chances by greatly reducing fatigue constraints. Beryllium coating material ostensibly overcomes the sputtering erosion problem by redepositing beryllium on the limiter. Each of these features is of great value in prolonging divertor life.

D. Base Case Parameters

As noted earlier, the desired divertor target in this investigation must survive for one year under operating heat loads of 1 kw/cm^2. In order to permit consistent analysis, operating conditions derived from ETF and INTOR studies are established as follows.

- -Pulse duration is 90 seconds.
- -Rejuvenation period is 15 seconds.
- -Three targets are assumed, such that each spends 1/3 of the time "on line" and 2/3 of the time in a "particle regeneration" status.
- -Devices operate with no prolonged shutdowns for a

one year period.

-Each target undergoes 10^5 plasma pulse cycles per year.

-Ion temperature at the target is 1.3 keV.

-Particle current is 1.5×10^{23} /sec.

-Available surface area for a bundle divertor is 9 m^2.

-Particle flux is 1.67×10^{22} /sec-m^2.

To establish the design window procedure, a set of base case parameters for the target is established. The selection of these parameters is guided by analysis of the impacts of ion sputtering, cyclic fatigue, subcooled boiling pressure drop, and critical heat flux. They are selected as representative of the practical ranges of each variable. The 10 cm length is selected as reasonable for near-term single component testing. Variation of each parameter is examined in Chapter VI. The base case parameters are:

Heat Flux	q''	=	1 kw/cm^2
Target Life (Goal)	τ	=	1 year
Coolant Channel Length	L	=	10 cm
Channel Diameter	D	=	1 cm
Coolant Pressure	p	=	500 psia, 3.45 MPa
Coolant Inlet Temperature	T_{in}	=	30 °C, 86 °F
Tube Outer Radius to Inner Radius Ratio	$\frac{t+r}{r}$	=	1.2

II. THERMO-HYDRAULICS

A. Coolant Survey

Successful heat removal for the base case target design requires an actively cooled system. A survey of a variety of basic options for active cooling was made. Liquid metals, helium gas, subcooled water, and mist-steam flows were compared for viability. High pressure drops occur for liquid metals flowing transverse to the diverted magnetic field lines (Refs. 14,15). Helium offers safety and materials compatibility advantages, but was assessed as inferior to subcooled water in the extensive analysis of the STARFIRE study group (Ref. 13). Mist-steam flow can operate at lower coolant pressures than is practical for subcooled water, but materials are not known which could operate at the high resulting wall temperatures. Mist-steam flows would also demand a relatively high pumping power. Subcooled water emerges as the most attractive coolant for the high heat flux divertor target, assuming adequate provision for safeguarding against water-alkali metal reactions is possible.

B. Determination of Applicable CHF Correlations

Under the very high heat loads experienced by the divertor target, channels cooled by subcooled liquid are subject to catastrophic failure resulting from coolant burnout. Accordingly, the first limitation on fluid

operating parameters is the proximity of the coolant to a critical heat flux condition. A review of literature concerning critical heat flux for water in flow boiling indicates that many attempts have been made to correlate CHF data under diverse conditions. Unfortunately, extrapolation of any correlation beyond its data range is quite tentative, as the predictions of different correlations may vary widely. Pertinent correlations and their data ranges appear in Table II-1. British Engineering Units will be used throughout this chapter, since most correlations are formulated using them.

To evaluate the validity of CHF correlations for a 1 kw/cm^2 heat flux, the constraints on mass flux, G, and inlet temperature, T_{in}, were defined for base case conditions, and plotted in Figure II-1. Reasonable CHF predictions should fall in a range between the onset of nucleate boiling and the flow regime transition from slug to annular flow. T_{in} could vary from freezing to saturation temperature.

The conditions at which the onset of nucleate boiling occurs just at the end of the channel may be determined from the equation:

$$(1) \quad G = \frac{4\, q''\, L\, (\frac{r+t}{r})}{\pi\, D\, c_p} \left[\frac{1}{(T_{sat}-T_{in}) - q''/h + \Delta T_{ONB}} \right],$$

where;

$$(2) \quad h = \frac{k}{D}\, .023\, (\frac{G\, D}{\mu_l})^{.8}\, (\frac{c_p\, \mu_l}{k})^{.4}\, (\frac{\mu_w}{\mu_b})^{.14}, \text{ (Ref.16)},$$

and,

$$\Delta T_{ONB} = \left[\frac{q''}{15.60\ p^{1.156}}\right]^{.435}\ p^{.0234} \qquad (3)$$

is the Rohsenow- Bergles correlation for incipient nucleation in British Engineering Units (Ref. 17).

Mass flux must be large enough to avoid transition from slug to annular flow in the channel, which occurs at approximately an equilibrium quality of 0.1 at the base case pressure. From the energy balance, a lower bound on G is found by requiring that the equilibrium quality at the channel exit be less than 10%:

$$G \geq \frac{4\ q''\ L\ (\frac{r+t}{r})}{\pi\ D\left[c_p(T_{sat}-T_{in})+.1\ h_{fg}\right]} \qquad (4)$$

The condition of exit saturation is determined similarly and is also plotted on Figure II-1.

The predictions of various correlations were plotted for the base case as in Figure II-2. Neither of the established physical mechanism boundaries on mass flux appear to come close to predicting CHF. A better theoretical approach would be determination of the point of net vapor generation, following the procedure of Zuber and Saha(Ref. 54). This procedure stipulates the conditions under which bubbles first detach from the channel walls. As the mechanism for CHF at very high heat fluxes is proposed to be insulation of the surface by a bubble boundary layer (Ref. 18) this net vapor generation point is thought to be a good prediction of the CHF point. A plot of the

Saha-Zuber equation appears on Figure II-2, showing good agreement with the Bernath and Gunther correlations at intermediate subcoolings. The agreement is not as close when tube length is varied, but the Saha-Zuber procedure provides a CHF prediction based on a plausible theoretical mechanism. It should be evaluated over a range of variables and checked for agreement with available CHF data.

A comparison of the plots in Figure II-2 with corresponding data ranges of Table II-1 indicates that the Bernath correlation is in general most appropriate for the base case conditions. It purports to be valid over such a wide range, however, that its accuracy is only to within 30% (Ref. 18). Further, its range does not include particularly high subcooling, where its plotted behavior becomes erratic. Since high subcooling appears to permit the most efficient operation, a correlation suited to that condition is desirable. The correlation of Rousar (Ref. 19) accounts for high subcooling at elevated pressures for tube lengths up to 15 cm. It is based on uniform circumferential heat fluxes from 1.6 to 10.3 kw/cm^2, and suggests that for very high heat

fluxes, local conditions govern CHF, independent of pressure, length, and diameter. Work by Lowdermilk, et al. (Ref.20) with thin tubes up to 114 cm in length offers data in the 1 kw/cm^2 range, and indicates a length and diameter effect. It does not, however, include the effect of varied subcooling. In order to permit variation of length, diameter, and subcooling in parametric analyses to follow, a combination of the Rousar and Lowdermilk correlations is proposed for the 1 kw/cm^2 heat flux range. The Rousar treatment of CHF as a local condition proportional to subcooling is applied to the Lowdermilk correlation, giving:

$$q''_c = \frac{1400}{D^{.05} L^{.15}} \left[\frac{G \, \Delta T_{sub}}{90} \right]^{.5} . \quad (5)$$

For a uniform axial heat flux the critical condition would occur at the tube exit, where:

$$\Delta T_{sub} = T_{sat} - T_{in} - \left[\frac{4 \, q'' \, L \left(\frac{t+r}{r} \right)}{\pi D \, c_p \, G} \right] . \quad (6)$$

Substituting into the above expression and rearranging gives:

$$G_{crit} = \frac{90 \left[\frac{D^{.05} L^{.15} \, q''}{1400} \right]^2 + \left[\frac{4 \, q'' \, L \left(\frac{t+r}{r} \right)}{\pi D \, c_p} \right]}{(T_{sat} - T_{in})} . \quad (7)$$

This expression closely corresponds with the Rousar correlation for the base case, as shown in Figure II-3.

The effects of varying pressure, length, and heat flux on the behavior of the Bernath, Rousar, and modified Lowdermilk correlations are plotted in Figures II-3,

II-4, and II-5. The modified Lowdermilk correlation is seen to give more conservative estimates of CHF than either Rousar or Bernath at longer channel lengths. This conservatism will be incorporated into the design window to compensate for the lack of specific data over the ranges of interest. Figure II-5 indicates that the modified Lowdermilk expression is not conservative for higher heat fluxes. Design window development at heat fluxes in the range of Rousar's data ($q" > 1.6$ kw/cm^2) should use Rousar's correlation, but with the caution that extending the channel length may make the correlation unconservative.

In order to account for experimental error and component tolerances, the common design practice in fission reactors has been to establish a minimum critical heat flux ratio below which the coolant should not go during normal operation. Until recently, this design CHFR has been 1.3, meaning that the predicted CHF must always be at least 1.3 times larger than the actual local heat flux. Extensive experience with fission reactors has recently led to the lowering of this CHFR in fission reactor design. Due to the uncertainties inherent in the fusion program, the safety factor of 1.3 will be retained for this analysis. The effect of lowering the safety factor is examined in Chapter VI.

C. Pressure Drop Limitations

One means of achieving higher heat loads is simply increasing the coolant mass flow rate. This option is constrained, however, by the unavoidable pressure loss experienced during passage along the coolant channel. Extremely high heat loads have been handled successfully, where the heated length was on the order of 1-2 cm, by pumping coolant at very high velocity and with large pressure losses (refs. 21, 22). This method is employed at NASA-Ames Research Laboratory, where a 540 psi pressure drop is experienced over a 10 cm cooling length to accomodate heat loads as high as 12 kw/cm^2 (Ref. 9). For the divertor, somewhat longer heated lengths may be desirable, accomodating lower heat fluxes, requiring more reasonable pressure losses, and lower pumping power requirements.

For the case of single phase flow the pressure drop to be expected in the channel may be approximated using the Darcy-Weisbach friction factor formula, taking the friction factor to be an empirical approximation to the Moody chart for smooth pipes at high Reynolds numbers. Complications arise due to the variation of viscosity with the non-uniform temperature distribution in the flow cross section. For uniform circumferential heating, a viscosity ratio factor, $(\mu_w/\mu_b)^v$, is commonly included in the friction factor. Suggested values for the exponent v range in the literature from .14 (Ref. 16) to .35 (Ref. 28). For single-

sided heating, the film temperature drop would vary around the channel circumference. Kays (Ref. 56) provides a procedure for determining the local heat transfer coefficient inside a tube under single-sided heating. By analogy, an expression for local friction factor may be obtained, and the average tube friction factor determined. For simplicity, a viscosity ratio factor of $(\mu_w/\mu_b)^{.25}$ is employed here, where μ_w is evaluated at a wall temperature averaged around the tube. Properties for water are taken from Ref. 23. The single phase pressure drop equations are then:

$$p = \frac{f\ L\ G^2}{2\ D\ \rho\ g_c}, \quad \text{where;} \tag{8}$$

$$f = \frac{.184\,(\mu_b)^{.2}}{(G\ D)^{.2}} \left(\frac{\mu_w}{\mu_b}\right)^{.25}, \quad 3\times10^4 \leq Re \leq 10^7, \tag{9}$$

L = channel length
D = channel diameter
G = coolant mass flux
ρ = coolant density
μ_b = bulk coolant viscosity
μ_w = coolant viscosity at average wall temperature
g_c = units conversion

At high heat loads and moderate mass flux, subcooled boiling along the heated channel walls is very possible. Several investigators provide some indication of the pressure losses to be expected, among them; Owens and Schrock (Ref. 24), Tarasova (Ref. 25), Mendler (Ref. 26), Martinelli and Nelson (Ref. 27), and Dormer and Bergles (Ref. 28). Wide variance in pressure drops and test

conditions exists, however, suggesting more design specific experimentation before taking full advantage of the subcooled boiling condition.

The study of first wall cooling by M.A. Hoffman, et al. (Ref. 12), concluded that the Mendler-Martinelli-Nelson model was most appropriate for their design case, resulting in a tripling of the effective friction factor over the nonboiling factor near the end of their tube. The Owens-Schrock model predicted a thirteen-fold increase in friction factor for the same subcooled boiling conditions. The experimental work of Dormer and Bergles (Figure II-6) records the behavior of total pressure drop for various tube L/D ratios as the subcooled boiling regime is entered. For L/D values of 50 and 100, total tube pressure drops in subcooled boiling more than six times greater than the corresponding adiabatic flow pressure drop were recorded. For shorter tubes (L/D = 25), pressure drops had reached only about 3 times their adiabatic value when onset of critical heat flux occurred. For tubes with L/D = 10, the higher wall shear common to the entrance region may be expected to increase the total pressure drop by up to 50% (Ref. 16), so that total pressure drops up to 4 to 5 times larger than the non-boiling Δp may be expected when fully developed subcooled boiling occurs.

Evaluation of the subcooled boiling pressure drop in

the 10 cm long base case tube, using the Mendler approach (Ref. 26), indicates that only at very low local subcooling does the subcooled boiling pressure drop exceed the predicted isothermal pressure drop. As is evident in Figure II-6, the favorable viscosity effect overcomes the boiling effect shortly after onset of boiling. Only when the heat flux on the tube becomes a significant fraction of that which would cause the exit to be saturated (under the same flow conditions) does the subcooled boiling effect greatly raise the pressure drop. For longer tubes, both the Dormer data and the Mendler formula predict a more rapid increase in pressure drop upon onset of boiling, necessitating more careful analysis.

From Figure II-4 it is apparent that at sufficiently high subcoolings, adequate cooling can be provided without boiling for a 1 kw/cm^2 heat flux, in tubes up to 1 meter long, with a mass flux on the order of 10^7 $lbm/hr\text{-}ft^2$. The non-boiling pressure drop over a 1 meter long tube at this mass flux is less than 3 psi, so that even a six-fold increase in Δp due to subcooled boiling should not be a major problem. Only at lower inlet pressures, higher heat loads, and longer lengths would the subcooled boiling pressure drop become critical.

The ratio of pumping power required for coolant circulation to thermal power extracted by the coolant is

a frequently used measure of cooling system efficiency.

$$W_p = \frac{\text{Pumping Power}}{\text{Thermal Power}} = \frac{\dot{m}\,\Delta p/\rho}{\dot{m}\,c_p\,\Delta T_{1-2}}$$

$$= \frac{\Delta p}{\rho\,c_p\,\Delta T_{1-2}} \qquad (10)$$

Based on overall power conversion efficiency in a fusion reactor blanket, Fraas (Ref. 29) suggested a design limit for this ratio of 2%. Since the divertor would handle only a small fraction of the total plasma power, it could be run at a much higher ratio, without very seriously impacting overall plant efficiency. However, since the occurrence of subcooled boiling may increase the pressure drop up to six times, the 2% limit will be used for the design window, with Δp calculated for non-boiling flow.

$$W_p = \frac{\Delta p_{nonb}}{\rho\,c_p \Delta T_{1-2}} \leq .02 \quad . \qquad (11)$$

Figure II-7 indicates the curve for pumping power ratio = 2% in the nonboiling and boiling regions. The small area included below the extension of the nonboiling W_p = 2% into the subcooled boiling region represents a "flagged" region in the design window. Operating points here require special analysis for subcooled boiling pressure drop, using the Mendler approach.

D. Heat Transfer Coefficient

The susceptibility of target materials to reach temperatures at which material integrity diminishes de-

mands that good heat transfer from channel wall to fluid be achieved. Subcooled boiling and other mechanical methods enhance fluid mixing, thereby increasing the heat transfer coefficient. For the design window a single phase heat transfer coefficient by McAdams (Ref. 19) will be used to develop the fluid-wall interface temperature profile.

$$Nu = .023\ (Re)^{.8}(Pr)^{.4}\ (\mu_b/\mu_w)^{.14} \qquad (12)$$

The occurrence of subcooled boiling would make this equation conservative. Further, the steep temperature gradient at the wall in the entrance region would enhance heat transfer there, further increasing the conservatism for short tubes. For base case conditions and mass flux on the order of 10^7 lbm/hr-ft^2, this equation predicts a film temperature rise of ~270 °F. Even with low inlet temperature and subcooled boiling, therefore, the inner wall temperature will be over 300 °F, posing a high temperature materials challenge.

E. Swirl and Mixed Flow Schemes

Extensive work has been documented on the advantages realized in coolant channel performance when internal devices are employed to induce swirl flow. The effect is to strip away nucleating bubbles and force denser (colder) coolant to the outside wall where heat transfer is occurring. Correlations for critical heat flux, pressure drop, and heat transfer coefficients in such cases are presented

by Gambill, et al. (Ref. 7). Approximately 1.5 to 1.8 times higher CHF can be realized over straight flow at the expense of 1.4 to 1.8 times higher pressure drop. The heat transfer coefficient is improved over straight flow by up to 85% for constant flow rate (Ref. 30). In terms of available design window space, the benefits of higher CHF are roughly offset by the penalty of higher pumping power. Swirl flow appears attractive in easing material temperature restrictions through increased film heat transfer coefficient. Unless operation near a material temperature limit is required, the use of swirl flow does not appear necessary for the base case conditions. From a particle handling viewpoint, swirl flow offers a means of controlling diffusion rates through channel wall temperature control.

F. Effect of Asymmetric Heating

Collier (Ref. 31) summarizes data regarding the effects of asymmetric circumferential heating. For highly subcooled boiling, he recommends treating the occurrence of burnout as a localized condition. This implies that burnout occurs where the incident flux is normal to the channel wall, at the same heat flux as would cause burnout for the uniform heating case. This is clearly conservative, as no allowance is made for fluid convection, conduction around the tube circumference, or conduction in the fluid.

As a conservative limit, the uniformly heated CHF value will be considered the design constraint.

The case of swirl flow virtually negates the effect of asymmetry, since the entire fluid column is rotated past the hot spot. Kim, et al. (Ref. 32) predict that CHF values twice as high as for uniform heating may be achieved utilizing a swirl flow for cooling a one-side-only heating situation.

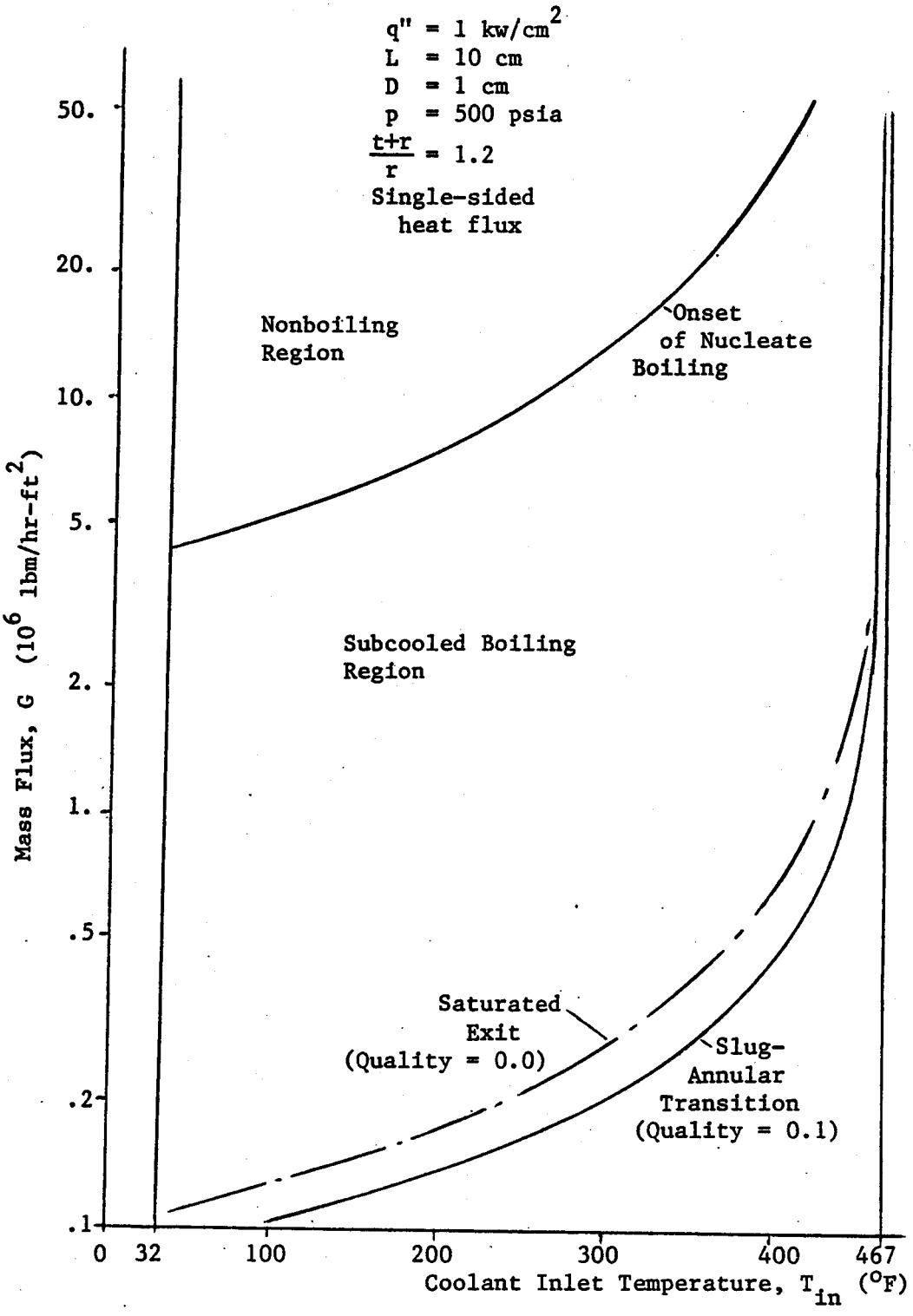

Figure II-1: Generalized Hydraulic Option Space Showing Constraints on T_{in} and Mass Flux. Critical Heat Flux and Pumping Power Constraint Not Yet Fixed.

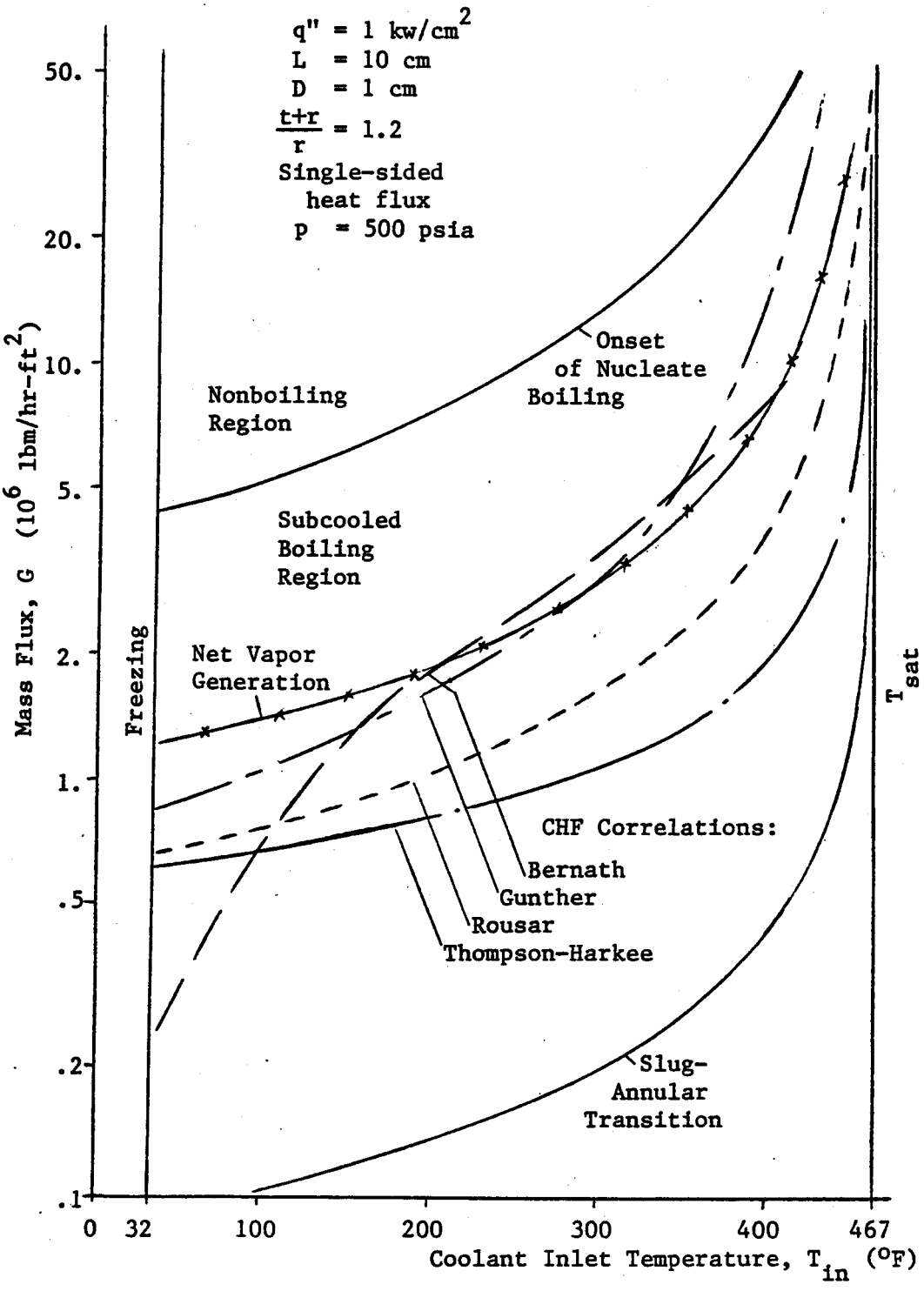

Figure II-2: Comparison of CHF Correlations for Base Case Conditions

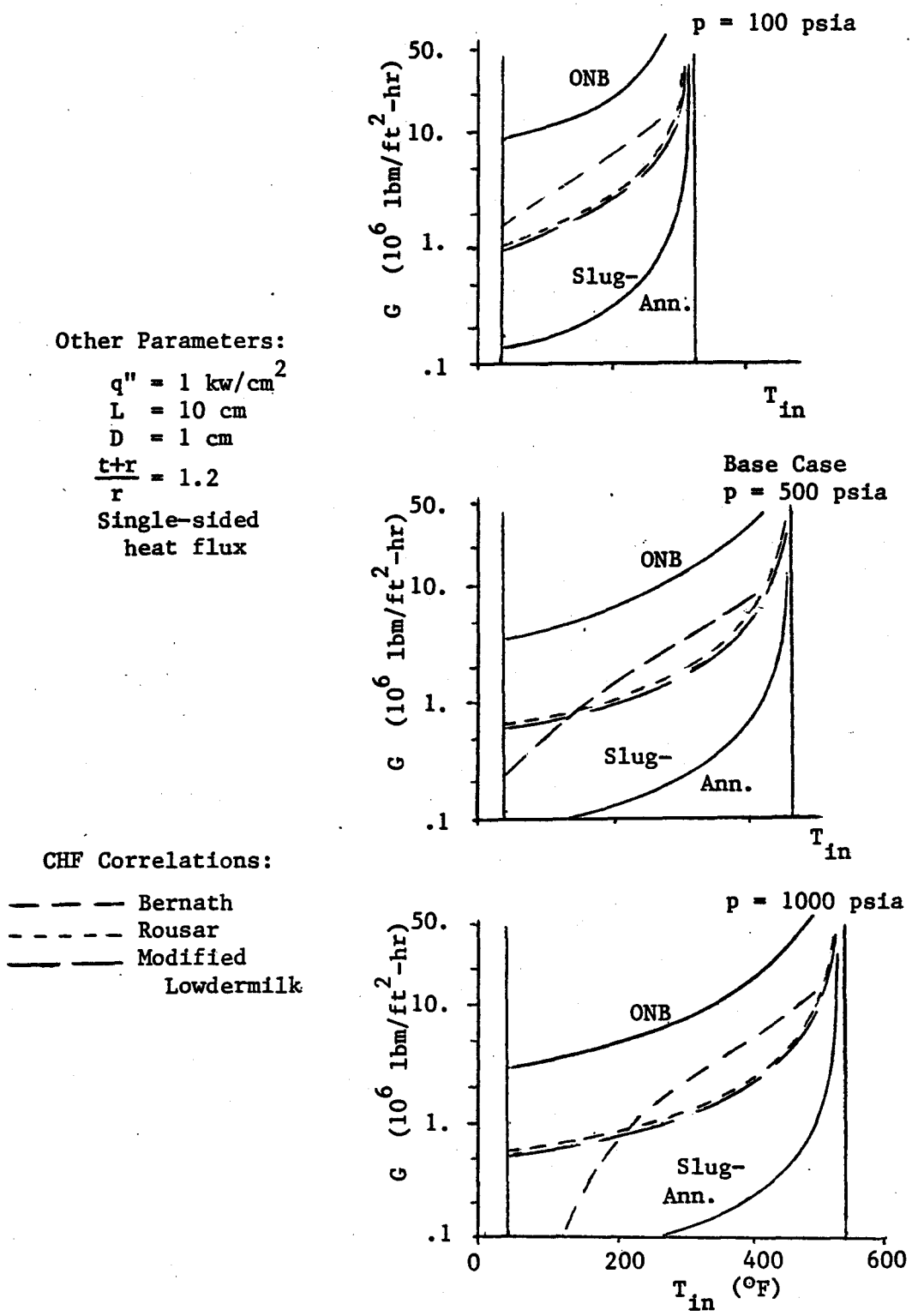

Other Parameters:

$q'' = 1$ kw/cm^2
$L = 10$ cm
$D = 1$ cm
$\frac{t+r}{r} = 1.2$
Single-sided heat flux

CHF Correlations:

— — — Bernath
- - - - - Rousar
—— —— Modified Lowdermilk

Figure II-3: Effect of Varying Pressure on Behavior of Pertinent CHF Correlations. Other Conditions Remain as in Base Case.

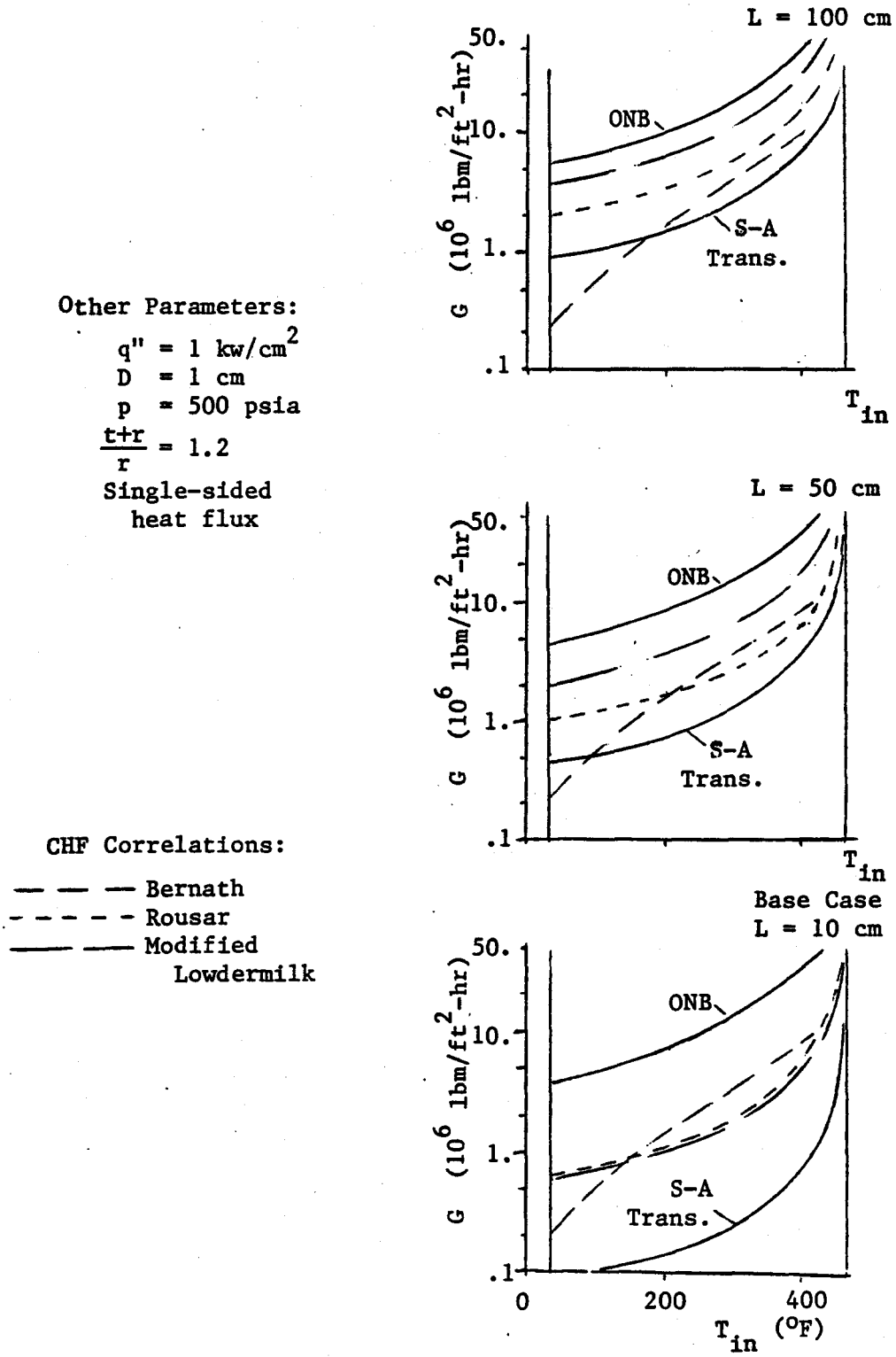

Figure II-4: Effect of Varying Length on Behavior of Pertinent CHF Correlations. Other Conditions Remain as in Base Case.

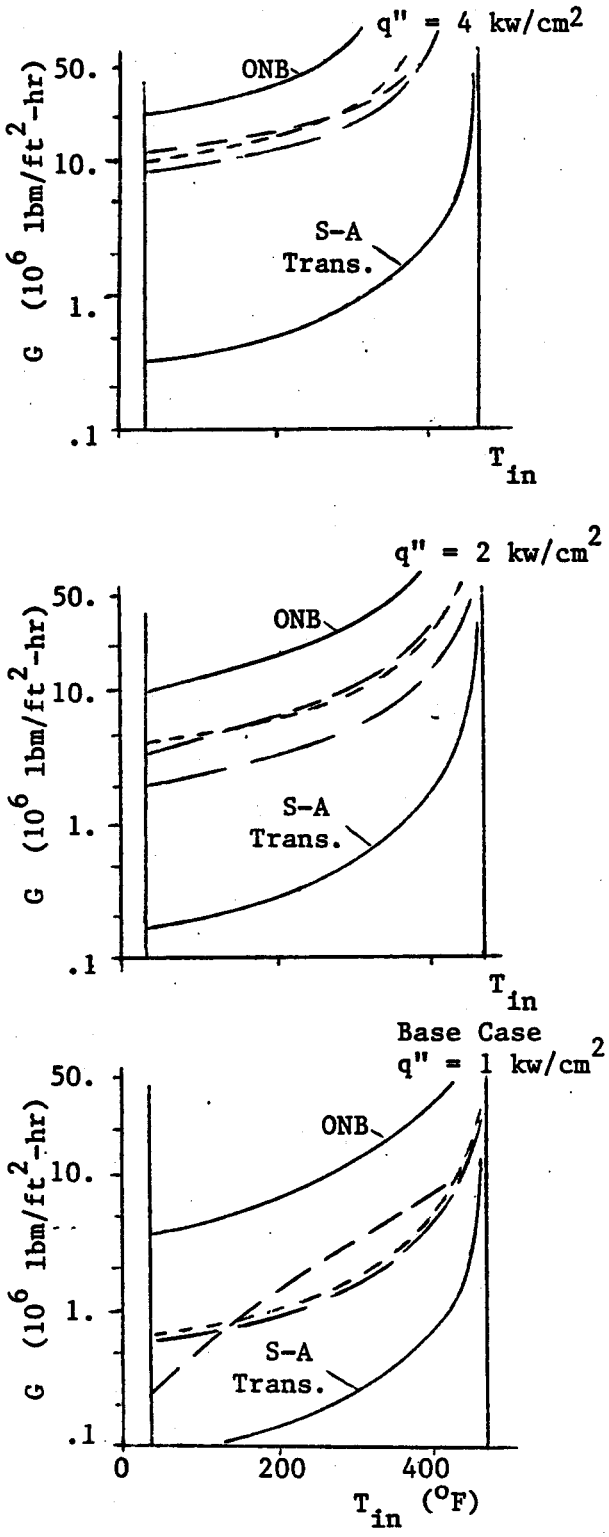

Other Parameters:

L = 10 cm
D = 1 cm
p = 500 psia
$\frac{t+r}{r}$ = 1.2
Single-sided heat flux

CHF Correlations:

— — — Bernath
- - - - - - Rousar
—— —— Modified Lowdermilk

Figure II-5: Effect of Varying Heat Flux on Behavior of Pertinent CHF Correlations. Other Conditions Remain as in Base Case.

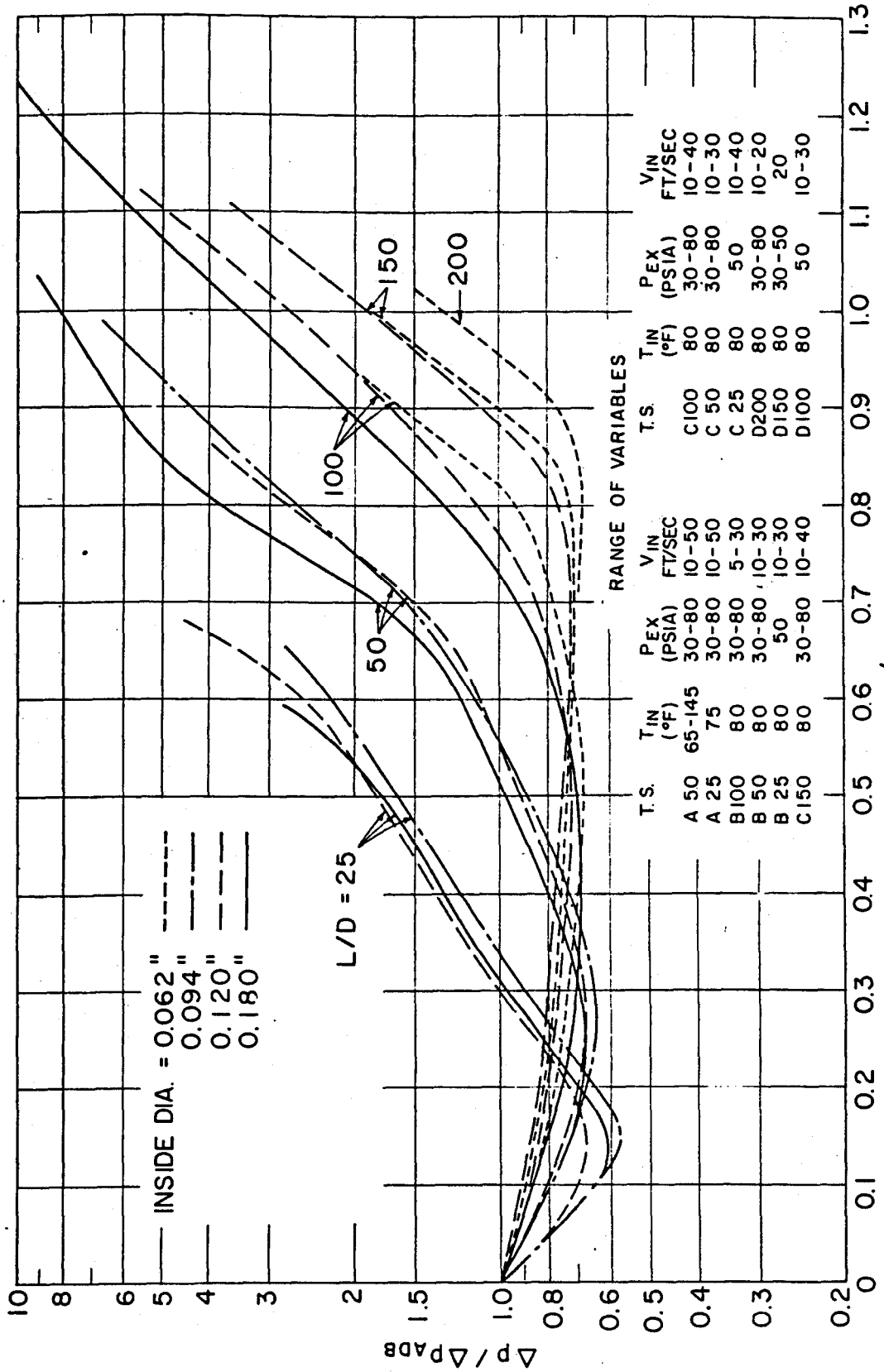

Figure II-6: Experimental Results Showing Effect of Subcooled Boiling on Dimensionless 4p (28).

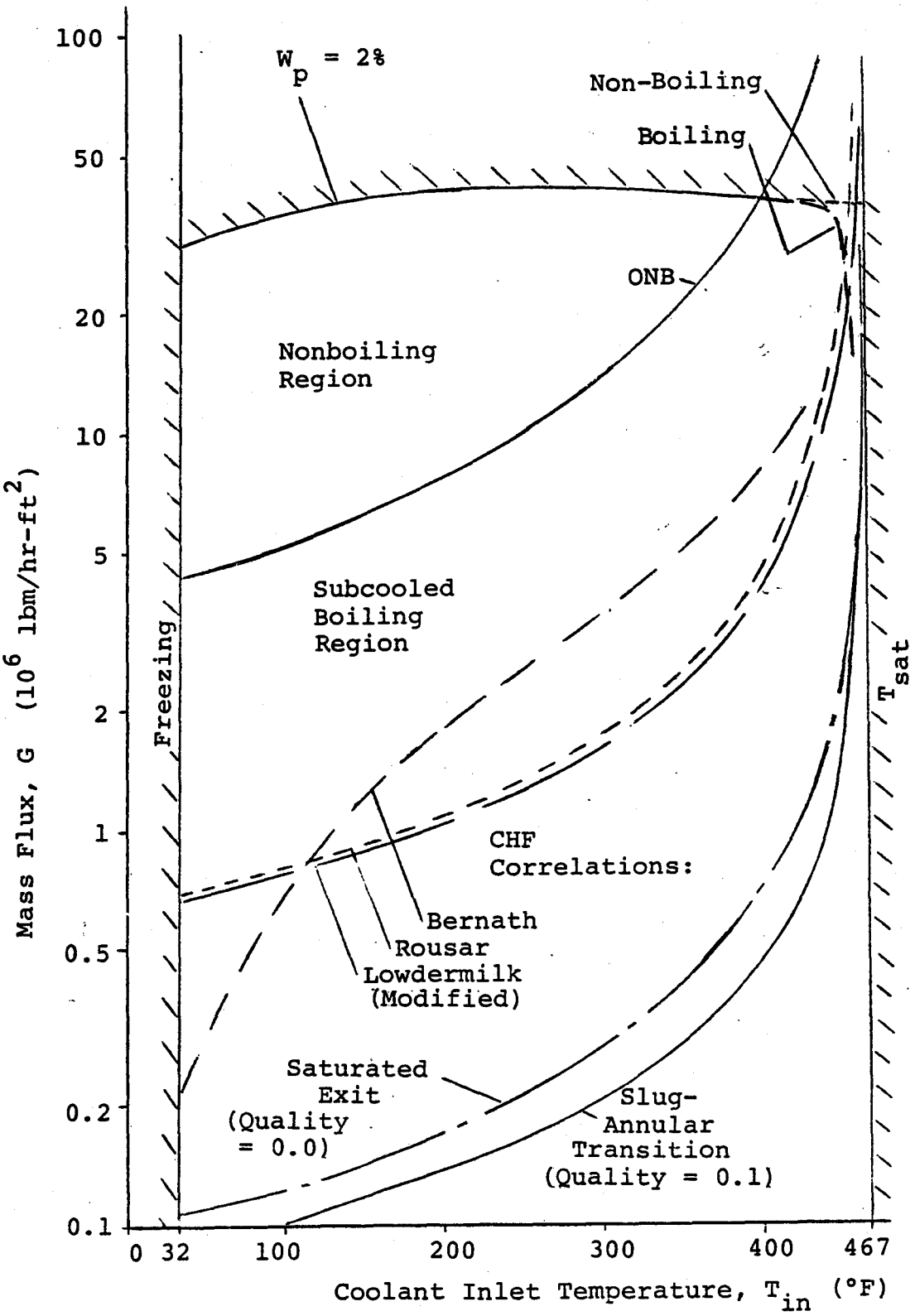

Figure II-7: Hydraulic Option Space and CHF Correlations for Base Case Conditions

Correlations (English Units)	Length Range (cm)	Diameter Range (cm)	Subcooling Range (^{o}C)	Pressure Range (psia)	Velocity Range (m/sec)	CHF Range, (kw/cm^2)
Gunther: $q''_c = 7000(T_{sat} - T_b)V^{0.5}$	9	1.5	12-157	15-164	1.5-12.2	0.1-3.5
Bernath: $q''_c = h_c(T_w - T_b)$, where; $h_c = 5445 + 48V/D_h^{0.6}$, $T_w = 1.8\left[57(\ln \rho) - 54\left(\frac{\rho}{\rho+15}\right) - \frac{V}{4}\right] + 32$ (ρ in psia)	?	.36-1.67	21-218	23-3000	0.1-16.5	0.1-3.6
Lowdwermilk: $q''_c = 1400\ G^{.5}/D^{.05}L^{.15}$	5-114	.13-.48	5-88	15-100	0.1-20.6	0.3-2.17
Thompson-Harkee: $q''_c = 9308\ V^{.9}\ (\Delta T_{sub})^{.6}$	2-15	.4-1.2	70-260	600-1500	15-45	1.6-11.2
Rousar: $q''_c = \left[2.64 + 0.00045\ V\ \Delta T_{sub}\right] 10^6$	2-15	.4-1.2	70-260	600-1500	15-45	1.6-10.3
Gambill: $q''_c = \frac{398\ G^{.645}\left[1+\left(\frac{\pi}{2y}\right)^2\right]^{\frac{1}{2}} D_i^{.24}}{L^{.44}}$	3.8-30.5	.33-.63	.2-144	15-545	4-48	.9-11.8

Table II-1: Comparison of Critical Heat Flux Correlations and Data Ranges

III. SURFACE INTERACTIONS

A. Sputtering and Plasma Contamination

The problem of impurity sputtering, which the divertor is intended to reduce at the tokamak first wall, is particularly acute at the divertor target itself. The ability of energetic ions to erode the solid target surface upon impact is a major limit on the target design. The rate at which the material will erode may be expressed to first order by the formula:

$$\frac{\Delta t}{\Delta \tau} = \sum_i S_i J_i C \left(\frac{M}{\rho N_A}\right) , \qquad (13)$$

where; Δt = change in thickness
$\Delta \tau$ = change in time
S_i = sputtering coefficient (atoms/ion)
J_i = ion flux at divertor surface
C = capacity factor of target (% of year exposed to target)
M = target material atomic weight
ρ = target material density
N_A = Avogadro's Number

This relation may be used in comparing candidate materials for use as target materials. The distribution of particle fluxes and energies across the target surface must be considered to account for accelerated erosion in regions of peak flux. Lacking such information, this work will apply the average particle fluxes to impose a comparative constraint on material thickness and lifetime. Sputtering coefficients are taken from Refs. 33 and 34.

The energy, mass, and angle of incidence of impinging ions have significant effect on the local sputtering coefficient. Figure III-1 shows the typical dependance of light ion sputtering coefficient on incident energy and mass. The peak of each curve occurs in the range 1-2 keV.

The sputtering coefficient varies with incident angle according to:

$$S_i(\theta) = \frac{S_i}{\cos \theta} \text{ , (Ref. 52)}$$

where $\theta=0$ constitutes normal incidence.

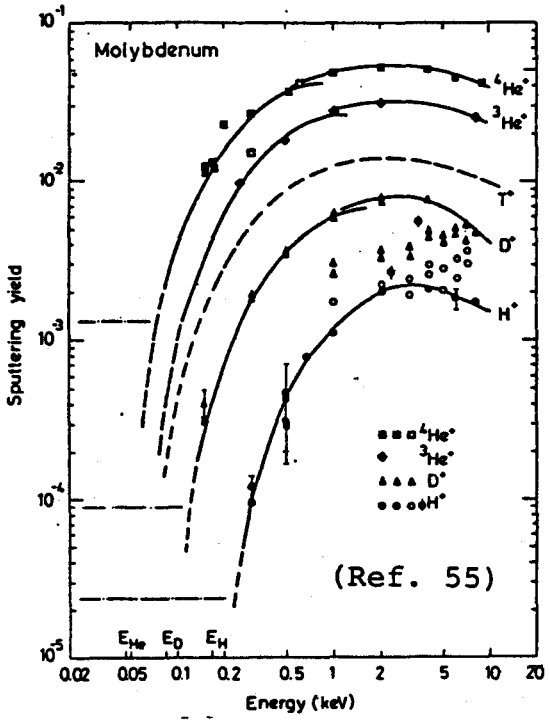

Figure III-1: Typical Sputtering Coefficient Data

Since a negative sheath potential will exist at the surface of an operating divertor, ions will be accelerated abruptly toward the target. This acceleration should raise the ion energy from the plasma edge temperature of .3 to .5 keV up to about 1.3 keV (Ref. 53). Further, it should make the angle of incidence nearly vertical. Normal incidence at 1.3 keV is assumed for this study. The effect of improving the sputtering climate is examined in Chapter VI. It should be noted that helium and heavier impurities have not been included as sputtering agents for this analysis.

Table III-1 summarizes the key sputtering variables and their product for the eight candidate materials.

As shown in Figures III-2 and III-3, the sputtering lifetime of a given target material increases linearly with its thickness. This suggests a minimum thickness permissible for a specified target life.

Considerable investigation is warranted to determine to what degree any redeposition of surface material may be expected on the exposed target surface. It would seem implausible for such assistance to occur in regions of peak flux, though its demonstration would certainly be welcome. None is assumed here. The effect of self sputtering must also be addressed; a destructive cascade being possible for the heavier materials.

Mere comparison of sputtering rate is not sufficient measure of a candidate's usefulness as a target material. The destiny and effect on the fusion plasma of the sputtered impurity must also be considered. A limit on the impurity concentration in the plasma, above which ignition is impossible, is provided by the expression (Ref. 35):

$$I_{max} = 50 \times 10^{-.1\,Z} , \qquad (14)$$

where; I_{max} = maximum allowable impurity (%)

Z = target Z number

Assuming a plasma volume characteristic of next generation reactors (400 m^3) allows determination of a maximum allowable impurity concentration. Further, assuming a divertor duct geometry and pumping system capable of trapping 99% of the target generated impurities estab-

lishes an estimate of the duration of target operation permissible before impurities from the target penetrate the plasma core in sufficient quantity to extinguish the burn. These results are tabulated in Table III-2 for nine materials. Such results are tentative, since the divertor pumping efficiency and the tendency for impurities at the plasma edge to migrate into the plasma core are at present uncertain. The comparison of Table III-2 is valuable, however, for comparing material alternatives.

A relative figure of merit may be devised by simply dividing the sputtering rate by the allowable burn time. The ranking in Table III-3 results, indicating the undesirability of copper and tungsten, and the advantages of beryllium and graphite as plasma interface materials.

B. Internal Erosion

The thickness of the target material may also be diminished by erosion and corrosion on the coolant side. Corrosion is a relatively slow process for most materials under study, and should have little effect relative to the external sputtering rate. Common corrosion rates are at least three orders of magnitude smaller than calculated sputtering erosion rates (Ref. 36). Mechanical erosion by the rapidly flowing coolant may, however, be a concern. Experience with high mass flow boilers and studies of rain damage to high performance aircraft have indicated that liquid water travelling at speeds in excess of 50 meters

per second will cause mechanical damage to metal surfaces. Coolant velocities of less than 30 meters per second should be adequate for a 1 kw/cm^2 heat flux, so direct erosion should not occur. The incidence of surface boiling may generate regions of bubble collapse with erosion rates comparable to those experienced in cavitation erosion. Such erosion has a velocity below which erosion is undetectable. Above this threshold, the erosion rate increases approximately as the velocity to the sixth power (Ref. 37). Such erosion would place a distinct limit on the flow velocity and hence the allowable heat load.

The main damage mechanism in cavitation erosion occurs when voids in the fluid suddenly collapse, generating both intense shock waves and liquid microjets capable of pitting or work hardening nearby surfaces until fatigue failure and material loss occur. Voids generated by boiling on a hot surface cannot collapse at the surface in the same way as cavitation bubbles, since vapor is always being generated by the addition of heat. In subcooled boiling, the bubble collapse should generally occur away from the heated walls and at a slower rate than in cavitation. Thus any internal erosion should be downstream from the heated surface, and of lesser intensity than that due to cavitation. Particular attention will therefore be necessary where the flow direction changes downstream of the heated section to insure that failure by internal

erosion does not occur.

Experiments with cavitation erosion on aluminum surfaces indicated that no appreciable damage was sustained at water velocities less than 12 m/sec (Ref. 37). Since adequate cooling can be provided at high subcooling with velocities less than 10 m/sec (Fig II-7), internal erosion should not be a problem for a 1 kw/cm^2 heat flux case. Should higher velocities be employed to offer protection against plasma disruptions, the possibility of cavitation damage must be specifically examined. TZM is expected to have particularly good resistance to cavitation damage in water, since its oxide is one of very few known to resist wear better than its base metal (Ref. 38).

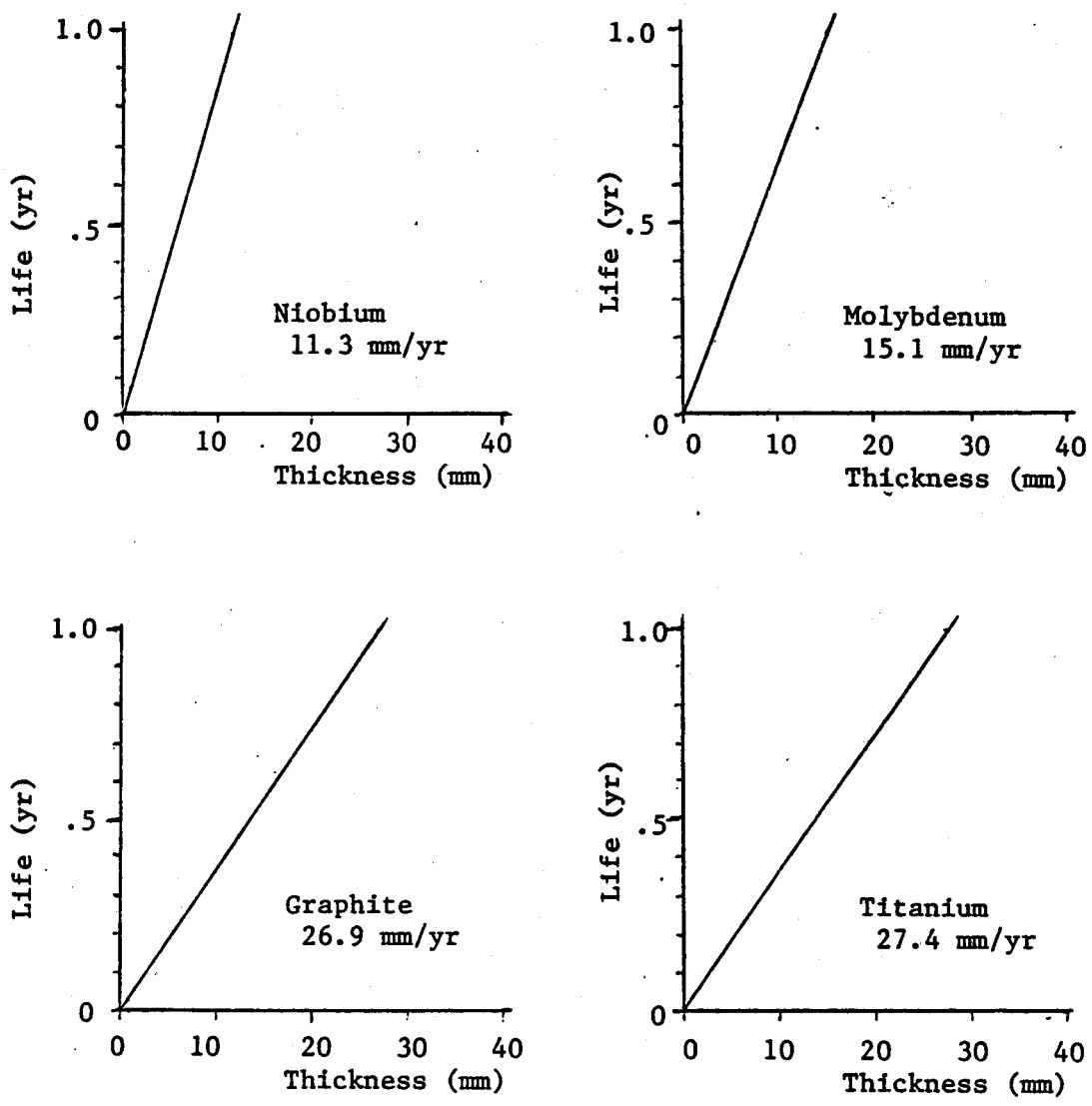

Divertor Power, P = 90 MW = 2.9 N $k_B T_i$; T_i = 1.3 keV.
Particle Current, N = 1.5 x 10^{23} particles/sec.
For 1 kw/cm^2 heat load, 9 m^2 target ;
Particle flux = 1.67 x 10^{22} particles/m^2-sec.
Normal Incident Angle.

Figure III-2: Sputtering Erosion Rates for Base Case Conditions and Capacity Factor, C = .28.

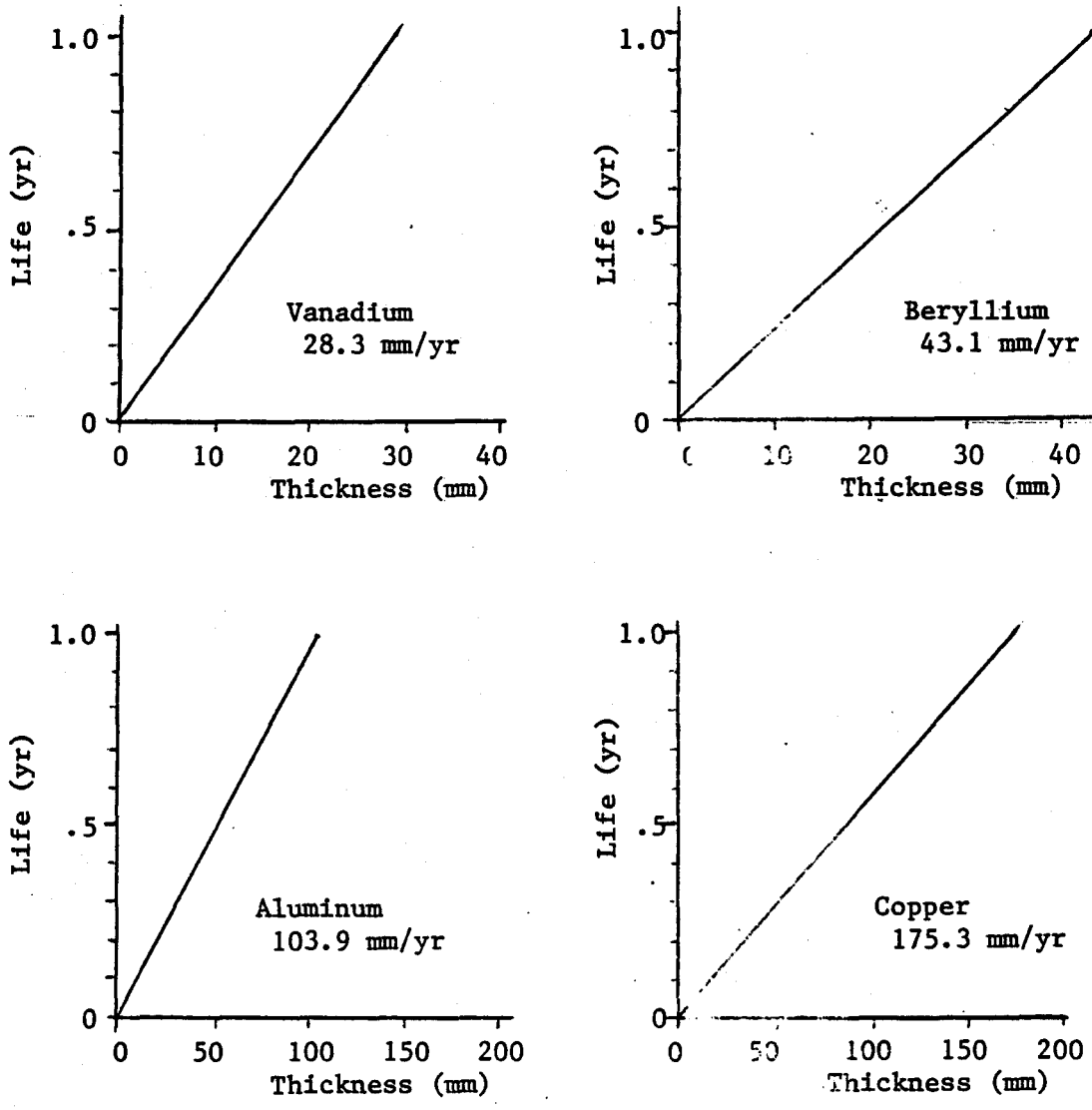

Divertor Power, P = 90 MW = 2.9 N [illegible] T_i = 1.3 keV.
Particle Current, N = 1.5 x 10^{23} [illegible]/sec.
For 1 kw/cm^2 heat load, 9 m^2 targ[illegible]
Particle flux = 1.67 x 10^{22} parti[illegible]-sec.
Normal Incident Angle

Figure III-3: Sputtering Erosion Rates [illegible] Case Conditions and Capacity Factor, C = [illegible]

Element	Z	S_i (atom/ion) for incident D^+ @ 1.3 keV	M ($\frac{gm}{gm\text{-}mole}$)	ρ ($\frac{gm}{cc}$)	$S_i \frac{M}{\rho}$
Be	4	.036	9.012	1.848	.176
C_{gr}	6	.019	12.011	2.10	.109
Al	13	.043	26.982	2.70	.429
Ti	22	.011	47.90	4.54	.116
V	23	.014	50.94	6.11	.117
Cu	29	.101	63.546	8.96	.716
Nb	41	.0046	92.91	8.57	.050
Mo	42	.0066	95.94	10.22	.062

Table III-1: Key Sputtering Characteristics for Eight Candidate Elements

a. Max impurity concentration for ignition:

$$I_{max} = 50 \times 10^{-.1\,Z} \quad \text{(Ref. 35)}$$

b. ETF plasma: 6.4×10^{22} particles.

c. Sputtering rate = $J_i S_i$.

d. Assume 1% of sputtered material gets into plasma. (99% is pumped or condensed.)

e. Plasma burn time limit due to impurity contamination

$$= \frac{\text{max impurity allowed}}{\text{sputtering rate @ 1 kw/cm}^2}$$

f. Results

W - .0082 sec	Nb - 3.8 sec	Al - 234 sec
Mo - 1.94 sec	V - 71.5 sec	Be - 2178 sec
Cu - 2.46 sec	Ti -117. sec	C_{gr} - 2610 sec

Table III-2: Effects on Plasma Burn Times of Sputtered Impurities from Candidate Target Materials.

$$\text{Figure of Merit} = \frac{\text{sputter rate}}{\text{burn time}} \left(\frac{\text{mm}}{\text{yr-sec}}\right)$$

W - 963.4	Nb - 10.6	Ti - .838
Mo - 254.5	Al - 1.58	Be - .071
Cu - 27.8	V - 1.41	C_{gr} - .037

Table III-3: Comparative Figure of Merit for Candidate Materials Due to Sputtering and Plasma Contamination (Small Numbers Preferred).

IV. THERMO-MECHANICS

A. Pressure Stress

The containment of internal coolant pressure imposes a stress constraint which demands that channel wall thickness always exceed a certain minimum. For cases in which the wall may be considered the membrane of a thin walled cylinder, the stress intensity is easily determined as the hoop stress minus the radial stress:

$$S = (p\ r / t) - (-p). \qquad (15)$$

The greatest allowable stress intensity within a material is established by the ASME Code as S_{mt}, and must be less than 1/3 of the ultimate strength and less than 2/3 of the yield strength. The minimum wall thickness allowed is then:

$$t_{min} = \frac{p\ r}{S_{mt} - p}. \qquad (16)$$

For thick walled pressure vessels, the stress at any point, n, in the cylindrical cross section is given by: (Ref. 39)

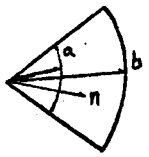

$$\sigma_t = \frac{a^2\ p}{b^2 - a^2} \left(1 + \frac{b^2}{n^2} \right) \text{ and } \sigma_r = \frac{a^2\ p}{b^2 - a^2} \left(1 - \frac{b^2}{n^2} \right). \qquad (17)$$

For internal pressurization, the tangential stress is tensile, the radial stress compressive, and the axial stress intermediate. The stress intensity will therefore be:

$$\left|\sigma_t - \sigma_r\right| = \frac{2\,a^2\,b^2}{b^2 - a^2}\,\frac{p}{n^2}\,, \qquad (18)$$

which is maximum at the inside surface of the cylinder, n=a. This requires that:

$$\frac{2\,b^2}{b^2 - a^2}\,(\,p\,) \leq S_{mt}\,. \qquad (19)$$

Substituting a=r, b=r+t leads to determination of the minimum thickness for this case:

$$t_{min} = \left(-1 + \frac{1}{\sqrt{1 - 2p/S_{mt}}}\right) r\,. \qquad (20)$$

This is slightly larger than the minimum thickness with the thin wall assumption and will be used when $t \geq 0.1\ r$.

B. Thermal Stress

Heat loads of the magnitude expected at the divertor target introduce steep temperature gradients in target material. Cyclic operation induces large temperature changes between plasma burn and chamber rejuvenation periods. The result of these conditions is sizeable thermal stresses which dominate the total stress calculations.

Careful design is necessary to minimize the external constraints on material expansion under heat load. Self-constraint is, however, unavoidable and must be considered in determining the peak stress to which the material is subjected. For sections of a plate or thin walled cylindrical target sufficiently far from the edge attachments,

under steady state conditions, the temperature profile may be assumed to be nearly linear from the high temperature heated surface to the low temperature cooled surface. For a plate constrained against bowing and for a cylindrical tube, the peak thermal stress will be:

$$\sigma_{th_{peak}} = \frac{E \alpha \Delta T}{2 (1-\nu)} , \quad \text{(Ref. 40)} \qquad (21)$$

compressive on the hot surface, tensile on the cold. The difference in temperature may be expressed in terms of the heat flux, wall thickness and conductivity:

$$\Delta T = \frac{q" t}{k} . \qquad (22)$$

Thus a simple expression relating the maximum thermal stress, the heat flux, and wall thickness is:

$$\sigma_{th_{peak}} = \frac{E q" t \alpha}{2 k (1-\nu)} . \qquad (23)$$

Thermal stresses at edge connections become difficult to determine analytically and require specific study for particular designs. Except in the cases of a free edge or specific designs in which the edge attachments deflect readily, edge connections will cause a rise in stress over the "infinite wall" case. Equation 23 is therefore an optimistic estimate of the thermal stresses to be encountered.

C. Fatigue

The base case heat load cycle considered in this analysis consists of a 90 second burn followed by a 15

second quiescent rejuvenation period. As a result, over 10^5 cycles are likely during one year's operation, introducing the likelihood of fatigue failure as a controlling design consideration. This may be treated using semi-empirical fatigue-life curves for several candidate materials in conjunction with ASME Code rules for peak stress analysis. The number of cycles anticipated dictates that the fatigue will be strain-cycle controlled.

Analysis of the time dependent temperature profile through the target material indicates the temperature and strain ranges through which the material is cycled. Considering a semi-infinite body whose surface is exposed to periodic temperature cycling, the fraction of the surface temperature fluctuation experienced at a depth, x, is

$$\Delta T_x / \Delta T_o = \exp \left(- \sqrt{\frac{\pi}{\omega a_t}} \right) , \qquad (24)$$

where ω is the period of oscillation, and a_t is material thermal diffusivity. This suggests that thermal strains inside the material might be less than calculated using steady state equations, due to the oscillating heat load.

The divertor target is not infinite, however, and is more closely modelled by a slab with fixed temperature, T_c, on one side, and a surface heat flux on the opposite side, $q"_s$, which follows a periodic step function as in Figure IV-1.

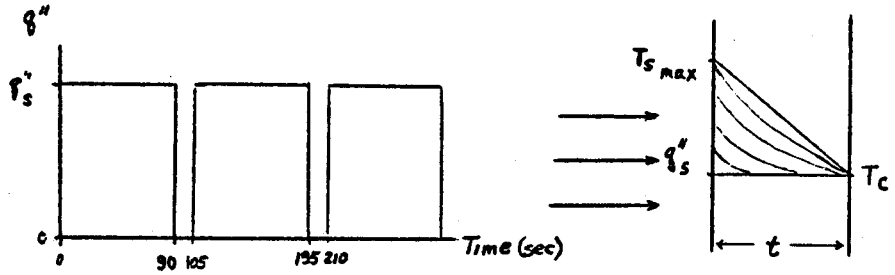

Figure IV-1

The time required to reach an essentially steady state temperature profile after a step change may be determined from the integral technique as (Ref. 41):

$$\tau_o = \frac{t^2}{6\,a_t} . \qquad (25)$$

For practical slab thicknesses (1 to 10 mm) and the eight materials considered in the analysis, these response times are at least an order of magnitude less than fifteen seconds. Fatigue strain ranges are therefore calculated based on full temperature cycling between a steady state burn condition and a steady state off condition.

Data for strain-cycle fatigue life curves is found in References 42, 43, and 44. Peak stresses determined as a combination of the pressure stress and thermal stress on the structure are converted to equivalent strains by use of the material modulus of elasticity, E. The cyclic component of these peak strains must be kept below $\Delta\epsilon_{max}$, that strain which will cause fatigue failure over the life-time specified. Substituting $\sigma_{th_{peak}} = E\,(\Delta\epsilon_{max})$ into equation 23 and rearranging gives a limit on wall thickness

such that:

$$t \leq \frac{2\,k\,(1-\nu)\,\Delta\epsilon_{max}}{\alpha\,q''} \quad . \qquad (26)$$

This is in conflict with the thicker channel walls favored by the sputtering consideration, and leads to an optimum thickness for either (1) maximum allowable heat flux for a specified lifetime, or (2) maximum life at a specified heat load. Determination of these optimum thicknesses is undertaken in Chapter V, and is the major factor in the design limitations reflected in the conclusions of Chapter VII.

D. Thermal Shock

During the transient periods of burn initiation and quenching, a non-linear thermal gradient will exist within the target material. This will introduce additional mechanisms of fatigue failure. The extremely steep temperature gradient at the heated surface immediately after burn initiation may result in cracking of the surface, with possible spalling and accelerated sputter damage. The frequently quoted thermal shock parameter, $\sigma_{max}(k\,c_p\,\rho)^{.5}/E\alpha$, gives a measure of material's relative survival in such an environment (Ref. 45). Work by Schivell and Grove (Ref. 46) indicates the greatest magnitude of the additional stress due to thermal shock on a flat plate will be ~1/5 of the maximum steady state thermal stress, and will occur at a depth from the heated surface approximately 4/10 of the

total thickness. This location does not coincide with that of the peak steady state thermal stress (adjacent to the coolant), but the additive effects were thought to be significant. The thermal shock stress on the inside layer is ~1/10 of the steady state stress. Experimentation under cyclic high heat load conditions will be necessary to determine actual effects. For this analysis the shock stresses are assumed to consume a fraction of the fatigue life equal to $N/N_{0.1}$, where N is the number of cycles endured, and $N_{0.1}$ is the number of cycles to failure at 0.1 times the peak steady state thermal stress. For all the materials considered, the shock stress fraction of fatigue life is found to be negligibly small.

E. Temperature Limits

All materials are subject to limitations in operating temperature, necessitating careful design to prevent overheating. Though fatigue life and sputtering are here found to govern design wall thicknesses, the temperature restrictions posed by materials characteristics form a secondary design limitation which bounds the range of potential improvements.

The melting/sublimation temperature limit is inescapable. In normal operation it would occur first on the heated surface at the outlet end of the coolant flow, assuming a uniform axial heat flux. The limiting equation is:

$$T_{melt} - T_{in} \geq \frac{q''(r+t)}{k} \ln(1+t/r) + q''/h + \left(\frac{r+t}{r}\right) 2Lq''/\pi G c_p r \quad , \tag{27}$$

where:
$2Lq''(\frac{r+t}{r})/\pi Gc_p r = \Delta T_{1-2}$, the coolant temperature rise,

$q''/h = \Delta T_{film}$, with h as in equation 2, and

$\frac{q''(r+t)}{k} \ln(1+t/r) = \Delta T_{wall}$, the temperature difference through the channel wall (Ref.16).

Most materials display a distinct degradation in strength above a critical temperature, which may pose a design limit if the material supports a structural load. The limiting equation then would be similar to that above with T_{melt} replaced by T_{mech}. For the divertor application adequate strength for coolant containment is provived by the inner cooler layers of material. Therefore, degradation of strength in the outer layers is not considered limiting.

Coolant and plasma compatibility with structural materials imposes temperature limits as well. For maximum coolant temperature permissible to avoid excessive corrosion, T_{corr}:

$$T_{corr} - T_{in} \geq q''/h + (\frac{r+t}{r}) 2Lq''/\pi Gc_p r = \Delta T_{film} + \Delta T_{1-2} \quad (28)$$

Known corrosion temperature limits are tabulated in Figure IV-2.

F. Graphical Materials Data

Employing materials properties, equations 26, 27, and 28 may be plotted on heat flux vs. wall thickness axes for candidate materials as shown is Figures IV-3a to IV-3h. Two fatigue curves are plotted, representing different numbers of thermal cycles to failure. The pairs of curves

for melting and property degradation temperature limits represent the range of these limits resulting from changes in the heat transfer coefficient due to varied mass flux of coolant. Safe operating conditions with respect to each material constraint lie below the respective constraint line. To survive 10^5 thermal cycles, the wall thickness and heat load must plot below the 10^5 cycle fatigue curve. If fatigue cracking and property degradation can be accepted, (as in a protective tile bearing no loads), points below the melt limit would be acceptable.

Element	Gas Corrosion	Liquid Water Corrosion	Liquid Metal Corrosion
Beryllium	-Does not react w/ hydrogen up to 2050°F -Attacked by steam above 500°F	-Good resistance to water up to 500°F	-Good resistance to liq. metals -Resists lithium to 1110°F
Aluminum	-Hydrogen doesn't diffuse and has no corrosive effect	-Good resistance -Protective film forms in water	
Titanium	-Hydrogen absorbed interstitially above 600°F	-Excellent resistance to 600°F	-Limited resistance to lithium above 1470°F
Vanadium	-Hydrogen embrittles above 570°F	-Modest corrosion in water	-Poor resistance in general -No tests on lithium
Copper	-Hydrogen embrittles above 650°F	-Excellent resistance to water	
Niobium	-Easily oxidized -Reacts easily w/ hydrogen	-Good resistance to 560°F	-Good lithium resistance to 1650°F
Molybdenum	-Oxidizes rapidly above 1000°F	-Limited applications in degassed water to 600°F	-Good lithium resistance to 1830°F
Graphite	-Rapid methane production from 670-1310°F -Rapid acetylene production above 2100°F		

Figure IV-2: Material Corrosion Summary (Ref. 36)

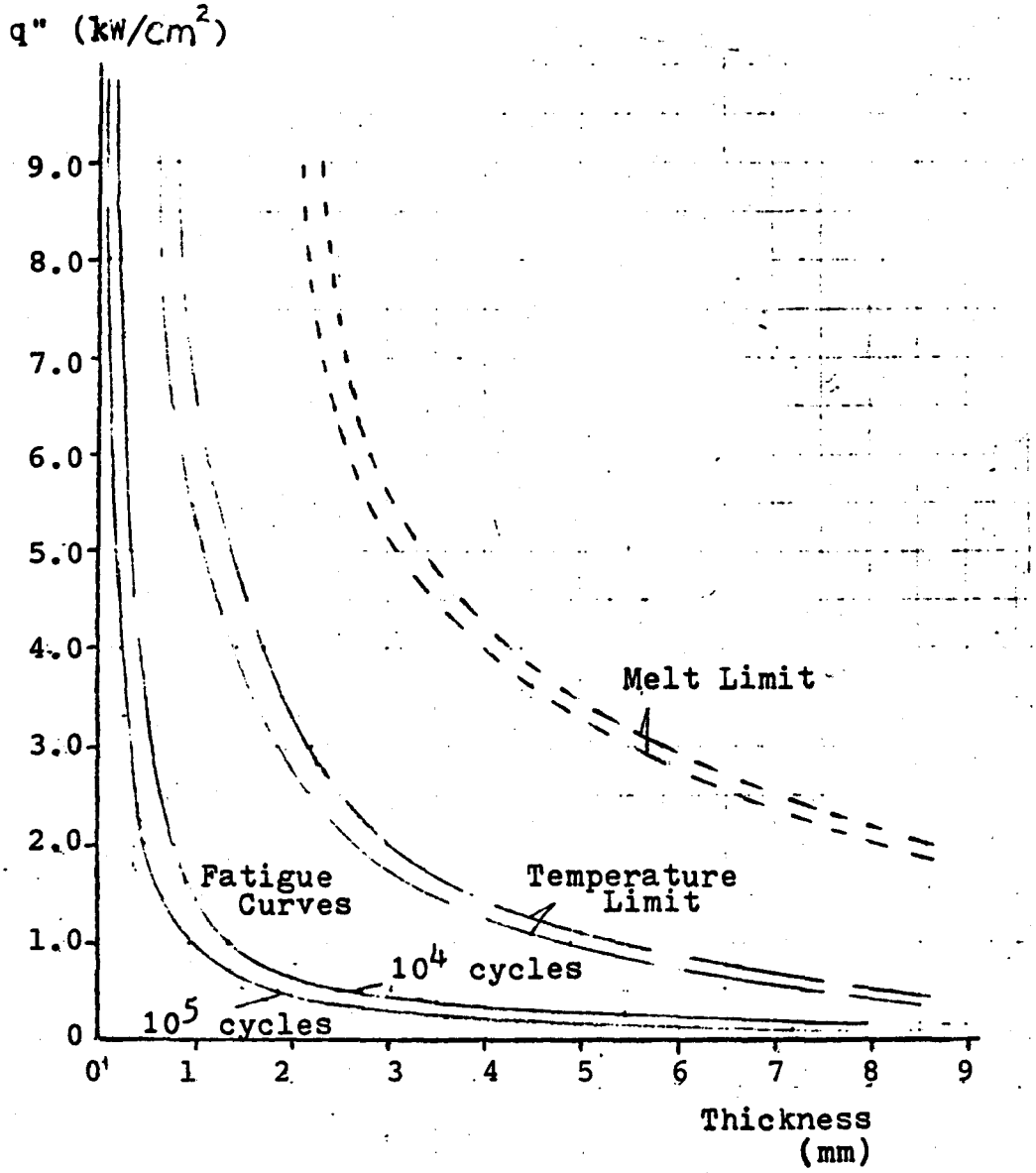

TZM Molybdenum Alloy

Figure IV-3a: Fatigue, Property Degradation, and Melting Limit Curves for TZM (Area Below Curves Acceptable)

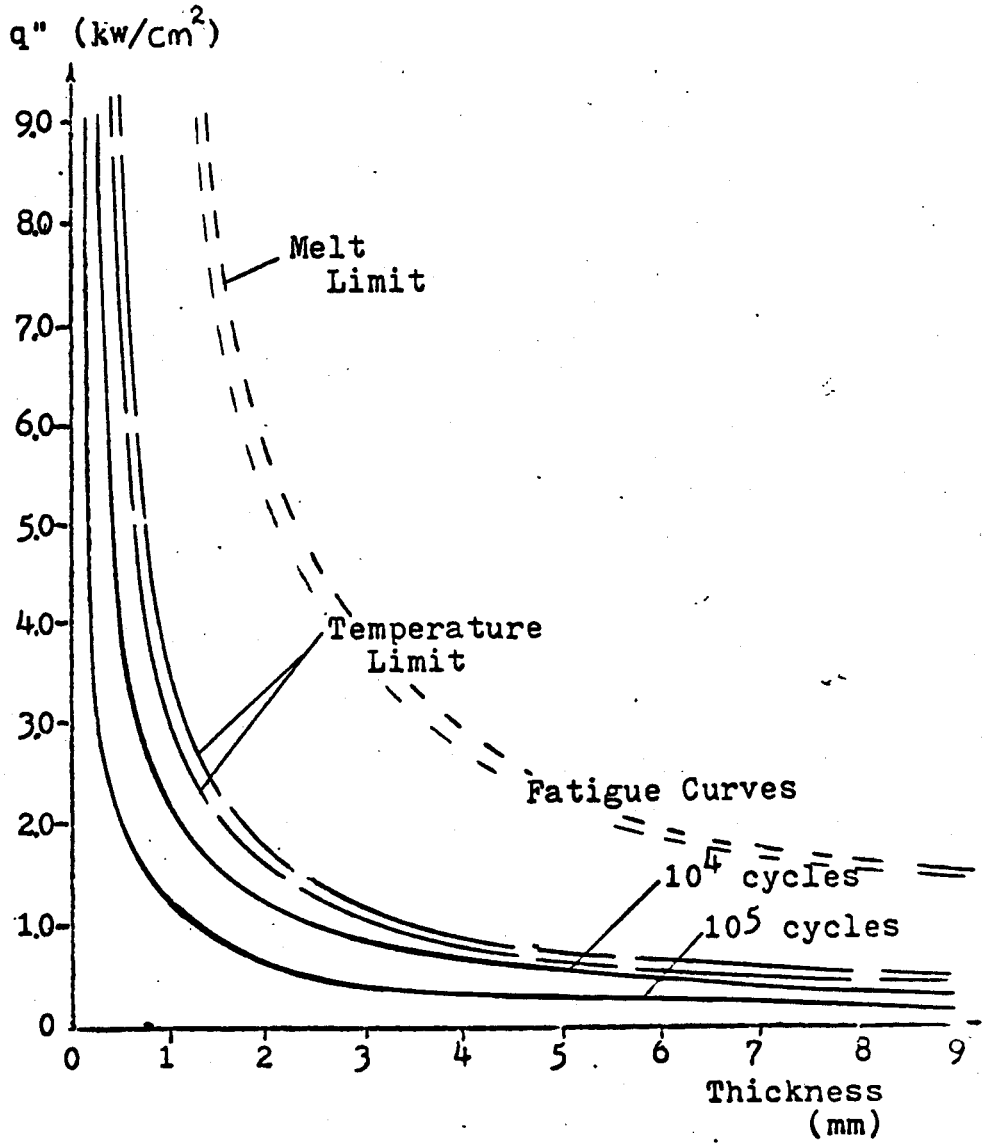

D-43 Niobium Alloy

Figure IV-3b: Fatigue, Property Degradation, and Melting Limit Curves for D-43 Niobium Alloy
(Area Below Curves Acceptable)

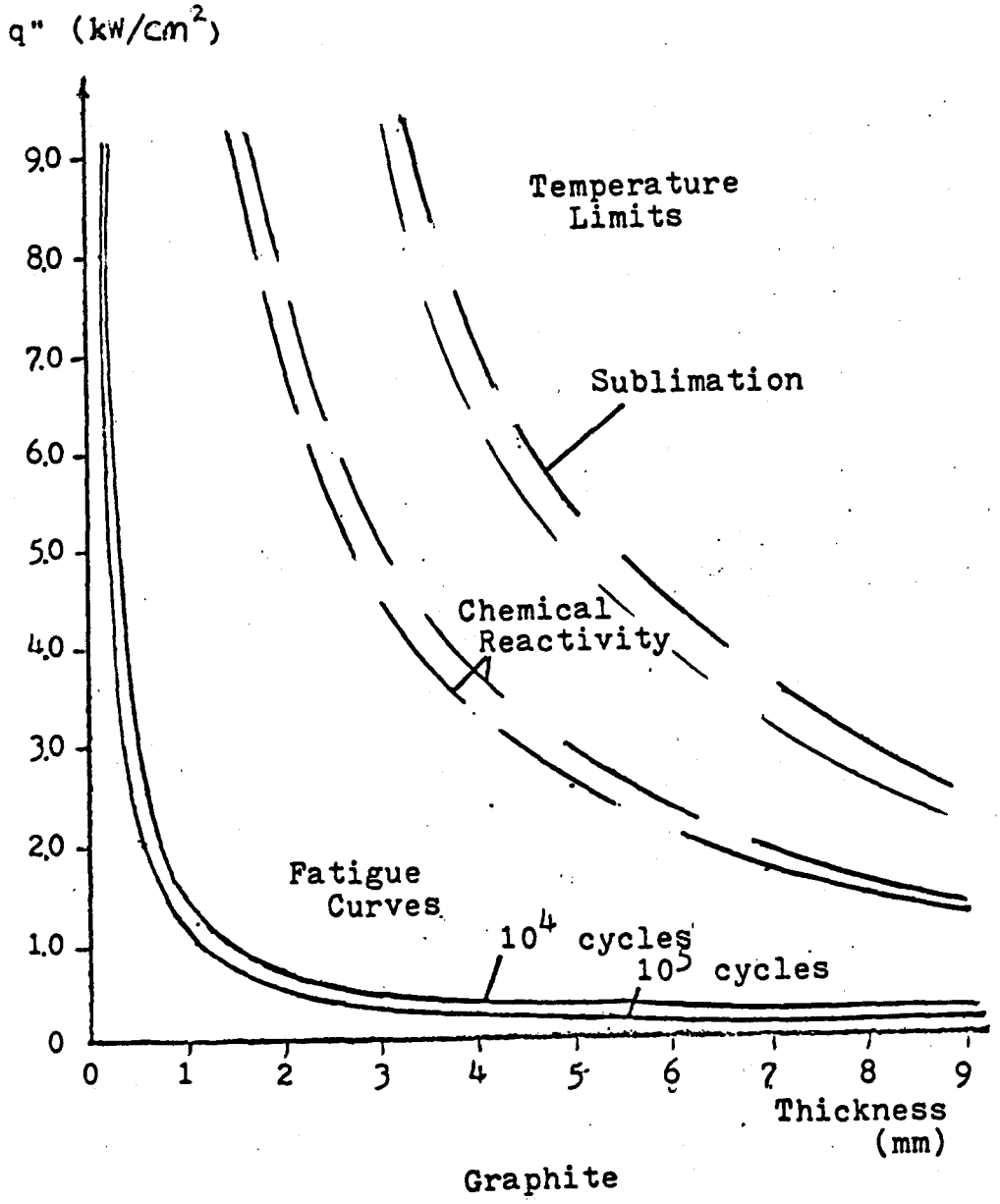

Figure IV-3c: Fatigue, Chemical Reactivity, and Sublimation Curves for ATJ Graphite (Area Below Curves Acceptable)

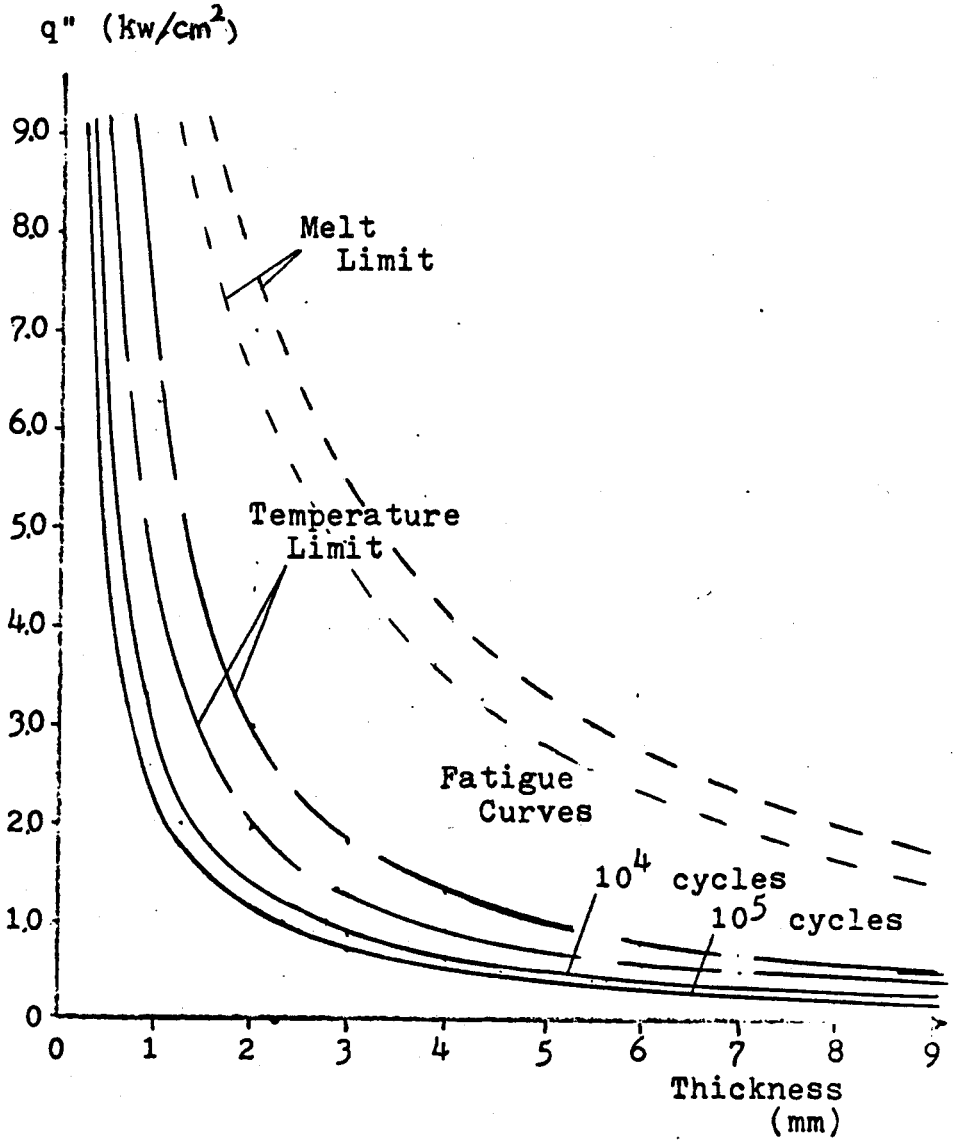

Figure IV-3d: Fatigue, Property Degradation, and Melting Limit Curves for Beryllium
(Area Below Curves Acceptable)

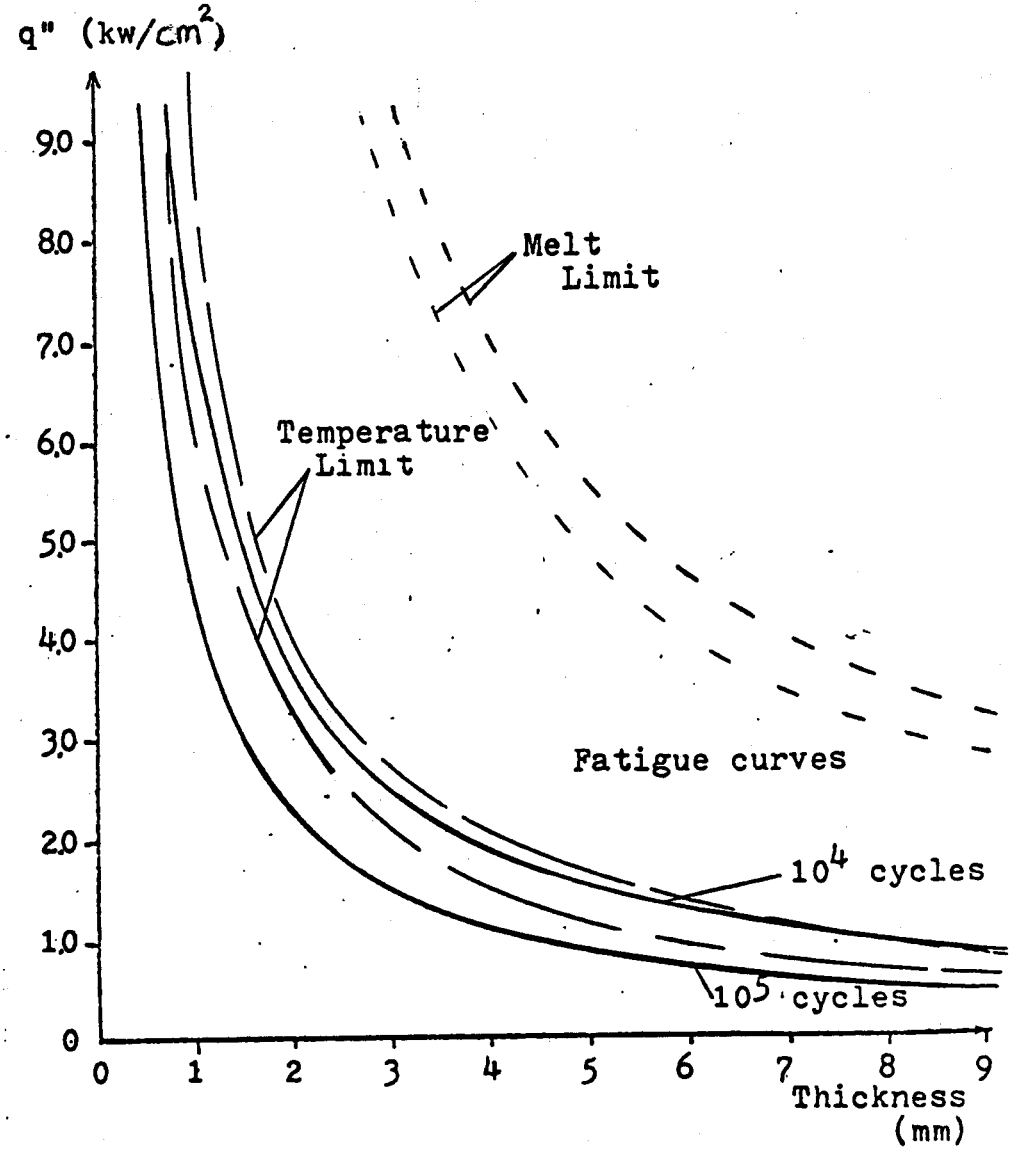

ZAC-2, Copper Alloy

Figure IV-3e: Fatigue, Property Degradation, and Melting Limit Curves for ZAC-2 Copper Alloy
(Area Below Curves Acceptable)

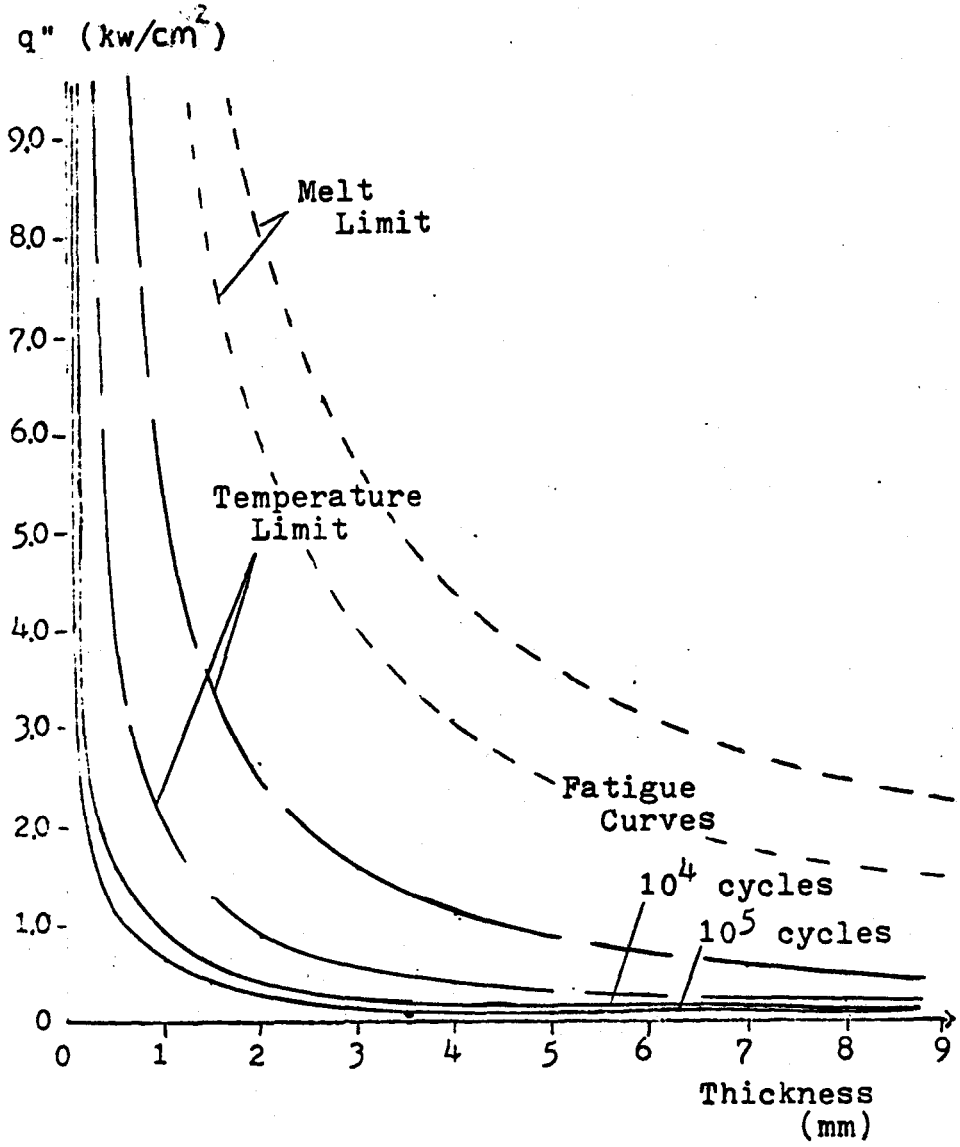

Figure IV-3f: Fatigue, Property Degradation, and Melting Limit Curves for Sintered Aluminum Powder (Area Below Curves Acceptable)

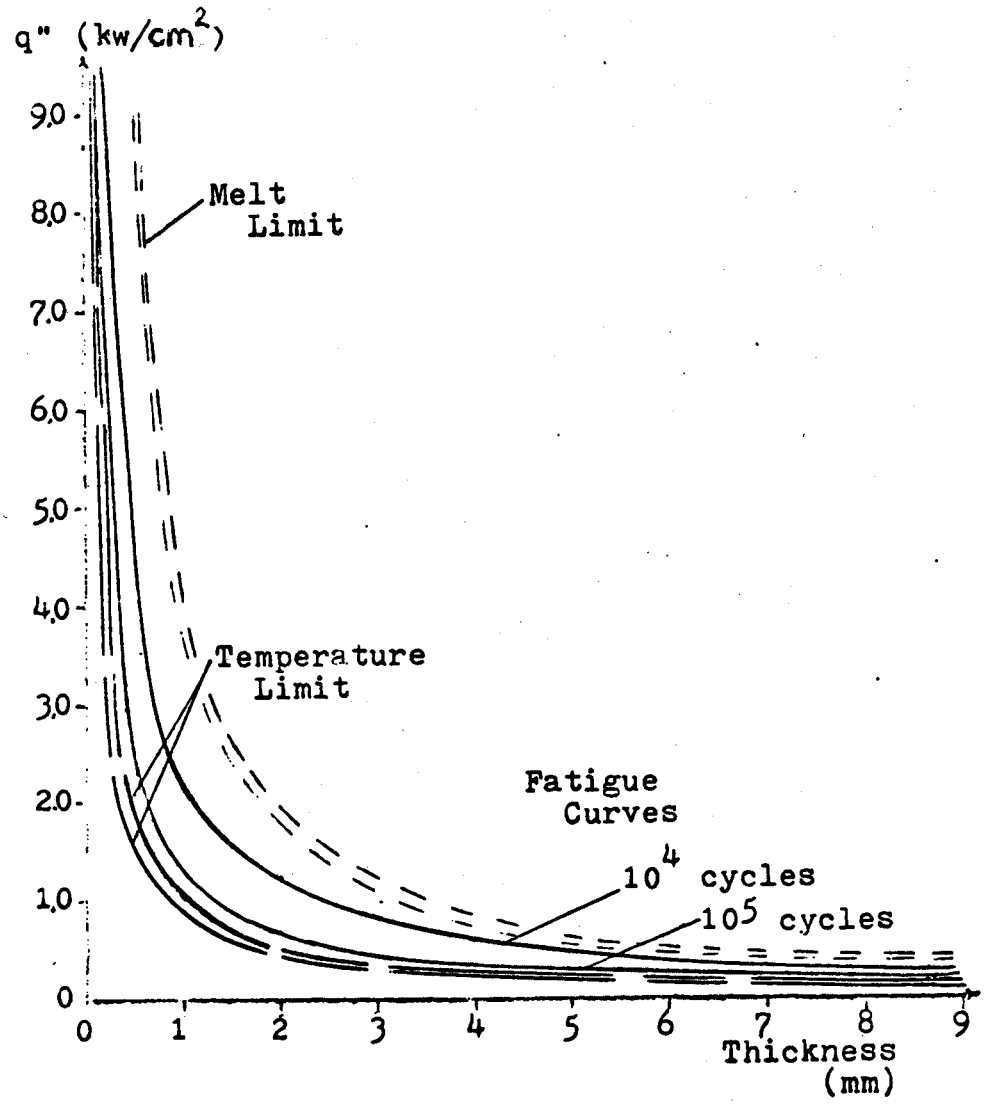

Vanadium Alloy

Figure IV-3g: Fatigue, Property Degradation, and Melting Limit Curves for Vanadium Alloy (V-25Cr-0.8Zr) (Area Below Curves Acceptable)

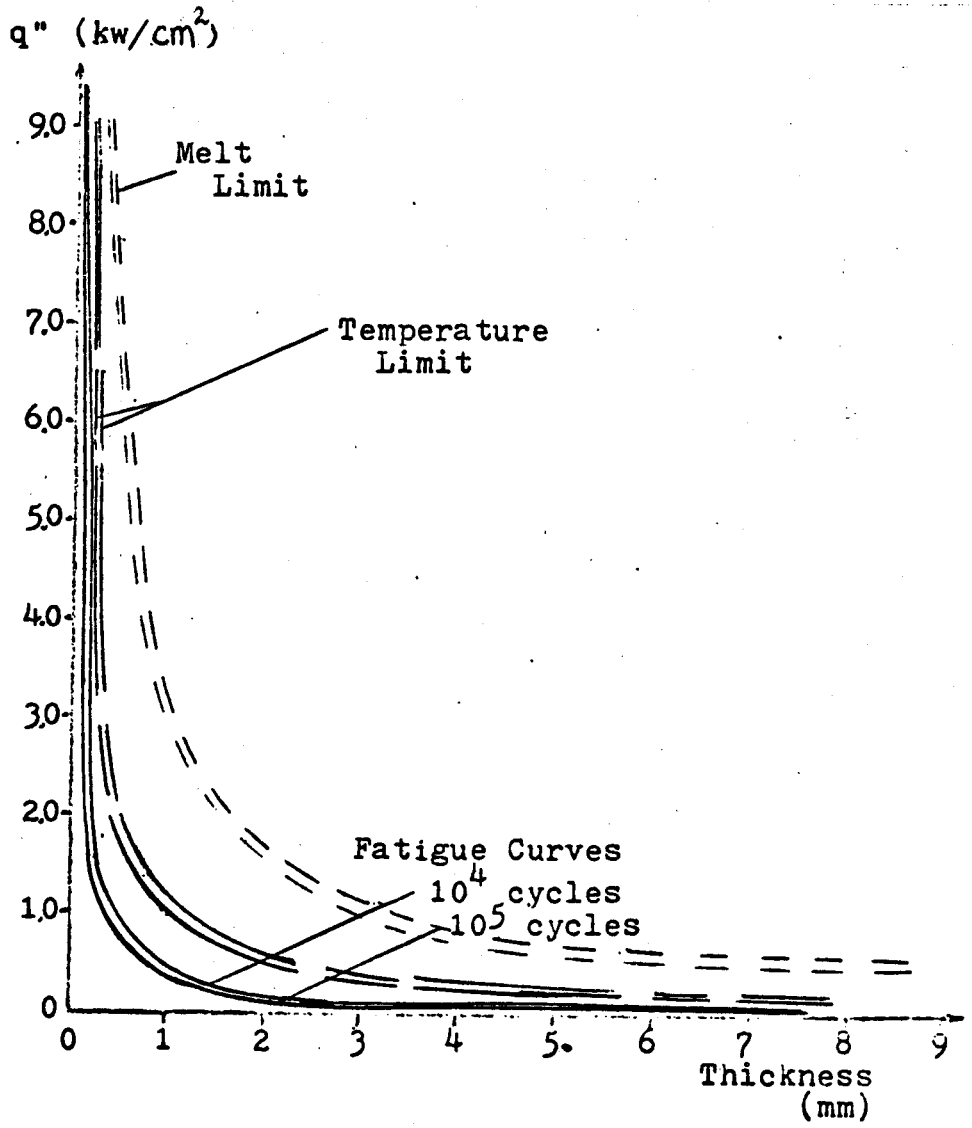

Ti-6Al-4V Titanium Alloy

Figure IV-3h: Fatigue, Property Degradation, and Melting Limit Curves for Titanium Alloy (Ti-6Al-4V) (Area Below Curves Acceptable)

V. EVALUATION OF DESIGN OPTIONS

A. Possible Geometries

A wide variety of solid target configurations are possible. The range of geometries depicted in Figure V-1 has been considered in this investigation. Each may be evaluated by applying minor modifications to the design equations already discussed. For analysis purposes, the concepts may be grouped into four more basic categories; Simple Tubes (A,B), Homogeneous Flat Plates (C,D), Composite Tubes (E), and Armored Plate Designs (F,G,H).

B. Materials

1. Functional Requirements

Identification of suitable materials for divertor target application is similar to the search for tokamak first wall materials. Strength and ductility are desirable to handle the thermal and pressure loads inherent in the system. Chemical compatibility with other materials in the machine, particularly coolant and plasma, must be considered. Further, for materials exposed to the plasma, resistance to hydrogen sputtering and self-sputtering must be sought. Minimization of plasma quenching effects due to impurity penetration of the plasma favors low Z materials. Resistance to thermal shock effects, fatigue damage, and radiation damage are additional desirable characteristics.

Materials offering some of the desirable characteris-

tics are numerous, and vast potential improvements through alloying may be available. An aggressive program of materials evaluation is warranted and ongoing to determine materials which meet all of the many criteria imposed on the divertor target. As a basis for analysis, eight structural materials representing a range of material characteristics are selected: Copper(ZAC-2), Sintered Aluminum Powder, Beryllium, Graphite, Molybdenum Alloy(TZM), Niobium Alloy (D-43), Vanadium Alloy(V-25 Cr-0.8 Zr), and Titanium Alloy (Ti-6Al-4V). Properties and their sources are summarized in Appendix A.

2. Limits on Data

Properties at elevated temperatures are available on only a limited basis. Where high temperature properties are unavailable, lower temperature values are used as the best available information. Such cases are indicated by the notes in Appendix A. Specific high temperature data will be needed and may be incorporated into the procedure as available to achieve a more precise design window delineation.

C. Particle Load vs. Lifetime Tradeoff

As noted in Chapters III and IV, sputtering and fatigue pose conflicting constraints on the allowable material thickness for any geometric configuration. The sputtering erosion curves of Chapter III and the fatigue limit curves of Chapter IV can be transferred to cycle life vs. wall thickness axes for various heat fluxes, as illustrated by figures V-2 and

V-3. Assuming that fatigue failure is unacceptable, design conditions must lie on or below both the sputtering and fatigue curves for a specified heat flux. The intersection of the fatigue and sputtering lines is seen to afford the greatest life. Plotting these optimum life points results in the design curves represented by the solid lines of Figures V-4 and V-5. The behavior of material optimum life and incident heat flux is apparent, and a quick determination of the target capabilities under a given heat flux may be made.

In Figures V-2 and V-3, the minimum thickness required to contain 1000 psi coolant in a 1 cm inner diameter tube is the origin of all sputtering lines. For a protective tile, not required to contain pressure, the sputtering lines would pass through the origin and have the same slope as in Figures V-2 and V-3. This improves the optimum life curves slightly, as shown by the dotted curves on Figures V-4 and V-5. From these tile curves, the optimum material performance limits of Figure V-6 may be found. Clearly, the goal of one year's survival under a one kw/cm^2 heat flux is not met by any of the materials. Particle delivered heat flux would have to be reduced to .25-.30 kw/cm^2, (perhaps by sloping the target or expanding the magnetic field lines) before a one year survival becomes reasonable.

D. Single Material Analysis

Simplicity of design and ease of manufacture favor a target formed of a single material. Composite structures are complicated by differential thermal expansion and chemical compatibility considerations. Accordingly, analysis of a simple tube and a simple flat plate with internal coolant channels is first undertaken.

1. Tube Design

Analysis of a single homogeneous tube is achieved by the following steps. The tube is considered to be one of many in a uniform array, operating under the base case conditions described in Chapter 1. End effects are initially neglected.

a. Thermo-hydraulic design limits are first specified.

1) The operating limit due to critical heat flux is established using the modified Lowdermilk CHF correlation from Chapter II, equation 7. (This equation uses British Engineering Units.)

$$G_{crit} = \frac{90\left[\frac{D^{.05}L^{.15}\,q''}{1400}\right]^2 + \left[\frac{4\,q''\,L\left(\frac{t+r}{r}\right)}{\pi D\,c_p}\right]}{(T_{sat} - T_{in})} \quad (7)$$

2) The pumping power constraint discussed in section II-C is applied.

$$\frac{\Delta p}{\rho c_p \Delta T_{1-2}} \leq .02 \quad (11)$$

3) Clearest visualization of the hydraulic design

window is afforded from a plot of constraints on a coolant temperature rise, ΔT_{1-2}, vs. channel radius, r, set of axes. From equations 7 and 10, the critical heat flux and pumping power ratio limits may be expressed respectively, in British Engineering units, as:

$$\text{CHF}: \quad \Delta T_{1-2_{crit}} = (T_{sat} - T_{in}) - \frac{90}{G_c}\left[\frac{(S.F.)q''\, D^{.05} L^{.15}}{1400}\right]^2 \tag{29}$$

$$W_p = .02: \quad \Delta T_{1-2_{W_p}} = \frac{.637\, K^{.357}\, L\, q''^{.643}}{\rho_f\, r^{1.071}\, W_p^{.357}} \tag{30}$$

where;

$$K = \frac{.063\,(\mu_b)^{.2}\,(\rho_f)^{1.8}}{778\; g_c}\left(\frac{\mu_w}{\mu_b}\right)^{.25} \tag{30a}$$

These curves are plotted for base case conditions, and appear as shown in Figure V-7.

b. Thermo-mechanical limits for each material are next established.

1) The minimum wall thickness required to contain internal pressure is found from equation 20 as a function of radius.

2) For incremental values of the tube radius, r, the thickness corresponding to optimum life for the specified heat load is derived from the procedures of section V-C. (The goal of one year survival must here be reduced to a quest for longest possible life.) Increasing the tube radius raises the thickness required to resist hoop stress, and shortens the optimum life.

3) An upper boundary on tube radius is established when the resulting tube life falls to 10 days.

4) To facilitate manufacture and avoid the possibilities of bubble blockage in the tube, a minimum tube radius is selected as .2 cm.

5) A check is made of the temperature limits at the tube exit in accordance with equations 27 and 28, section IV-E. An upper bound on ΔT_{1-2} is thereby established, which is the lesser value of:

$$\Delta T_{1-2_{melt}} = T_{melt} - T_{in} - \frac{q''(r+t)}{k} \ln(1+t/r) - q''/h \qquad (31)$$

$$\Delta T_{1-2_{corr}} = T_{corr} - T_{in} - q''/h \qquad (32)$$

c. The design window boundaries are plotted for each candidate material, as illustrated in Figure V-8a. Materials can be compared by plotting the window for fixed life, as in Figure V-8b. This constitutes the simple tube design window. Regions within the window are acceptable from a hydraulic and mechanical standpoint, though tube life decreases with increasing radius.

2. Plate Design

Assuming that plates are restrained from bowing but can expand in directions parallel to their surface, essentially the same analysis can be performed for the flat plate as was performed for the tube. An assumption of rectangular coolant channels would require greater wall

thicknesses to resist internal pressure. Circular channels may result in added thermal stress in the thick material between tubes. This increased stress could be relieved by sloped grooves in the face of the plate, so that the tube analysis remains an appropriate procedure. In this configuration, the spacing between channels is independent of the thickness facing the plasma. The channel spacing may be selected to optimize the conduction to the rear of the channel, reducing pumping power requirements per unit area of target. Since sputtering and fatigue will affect the plasma facing wall in the same way as the tube, the mechanical temperature and radius limits will be identical to the tube case. The design window would appear as in Figures V-8.

E. Composite Material Analysis

The diverse demands for material resistance to sputtering, fatigue, and erosion, and for compatibility with plasma and coolant, suggest that some blend of materials may best suit the divertor purpose. As seen in the previous section, no single material offers adequate properties for all constraints in the base case design.

Analysis of composite designs encompasses all the considerations of the single material targets. In addition, the effects at interfaces between different materials must be assessed.

1. Coated Tube Analysis

Based on the results of section V-D, the concept of

adjacent tubes was seen to be somewhat less desirable than circular channels in a flat plate, since the thickness of tube walls to resist sputtering was linked to the spacing between coolant channels. Very thick tubes would result in an increased heat load per channel. However, if sputtering resistance could be provided by an appropriate coating on the plasma side of a tube array, the heat load per tube could be fixed, and a coated tube array would be competitive with flat plate concepts by virtue of its production simplicity.

Thermohydraulic analysis would be identical to that of the simple tube case. The minimum wall thickness for the tube substrate is determined as before, based on the hoop stress consideration. The coating thickness must be given particular attention, in order that it neither crumbles due to fatigue nor is penetrated by sputtering. Norem and Bowers (47) report that a thickness of just 10 microns of beryllium should be sufficient to accomodate incident ions without sputtering from the substrate. They report that such a thin coating would be redeposited every 20 pulses, assuming adequate coating material is artificially introduced into the plasma edge. Such a thin coating should not be subject to thermal stress, since its surface would be rough on a scale of Angstroms (Ref. 47). The development of this sort of in-situ plasma-recoating of the target surface would virtually eliminate the sputtering limits, making the coated tube option more attractive.

2. Armored Plate Design

Thermohydraulic analysis of the armored plate would be identical to that of the simple flat plate. Thermo-mechanically, procedures would parallel the simple case, except that surface stresses arising at the interface between the two materials must be accounted for. If the armored tile is bonded to the substrate, the analysis illustrated by Figure V-9 affords a two dimensional indication of the resulting thermal stresses. For the substrate, the temperature difference through the thickness is:

$$\Delta T_1 = \frac{q'' t_1}{k_1} . \qquad (33)$$

Likewise, for the tile:

$$\Delta T_2 = \frac{q'' t_2}{k_2} . \qquad (34)$$

Were the plates unrestrained, they would appear as in Figure V-9c under a steady heat load. Imposing a plane strain condition on the plate leads to a virtual thermal strain as shown. The neutral plane through the plate will have displaced a distance X from its unheated position on the x axis due to thermal expansion. The virtual strain in the substrate is then:

$$\epsilon_1 = X - (\alpha_1 \Delta T_1 \frac{z}{t_1} + \alpha_1 \Delta T_1) , \qquad (35)$$

while that in the tile is:

$$\epsilon_2 = X - (\alpha_2 \Delta T_2 \frac{z}{t_2} + \alpha_2 \Delta T_1) . \qquad (36)$$

For the two dimensional plate, the stress in each region is then (Ref. 48):

$$\sigma_1 = \frac{E_1}{(1-\nu_1)}\left[X - (\alpha_1 \Delta T_1 \frac{z}{t_1} + \alpha_1 \Delta T_1)\right] \quad (37)$$

$$\sigma_2 = \frac{E_2}{(1-\nu_2)}\left[X - (\alpha_2 \Delta T_2 \frac{z}{t_2} + \alpha_2 \Delta T_1)\right] \quad (38)$$

For equilibrium we can set the sum of forces on the plate equal to zero and solve for the displacement X:

$$\text{Force} = 0 = \int_{-t_1}^{0} \frac{E_1}{1-\nu_1}\left[X - \alpha_1 \Delta T_1 - \frac{\alpha_1 \Delta T_1}{t_1} z\right] dz + \int_{0}^{t_2} \frac{E_2}{1-\nu_2}\left[X - \alpha_2 \Delta T_1 - \frac{\alpha_2 \Delta T_2}{t_2} z\right] dz \quad (39)$$

$$X = \frac{(1-\nu_2)\ \frac{E_1 t_1 \alpha_1 \Delta T_1}{2} + \left[\frac{E_2 t_2 \alpha_2 \Delta T_2}{2} + E_2 t_2 \alpha_2 \Delta T_1\right]\ (1-\nu_1)}{(1-\nu_2)\ E_1 t_1 + E_2 t_2 (1-\nu_1)} \quad (40)$$

This value of X may then be used to determine the strains and stresses from equations 35, 36, 37, and 38. Sample results appear as in Figure V-10. The peak strains so determined can be compared with the maximum allowable strain range for the specified material and design life. Conversely, the maximum allowable strain may be used in equations 33, 34, 35, and 36 , to determine the maximum allowable heat flux for a specified target thickness. In this way, fatigue curves on a life vs. thickness axis may be generated, the sputtering rate plotted, and optimum life vs. thickness curves obtained.

Analysis of six types of tiles (Aluminum, TZM, Beryllium,

Graphite, Titanium, and Vanadium) over a copper substrate were analyzed in this way. In all cases except aluminum, the tensile virtual strains in the tile were reduced over the unbonded plate. The compressive strains increased, but occurred in the first layers of surface to be eroded by sputtering. A modest improvement in the tile fatigue life should result from this strain reduction. The relatively high expansion coefficient of copper tends to mitigate the back side tensile strain of all candidate tiles except aluminum, reducing cyclic fatigue at the back of the tile. With remote replacement of tiles, the substrate and coolant channels would easily survive past the one year design goal. The relative ranking of material survival would be unchanged from Figure V-6, though life would be increased slightly.

3. Mechanically Unbonded Layered Plate Design

The foregoing analysis has revealed serious limitations on the lifetime and heat load constraints under which solid target configurations may operate. An upper limit on the ability of a solid target to survive may be evaluated by assuming a design which in effect takes full advantage of material temperature, sputter rate, and fatigue thickness constraints simultaneously. This is achieved by assembling relatively thin layers of armor material so that mechanical bonding between them is non-existent, while thermal bonding remains very good. Here a thin film of liquid lithium is postulated to separate the layers. Powdered graphite may be

an acceptable alternative. Each layer is thin enough to prevent fatigue failure during its survival time in the target. In this way successively thicker layers can be built upon the cooled backing, up to a thickness at which a temperature limit is approached. For most materials considered, this limit is the boiling point of lithium. The thickness of armor material thus assembled resists sputtering for the longest time possible for any target configuration.

The obvious price paid to reach this optimum life design is an increase in the complexity and difficulty in fabrication of the target. To effectively eliminate mechanical bonding between solid layers, the liquid lithium would require an expansion reservoir connected to each liquid layer. These connections may have to be valved in some way to prevent loss of lithium as sputtering penetrates to the depth of each lithium layer. Thus as few layers of lithium as possible would be desirable to simplify valve assembly.

Figure V-11 indicates the analysis of this optimum configuration for the eight candidate materials of this report. TZM affords the longest life at a 1 kw/cm^2 heat load; 261 days. Niobium (D-43) appears to be nearly as attractive at 258 days, perhaps more so since but four niobium layers are required as opposed to TZM's nine layers.

If an ideal lubricant between the layers ($k = \infty$, $T_{melt} = \infty$) were available the total wall thickness could be increased further, up to a thickness at which the outer surface

approaches the material melting point. This would improve the target lifetimes by roughly a factor of 2 over the values of Figure V-11. This extreme would probably be impractical, however, since the remainder of the divertor duct would become even hotter due to radiative heat transfer.

A. Adjacent Tubes

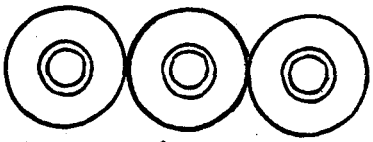

E. Protective Tubes Sheathing Substrate Tubes (Bonded and Unbonded)

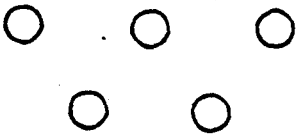

B. Spaced Tubes

F. Protective Coating Bonded to Plates

C. Plate with Milled Channels

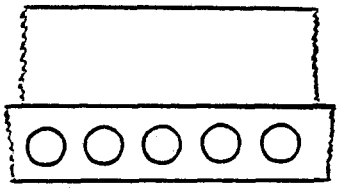

G. Protective Tile over Substrate Plate (Bonded and Unbonded)

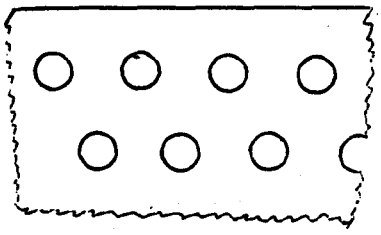

D. Consumable Target

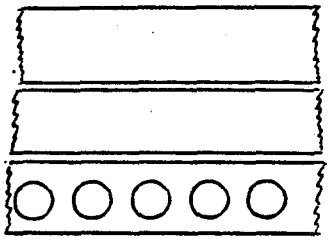

H. Thermally Bonded, Mechanically Unbonded Tiles over Plates

Figure V-1: Conceptual Solid Target Configurations

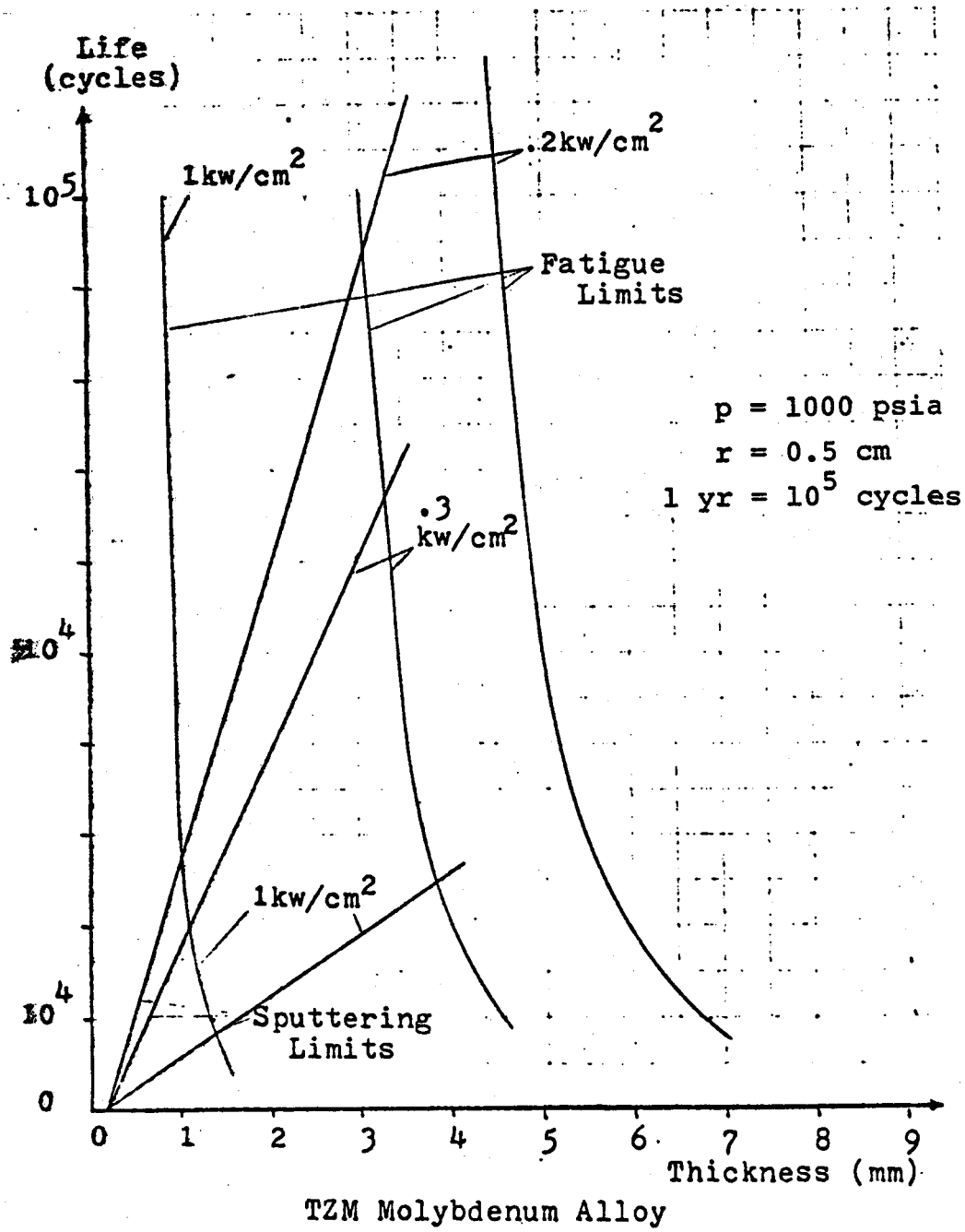

Figure V-2: Sputtering and Fatigue Curves Plotted for Various Heat Fluxes for TZM

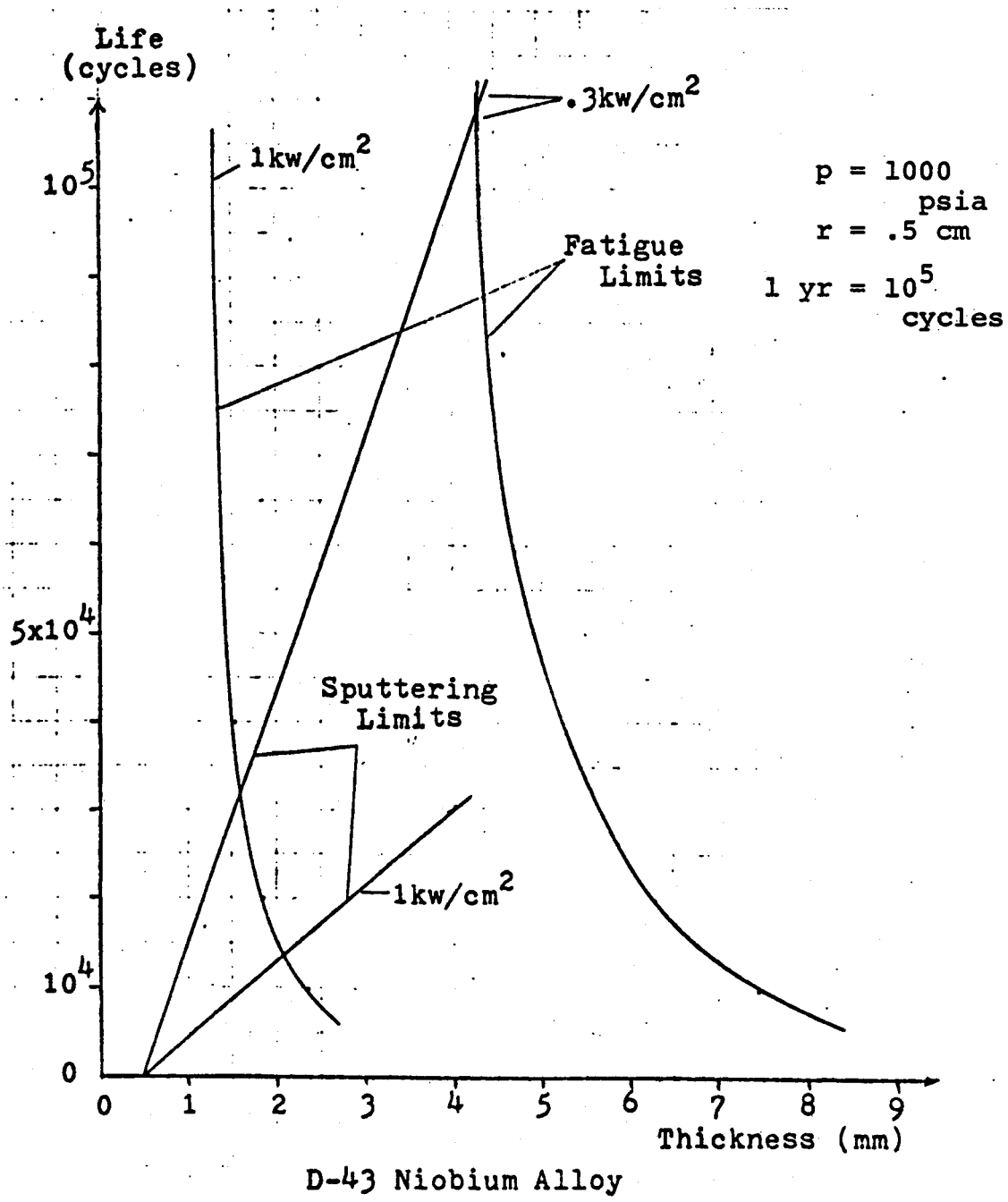

Figure V-3: Sputtering and Fatigue Curves Plotted for Various Heat Fluxes for D-43 Niobium Alloy

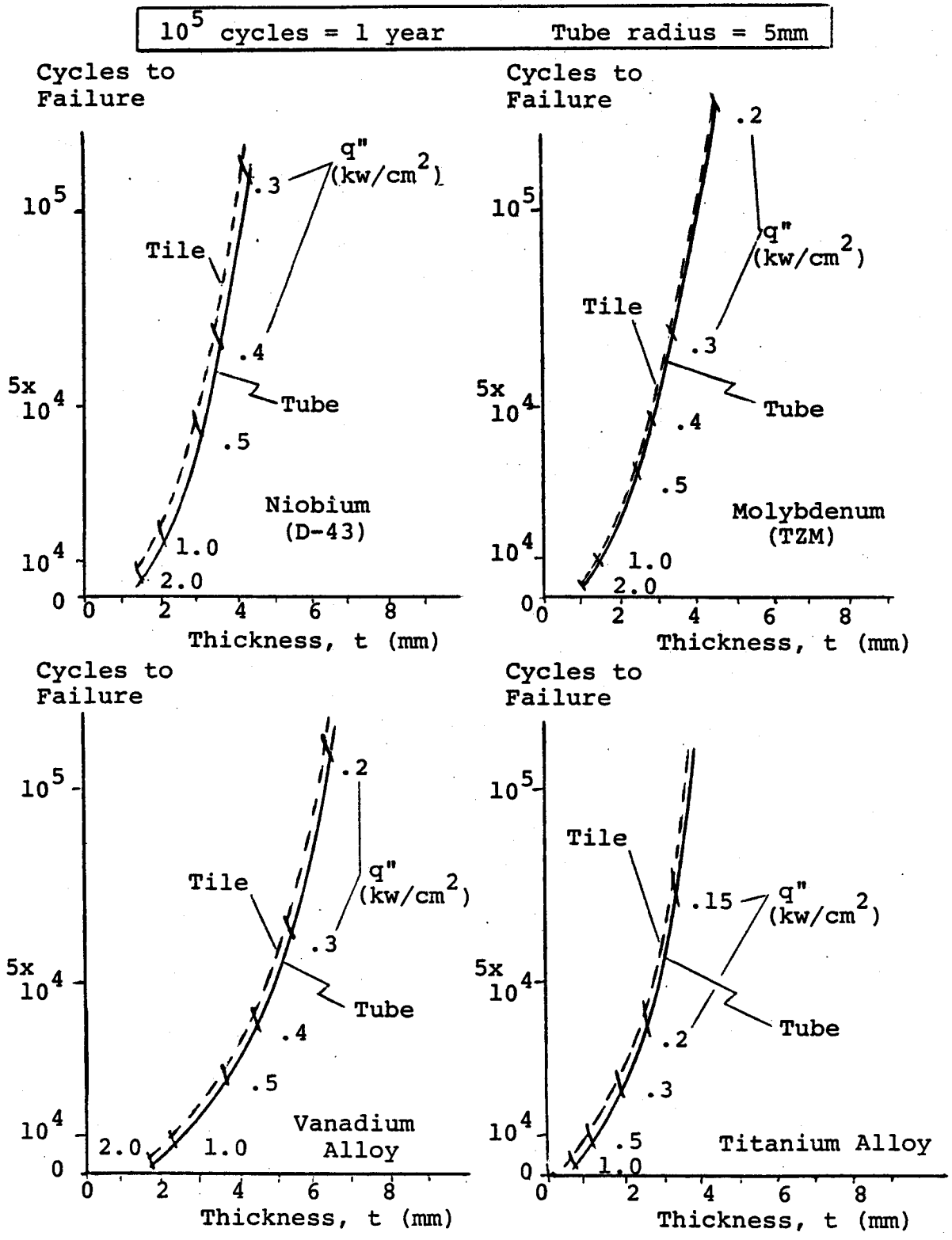

Figure V-4: Optimum Life and Thickness Curves for Candidate Materials Showing Effect of Varied Heat Flux

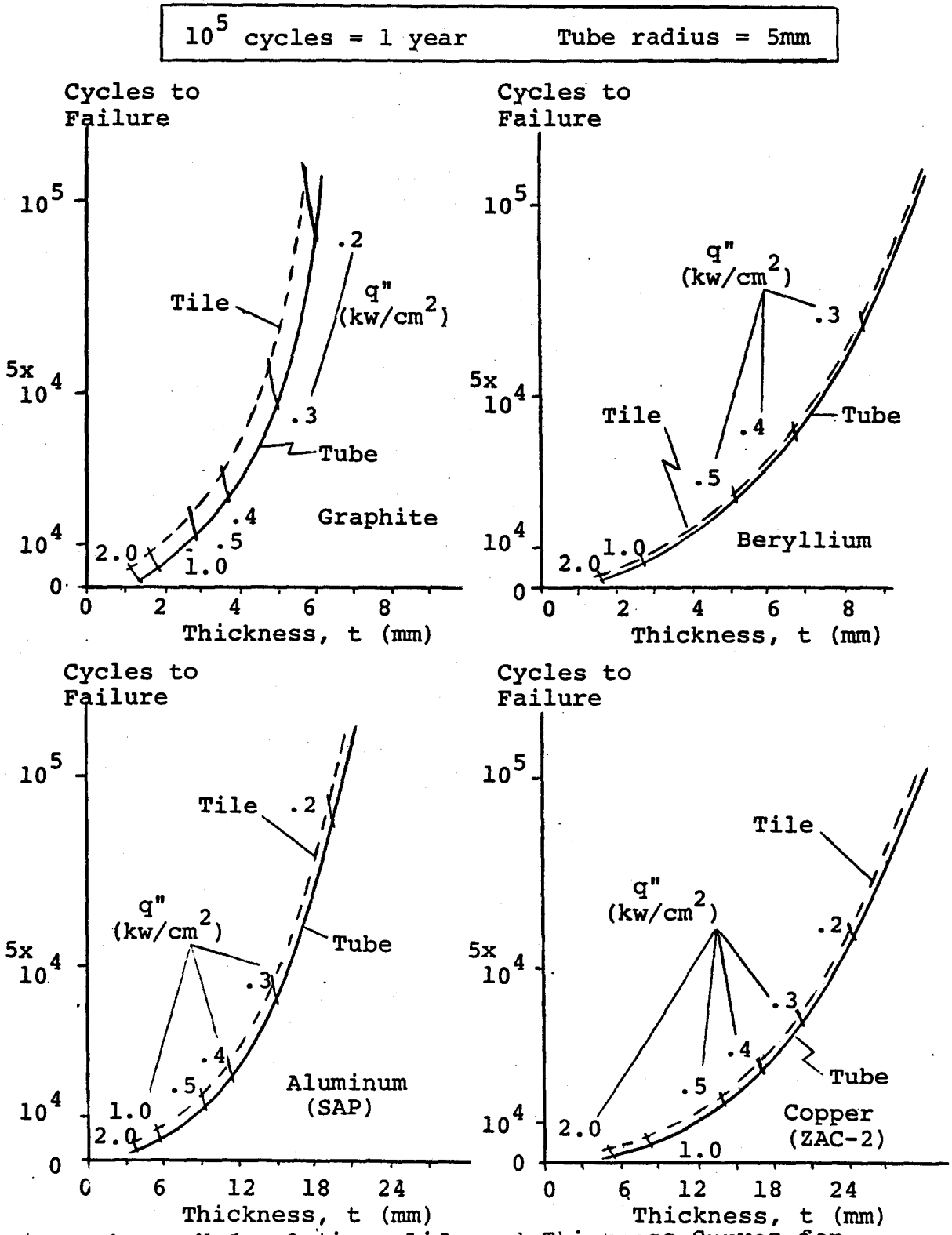

Figure V-5: Optimum Life and Thickness Curves for Candidate Materials Showing Effect of Varied Heat Flux

	Sputter Rate (mm/yr)	Column 1: 1 Year Life — Heat Load (kw/cm^2)	Column 1: 1 Year Life — Thickness (mm)	Column 2: 1 kw/cm^2 Load — Life (days)	Column 2: 1 kw/cm^2 Load — Thickness (mm)
Nb	11.3	.32	3.9	61	1.9
TZM	15.1	.24	3.9	36	1.4
V	28.3	.22	6.0	29	2.3
Be	43.1	.23	9.6	25	2.7
Al	103.9	.19	19.2	22	5.4
C_{gr}	26.9	.21	5.8	23	1.6
Cu	175.3	.17	26.8	21	8.2
Ti	27.4	.13	3.6	11	.5

Figure V-6: Optimum performance capabilities for candidate materials, configured as single flat tile constrained against bowing, and assuming no interfacial stress at joint with substrate.

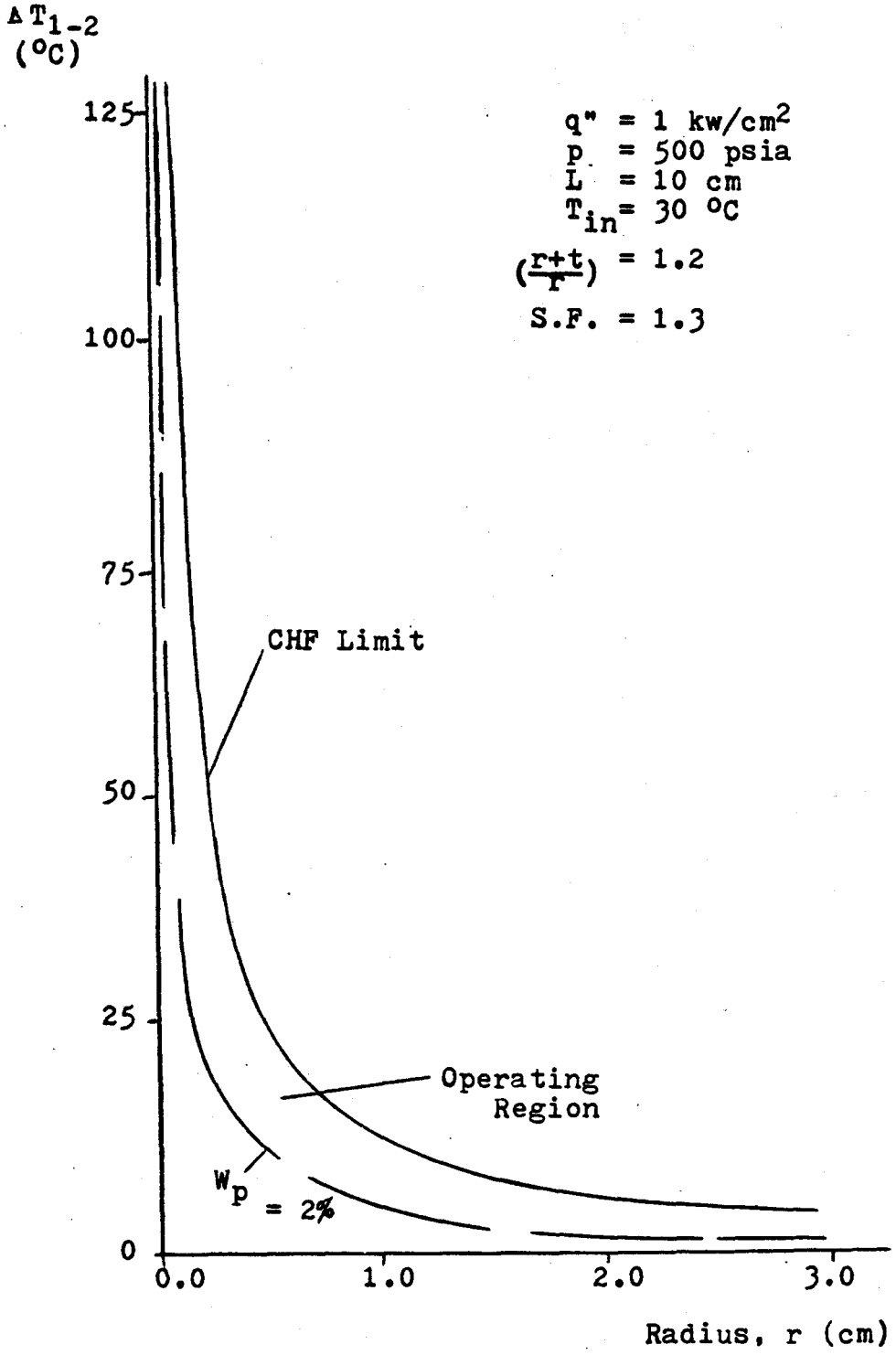

Figure V-7: Hydraulic Constraints for Design Window under Base Case Conditions. Mass Flux, G, Increases Toward Origin.

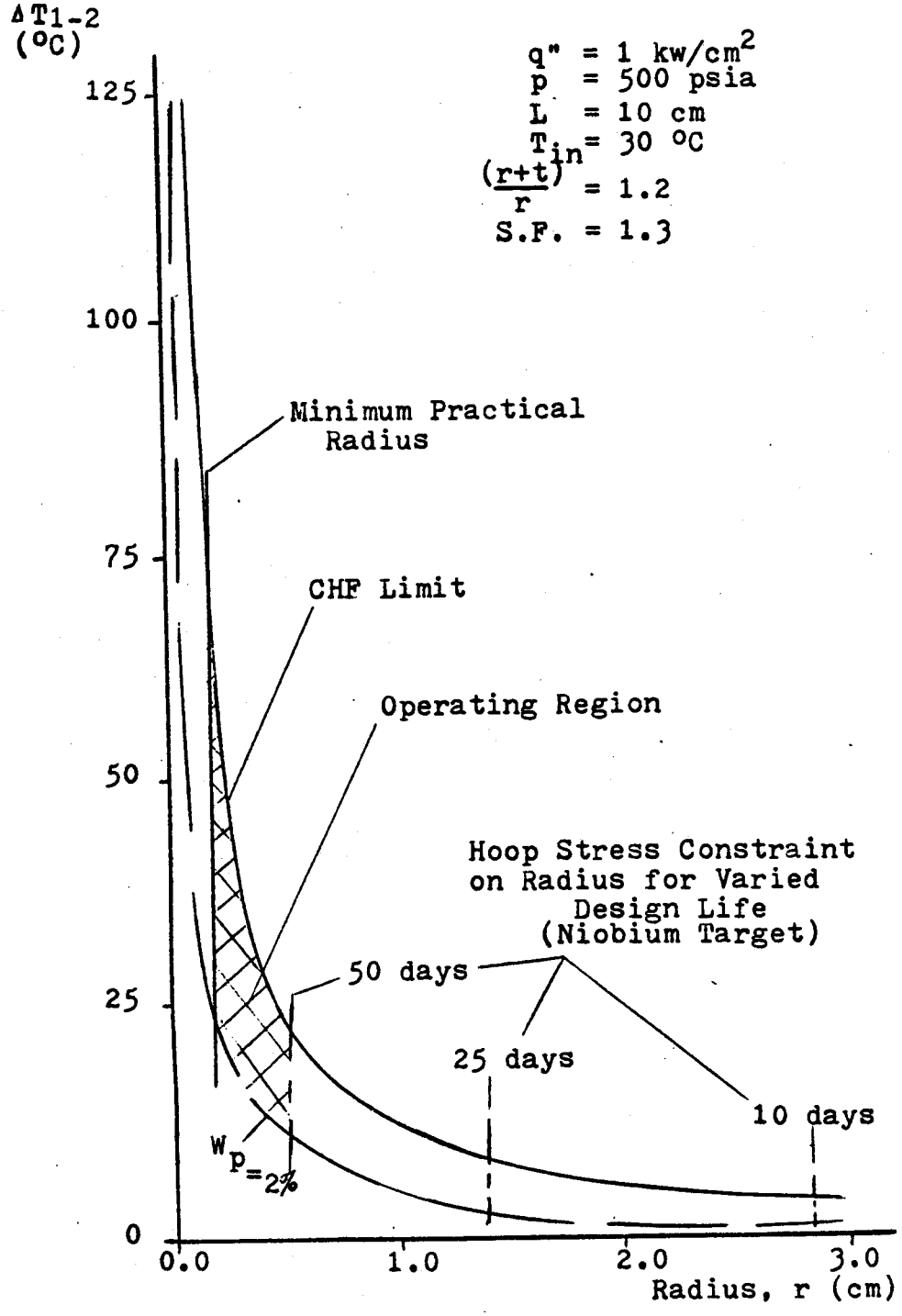

Figure V-8a: Design Window for Niobium (D-43) Plates and Tubes, Showing Relation between Life and Radius.
(Temperature Limits not Significant at High Subcooling)

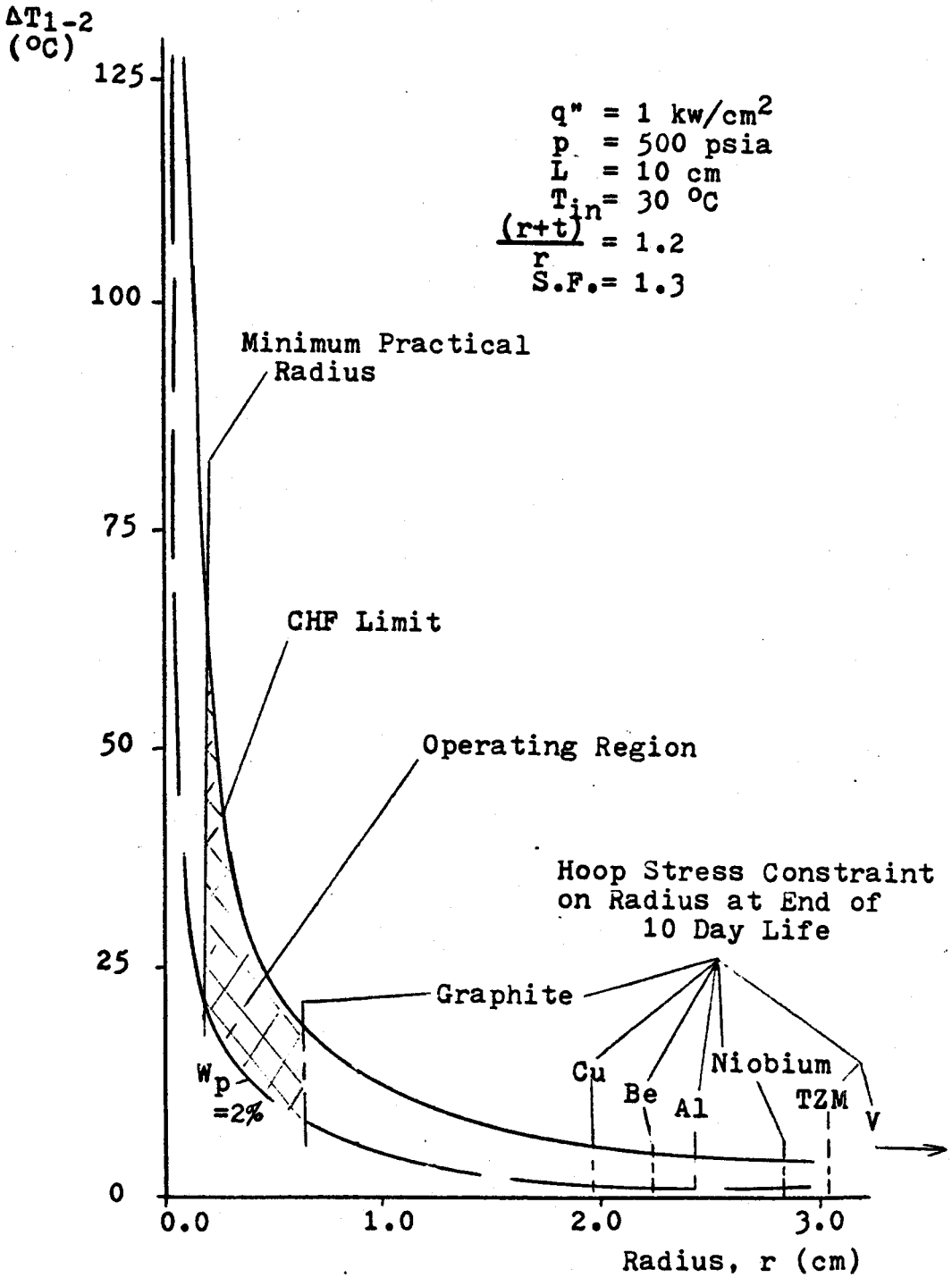

Figure V-8b: Design Window for Homogeneous Plates and Tubes Under Base Conditions. (Target Life Cannot Meet 1 Year Goal.) (Temperature Limits not Significant at Such High Subcooling.)

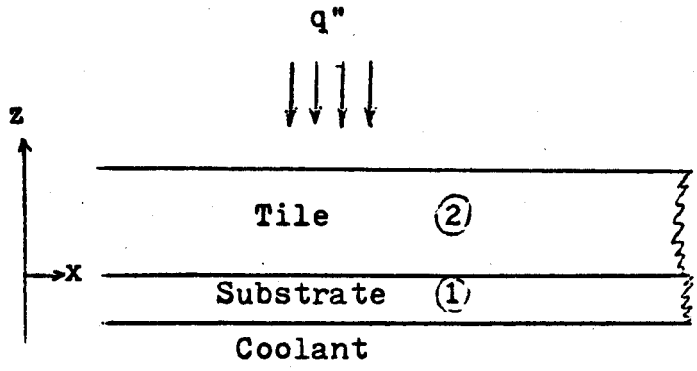

a.

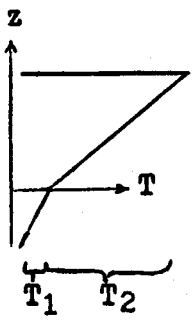

b. Temperature Profile

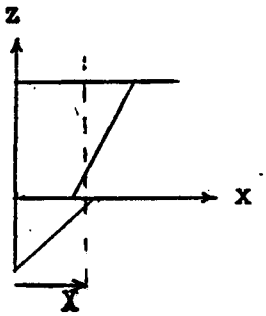

c. Thermal Expansion Unrestrained by Interface

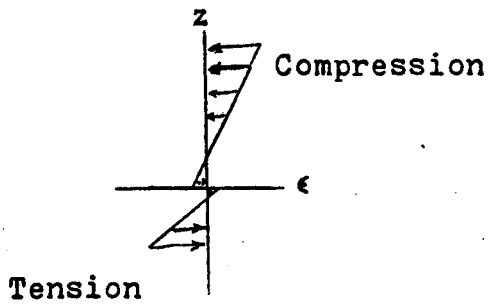

d. Virtual Thermal Strain

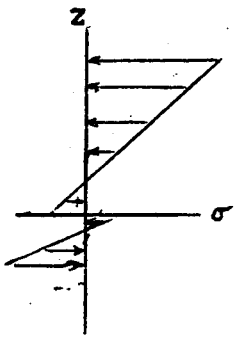

e. Thermal Stress (Sum of Forces = 0)

Figure V-9: Two Dimensional Stress in a Composite Plate with Ends Constrained Against Bending

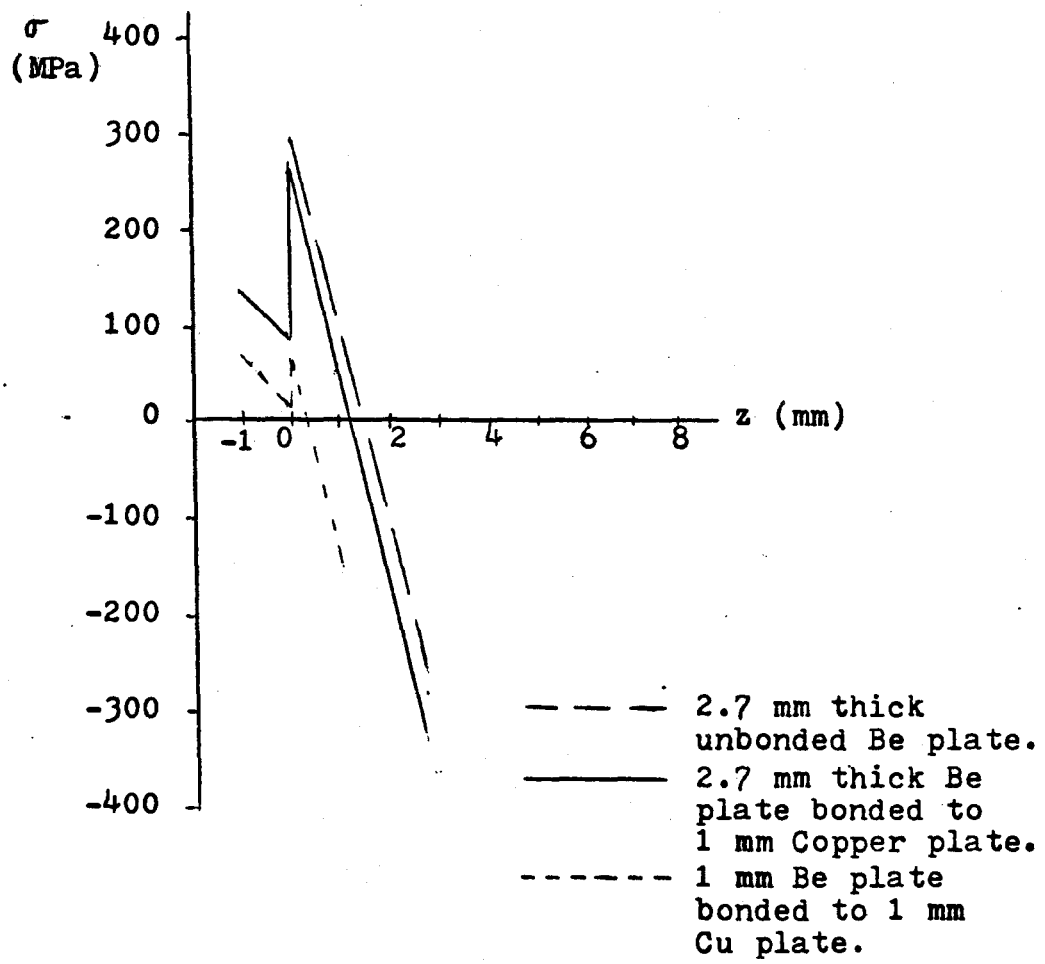

Figure V-10: Stress Profiles in Beryllium Tiles over Copper Substrate. Note Decrease in Tensile Stress at Back Layer of Tile as Result of Bonding. Some Lengthening of Fatigue Life would be Expected. (Effect of Increased Compression on Front Layer is Negated by Sputtering Erosion.)

Figure V-11: Mechanically Unbonded Layered Plate Design - Comparison of Material Performance and Component Lifetimes

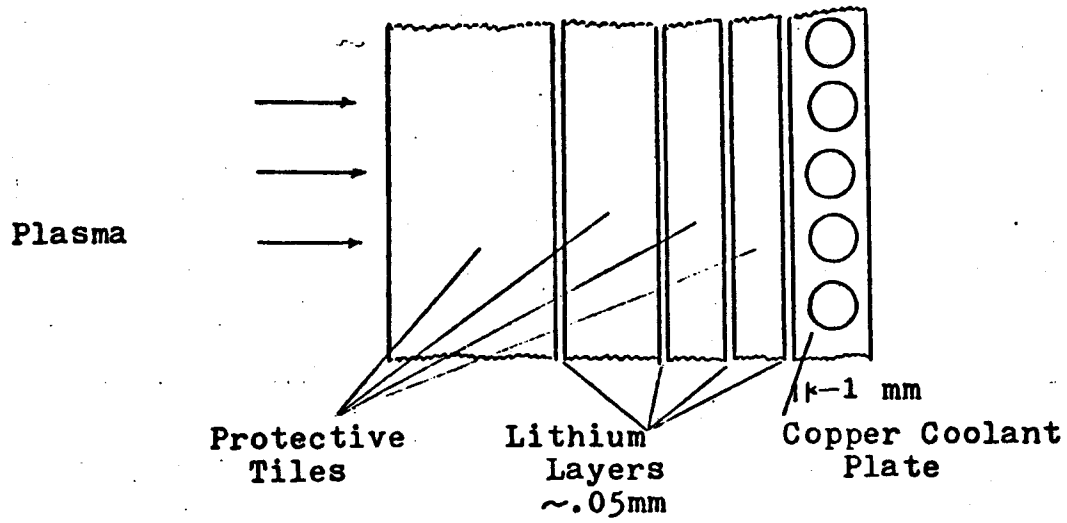

	Li	Be	TZM	C_{gr}	Nb	Al	V	Ti	Cu
Melt Temperature (^oC)	1347 Boil	1290	2610	3367	2468	631	1900	1668	1085
Sputter Rate at 1 kw/cm^2, C=.28 (mm/yr)	—	43.1	15.1	26.9	11.3	103.9	28.3	27.4	175.3
Avg Layer Thickness (mm)	.05	2.5	1.2	1.2	2.0	4.2	1.8	.4	6.0
Temperature Drop Across Layer (^oC)	10	132	124	120	357	233	600	229	192
Number of Layers Permitted	—	7	9	9	4	2	2	5	4
Life of Single Layer (days)	—	22.9	29.0	16.3	64.6	14.7	23.4	5.3	12.5
Total Lifetime (days)	—	160	261	146	258	29.4	46.4	26.6	50.0

VI. SENSITIVITY ANALYSIS

The base case parameters selected for the initial analysis in Chapter I are typical of the conditions currently being considered for divertor operation. The resulting design window provides a view of how much option space exists for these conditions. Much latitude exists for varying many of these parameters, however, in an effort to expand the design window and determine its behavior over a broad range of conditions. Further, uncertainty in the applicability of presently known physical behavior of coolants and structural solids at the extreme conditions anticipated suggests that better knowledge of such behavior may affect the design window boundaries. Accordingly, a systematic analysis of the effect of varying key parameters and physical assumptions has been made.

A. Pulse Length and Fatigue Constraint

The most severe limitation on solid divertor target options at high heat loads appears to be the dual constraint of sputtering and cyclic fatigue. Extension of the reactor pulse length would be a means of easing the fatigue problem. An examination of the improvement in material lifetimes expected from an order of magnitude reduction in the number of thermal stress cycles imposed on the target per year was performed. Allowable strain ranges for fatigue lives between 10^3 and 10^4 cycles from Ref. 42, combined

with the equation, $t \leq \frac{2\ k\ (1-\nu)\ \Delta\epsilon_{max}}{\alpha\ q''}$, established the appropriate fatigue life vs. thickness curves for various heat fluxes.

Sputtering rates at each heat flux were determined as in section III-A. At each heat flux the thickness and corresponding lifetime at which the minimum thickness to withstand sputtering just equaled the maximum thickness to withstand fatigue was the optimum material design. For niobium, these points appear on Figure VI-1 along with the base case optimum life curve. For a given heat flux, an order of magnitude reduction in cycles per year provides only 80% increase in the target lifetime. Improvements in other materials were of the same order.

B. Sputtering Characteristics

The devastating rate at which target material appears to be eroded by sputtering in this analysis demands a search for ways in which the situation may be improved. Several factors may be considered. First, there is some scatter in the reported data for sputtering coefficients. A comparison of data from Ref. 33 with corresponding predictions of the analytical formula of Ref. 51, Figure VI-2, indicates a factor of two uncertainty in these coefficents. Second, the imposed plasma load may be made less severe than is currently predicted by the INTOR study. Since light ion sputtering coefficients peak near energies of 1 keV, reducing or raising the ion energies would reduce their

sputtering coefficient, thereby reducing the erosion rate. At the same incident heat flux, fewer particles of higher energy or more particles of lower energy could reduce the sputtering rate by up to 50%. Taking as an optimistic improvement a four-fold reduction in the sputtering rate, the more favorable optimum life curve of Figure VI-3 results. Lifetimes for each heat flux are seen to increase approximately 2.5 times.

Such optimism may be warranted in light of suggestions that radiation in the plasma might be enhanced, resulting in less energetic particles at the divertor target. (Ref.13) However, the degree to which relatively high Z materials may be ionized and accelerated into the divertor target will adversely affect the sputter rate. Indeed, ions of $Z > 6$ can achieve sputtering coefficients greater than one if accelerated to 1 keV, possibly causing a catastrophic sputtering cascade. Finally, the divertor target may occasionally receive the intense particle load of a plasma disruption. The conditions in the divertor chamber affecting self-sputtering and plasma disruption effects are ill-defined, and have not been included in this analysis.

C. CHF Limit

Due to present uncertainties in the prediction of subcooled boiling pressure drop, the critical heat flux limit for the design window has been restricted such that the predicted critical heat flux is 1.3 times larger than the design heat flux. (See section II-B.) Should experience

with subcooled liquids in high heat fluxes provide confidence that this safety factor may be reduced, an appreciable enlargement of the design window operating region will result. Figure VI-4 indicates the effect of varying the safety factor from 1.1 to 1.5. A wider selection of operating conditions becomes available as safety factor is lowered. Specifically, reducing the safety factor from 1.3 to 1.1 while maintaining other base conditions reduces the required mass flux by 30%.

The prospect of operating a high mass flux system under conditions of subcooled boiling on the tube walls introduces the potentially catastrophic occurrence of pressure drop-flow rate instabilities. Should the flow rate decrease momentarily due to any perturbation, the increased boiling would increase pressure drop, in turn lowering T_{sat} and possibly driving the tube to a burnout condition. Lowdermilk, et al, among others dealt extensively with this phenomenon in their small tube, high heat flux experiments. (Ref. 20) Throttling the inlet to each heated tube would help control such instabilities, but would incur a significant pumping power penalty.

D. Pumping Power Limit

Relaxation of the pumping power ratio limit from 2% to 5% or 10% may prove necessary and justifiable, particularly in cases where heat fluxes greater than 1 kw/cm^2 may be received. The analysis here does not account for pressure losses in headers, bends, throttles, etc., so pushing the pumping power limit above 20% would seriously impact on energy economy.

Such a limit relaxation would clearly widen the operating region of the design window, allowing a greater margin of safety against CHF, as shown by Curves A and B in Figure VI-9.

E. Inlet Temperature

Increasing the inlet temperature decreases the exit subcooling. This necessitates higher mass flux to avoid CHF. The accompanying increase in pumping power pushes the CHF constraint ever closer to the $W_p = .02$ constraint. With other parameters unchanged from the base case, the design window vanishes for T_{in} larger than 190°. Operation at an inlet temperature as close to freezing as possible widens the design window and allows operation at the lowest possible mass flux, as evidenced by Figure VI-5.

F. Pressure

Varying pressure changes the degree of subcooling for a fixed inlet temperature. High pressures provide an increase in subcooling, allowing lower mass flux to avoid CHF. This enlarges the hydraulic design window, as shown in Figure VI-6, but adds to the hoop stress imposed on the material. The radius limit due to hoop stress imposed on the structure is proportionately reduced. Further, the occurrence of system pressure cycling would impose an additional life-shortening fatigue component to the structural analysis. Finally, a preference for low to moderate pressure systems is indicated by the consequences of a high pressure pipe break within the divertor chamber.

G. Tube Length

Variation of the tube length, keeping other parameters constant, was investigated. The resulting operating regions are illustrated by Figure VI-7 for lengths of 10cm, 50cm, and 100cm. Because the temperature rise in the tube is greater for longer lengths, less exit subcooling remains. A higher mass flux is necessary to avoid CHF. Entrance effects become less significant at longer lengths, improving the pumping power ratio over the base case. The net effect is that the permissible operating region shrinks as length is increased.

H. Thickness

Due to the wall thickness demands of sputtering and fatigue, adjacent tube arrays will be required to operate with considerable wall thickness separating the coolant channels. As this thickness increases, the linear power received by each channel also increases; $q'_{tot} = 2\left(\frac{t+r}{r}\right) q''_{act}$. However, the conduction path to the rear side of the channel is improved, permitting extraction of more heat by the coolant at essentially the same peak heat flux on the hottest side. The pumping power ratio is thus improved, resulting in an enlargement of the design window for wall thicknesses between .05(r) and 3.0(r). For wall thicknesses above 3.0(r), heat flux to the coolant exceeds the incident heat flux from the plasma, q''_{act}, raising mass flux and shrinking the design window. An optimum thickness may be determined for each structural material at which the design window is at its "widest". See Figure VI-8.

I. Heat Flux

An investigation of the limits to which steady state heat flux may be raised was undertaken, keeping all other parameters as in the base case. Extrapolating the CHF correlation based on Lowdermilk's work to higher heat fluxes imposes a very stringent constraint on the design window. As shown in Figure VI-9, the increased mass flux required to accomodate a 4 kw/cm^2 heat flux raises the minimum pumping power ratio to avoid CHF to approximately 60%. At these higher heat fluxes, the correlation on Rousar (Ref. 19) is more appropriate for CHF, and leads to the operating regions depicted in Figure VI-10. Clearly, a significant pumping power penalty is incurred by raising heat flux. The work of M.A. Hoffman, et al., (Ref. 12), provides an estimate of the option space available at a 3.3 kw/cm^2 heat flux, and is in close agreement with Figure VI-10.

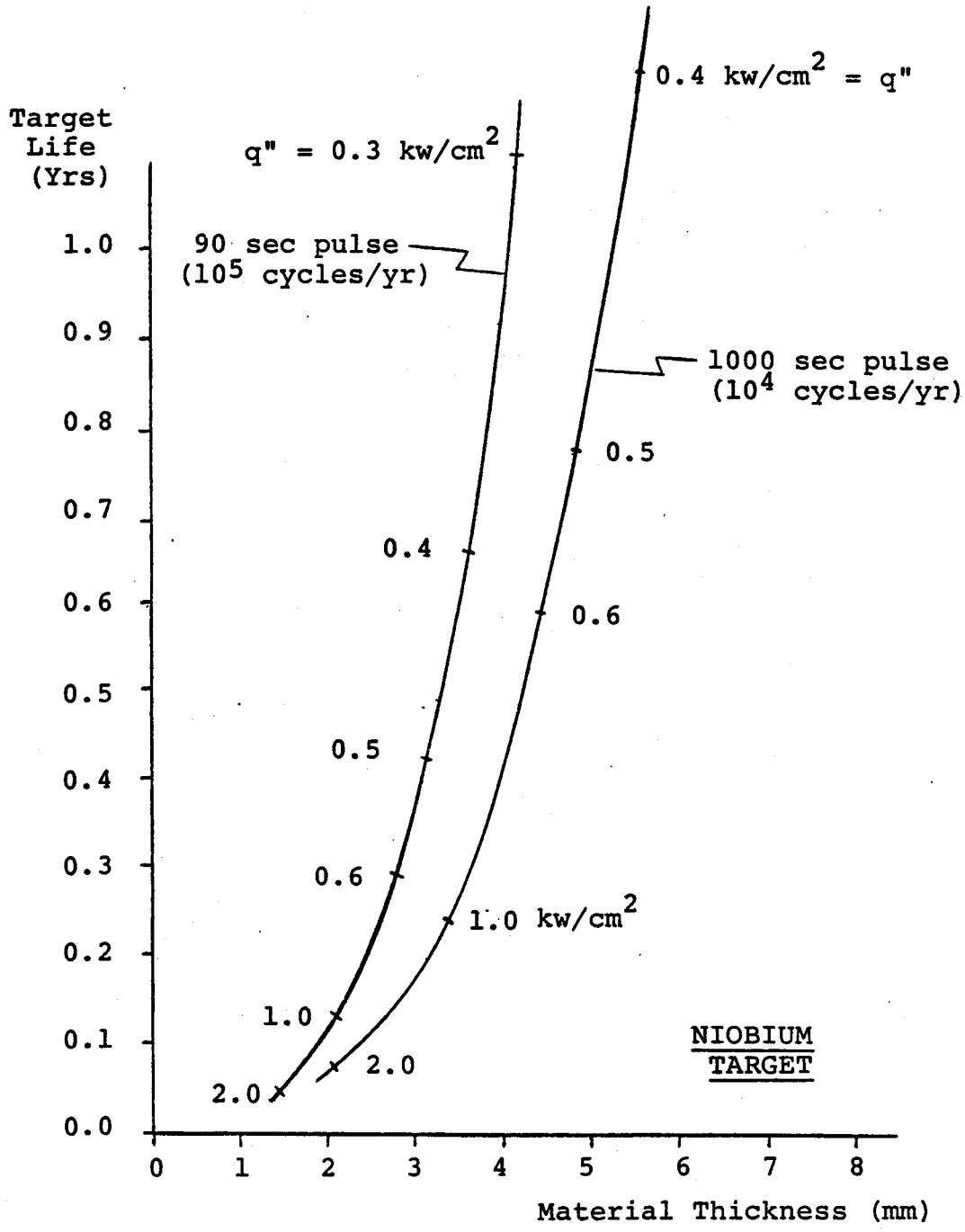

Figure VI-1: Sensitivity to Change in Pulse Duration of Optimum Life vs. Thickness Curves for Niobium Target.

Z	Target Material	Data S_i for 1 keV D^+ from ORNL data (Ref. 33)	Theory S_i for 1 keV D^+ from Bohdansky equation (Ref. 51) °°
4	Be	.034*	.028
6	C_{gr}	.018	.027
13	Al	.04 *	.023
22	Ti	.010	.017
23	V	.013*	.016
29	Cu	.095	.014
41	Nb	.0043	.0098
42	Mo	.0062	.0100

°° Heats of sublimation taken from Touloukian, Ref. 50

* Extrapolated.

Figure VI-2: Comparison of Experimental Data with Analytical Results for Sputtering Coefficient.

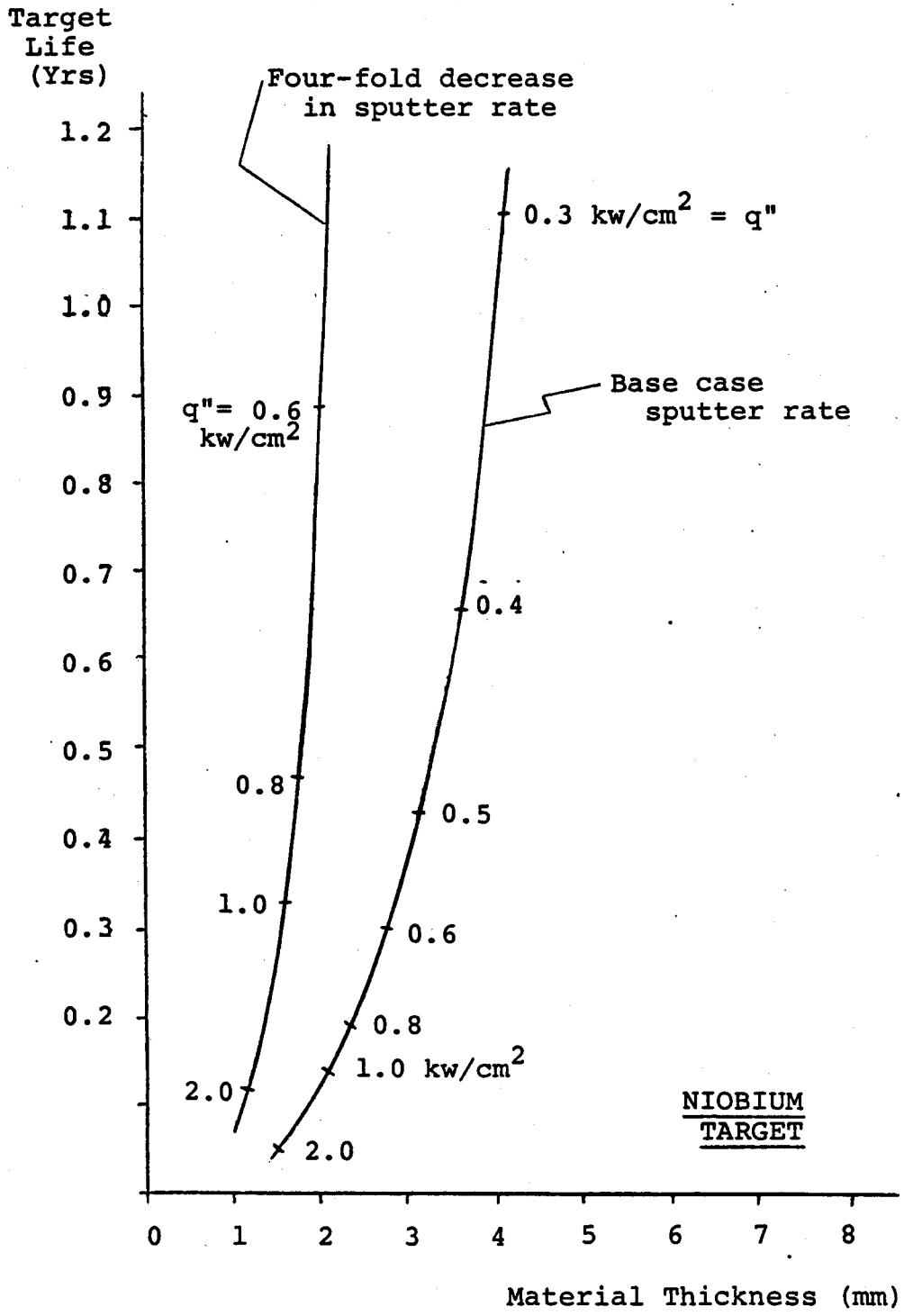

Figure VI-3: Sensitivity to Four-fold Decrease in Sputter Rate of Optimum Life vs. Thickness Curves for Niobium Target.

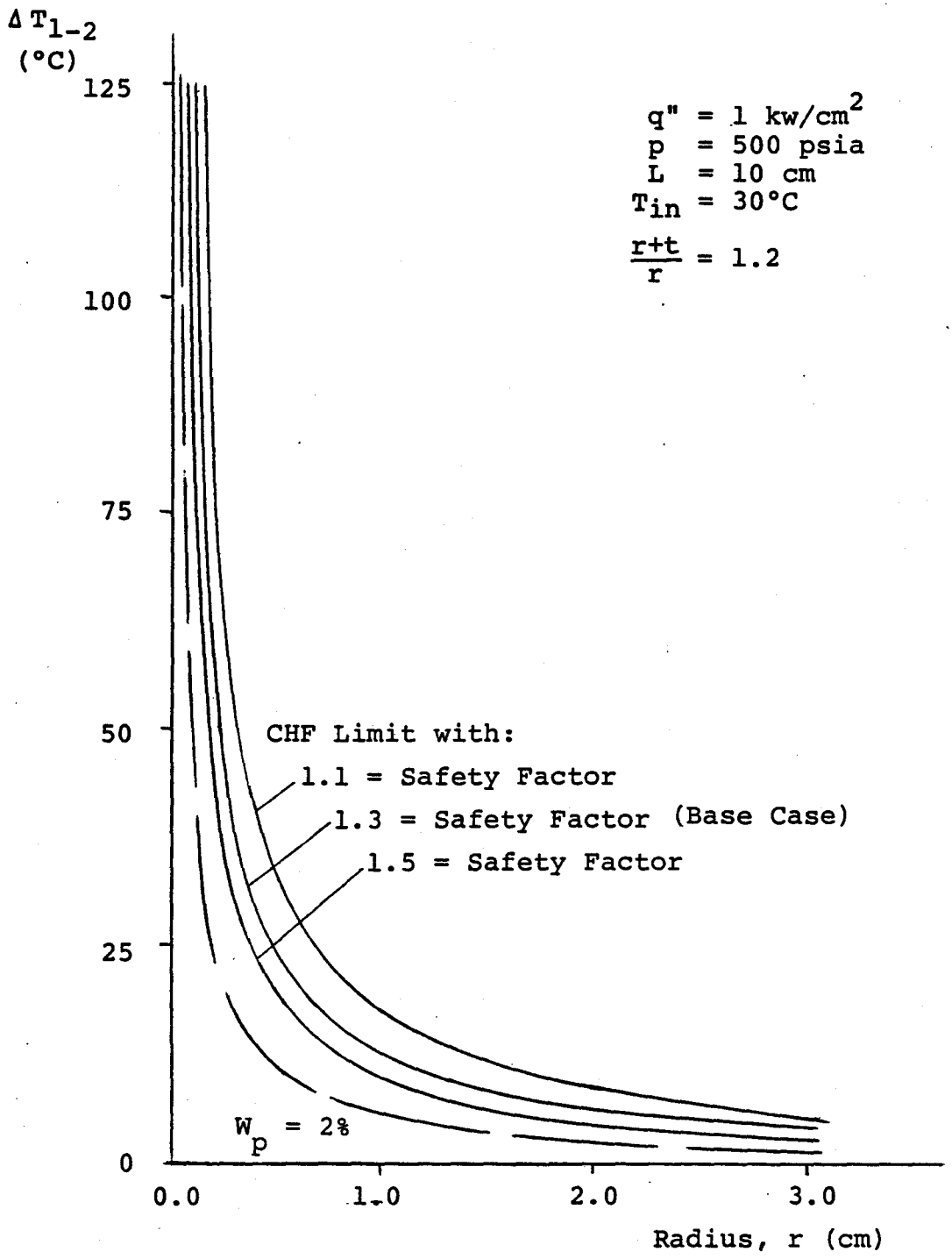

Figure VI-4: Effect of Varying CHF Safety Factor on Design Window

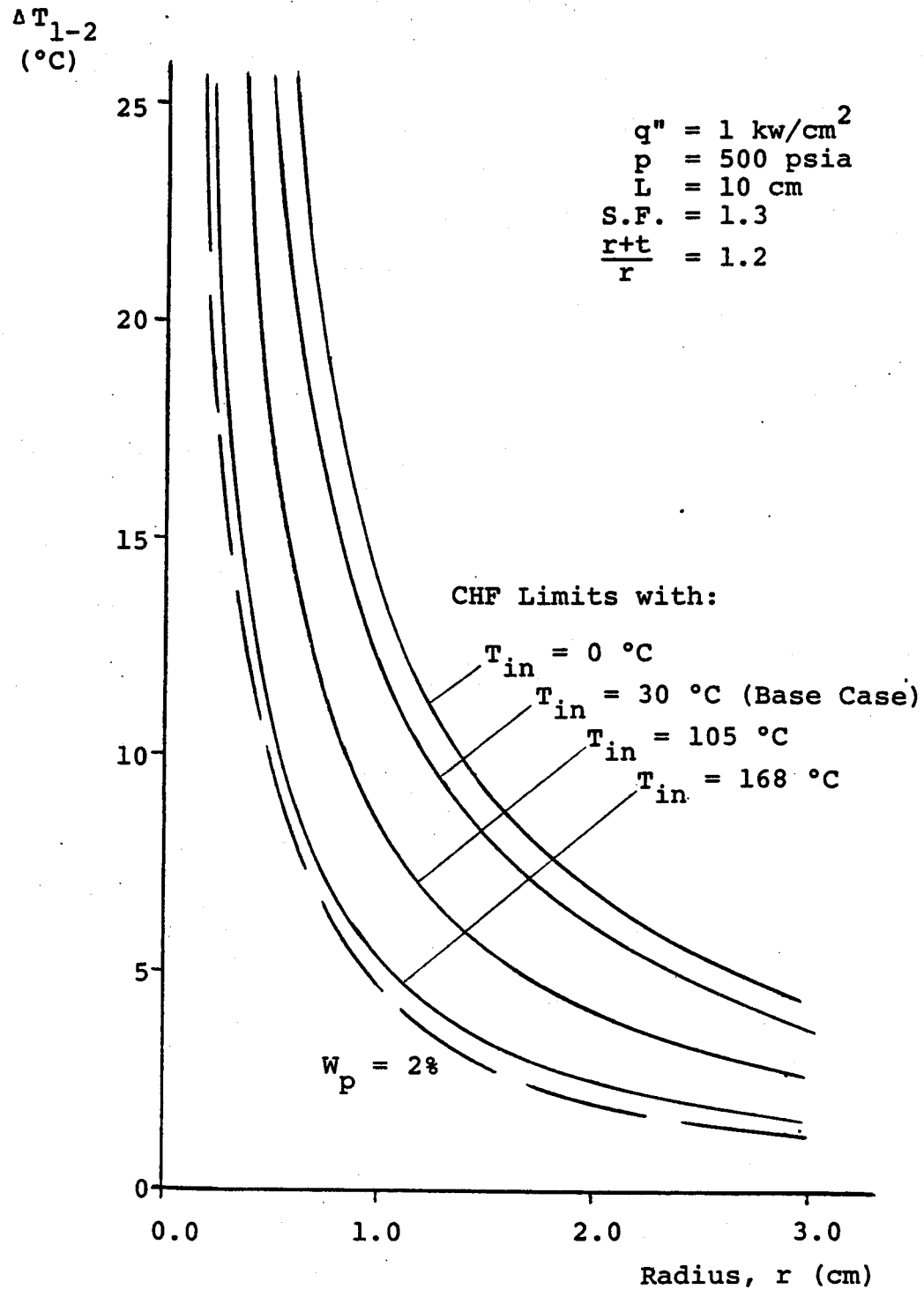

Figure VI-5: Effect of Varying Inlet Temperature on Design Window

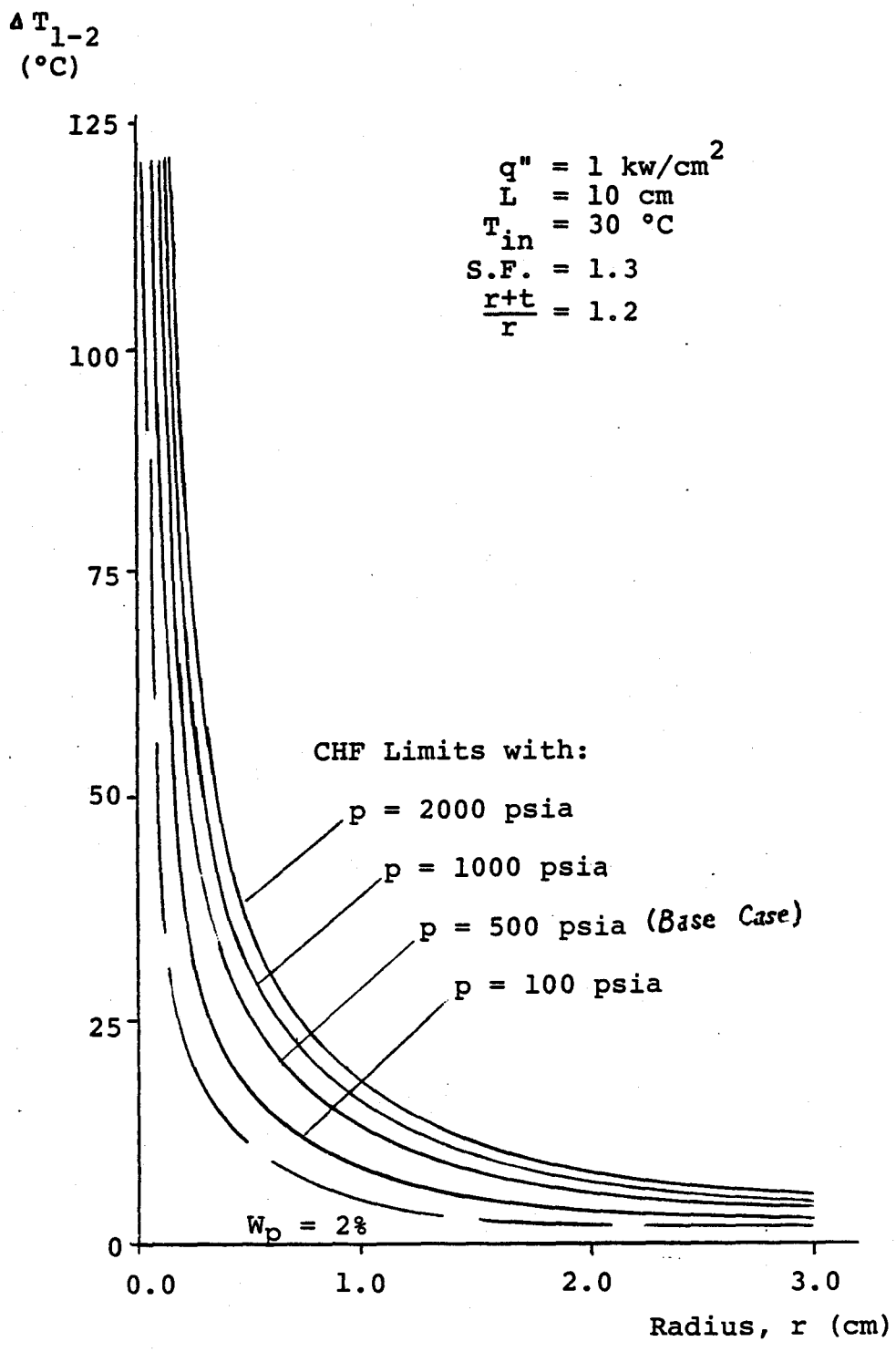

Figure VI-6: Effect of Varying Pressure on Design Window

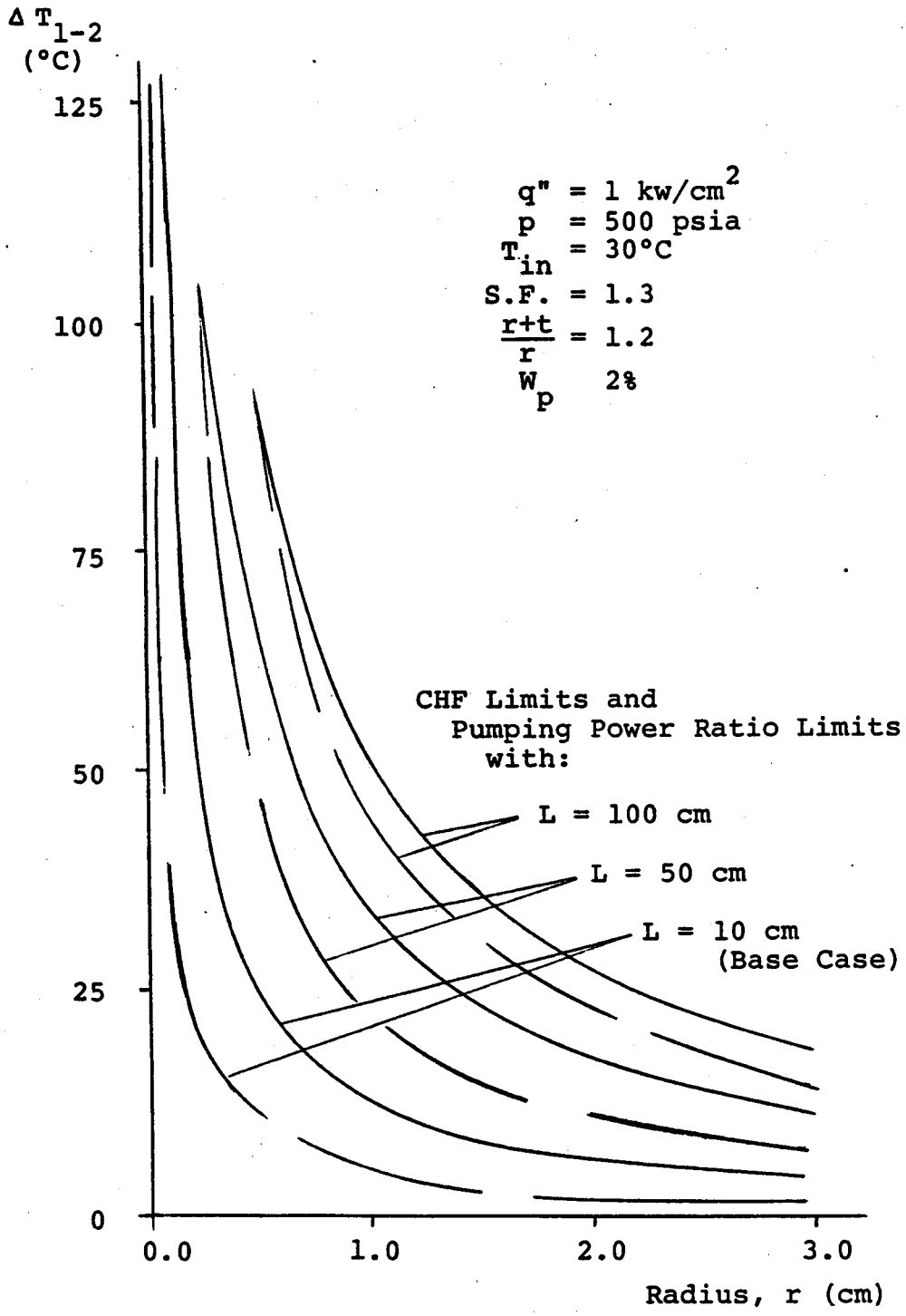

Figure VI-7: Effect of Varying Length on Design Window

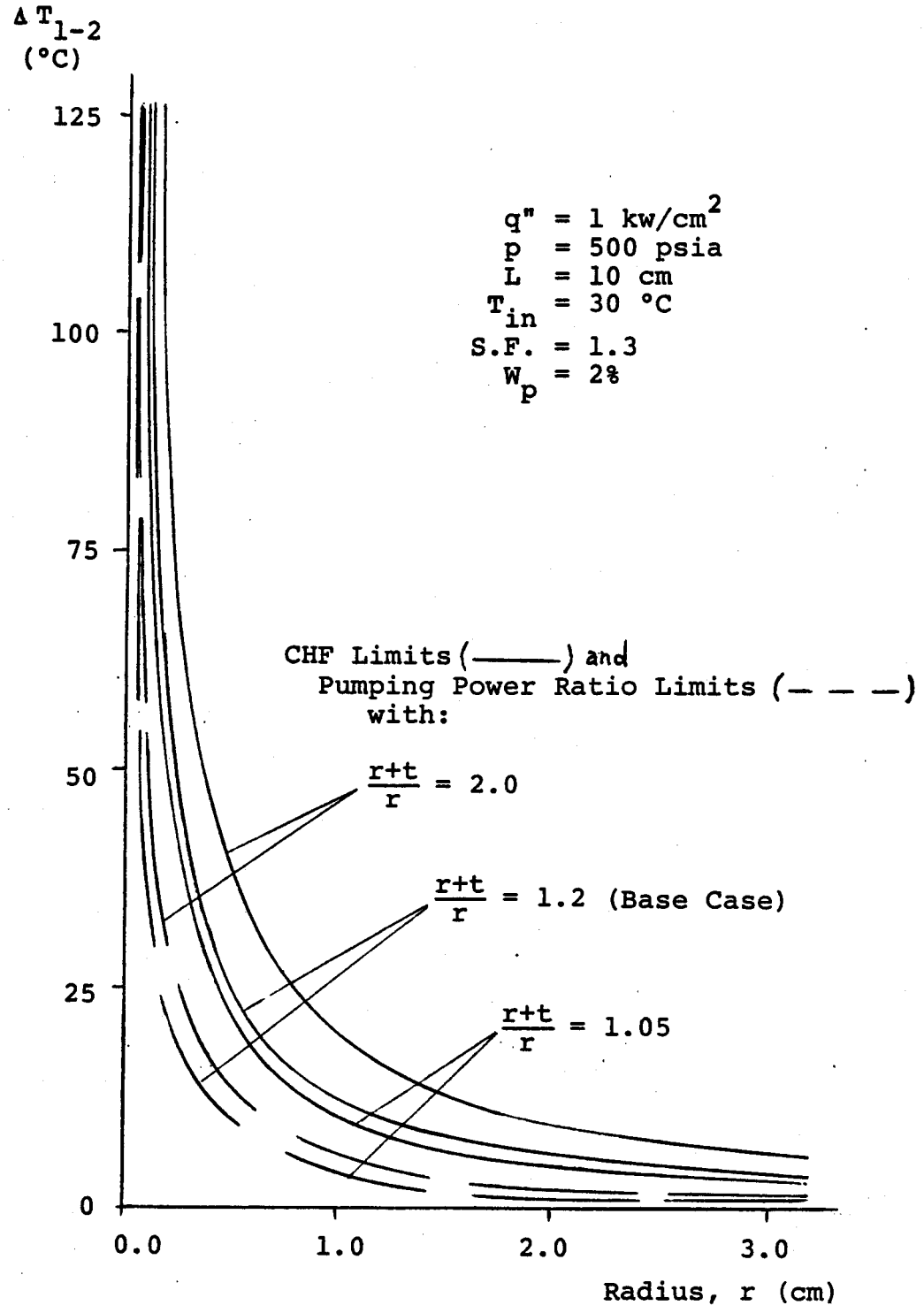

Figure VI-8: Effect of Varying Wall Thickness between Coolant Channels

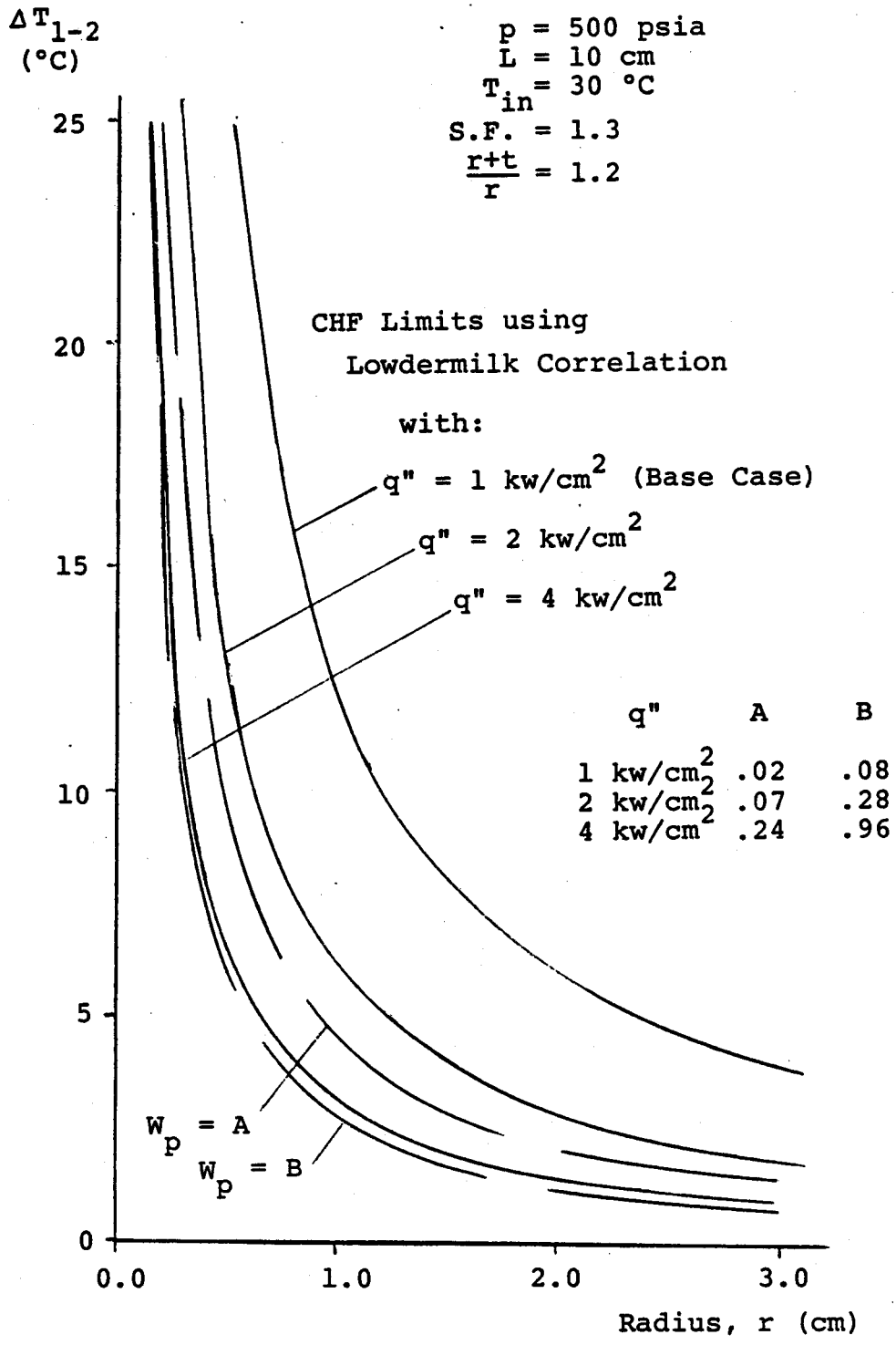

Figure VI-9: Effect of Raising Heat Flux on Design Window (Using Lowdermilk Correlation)

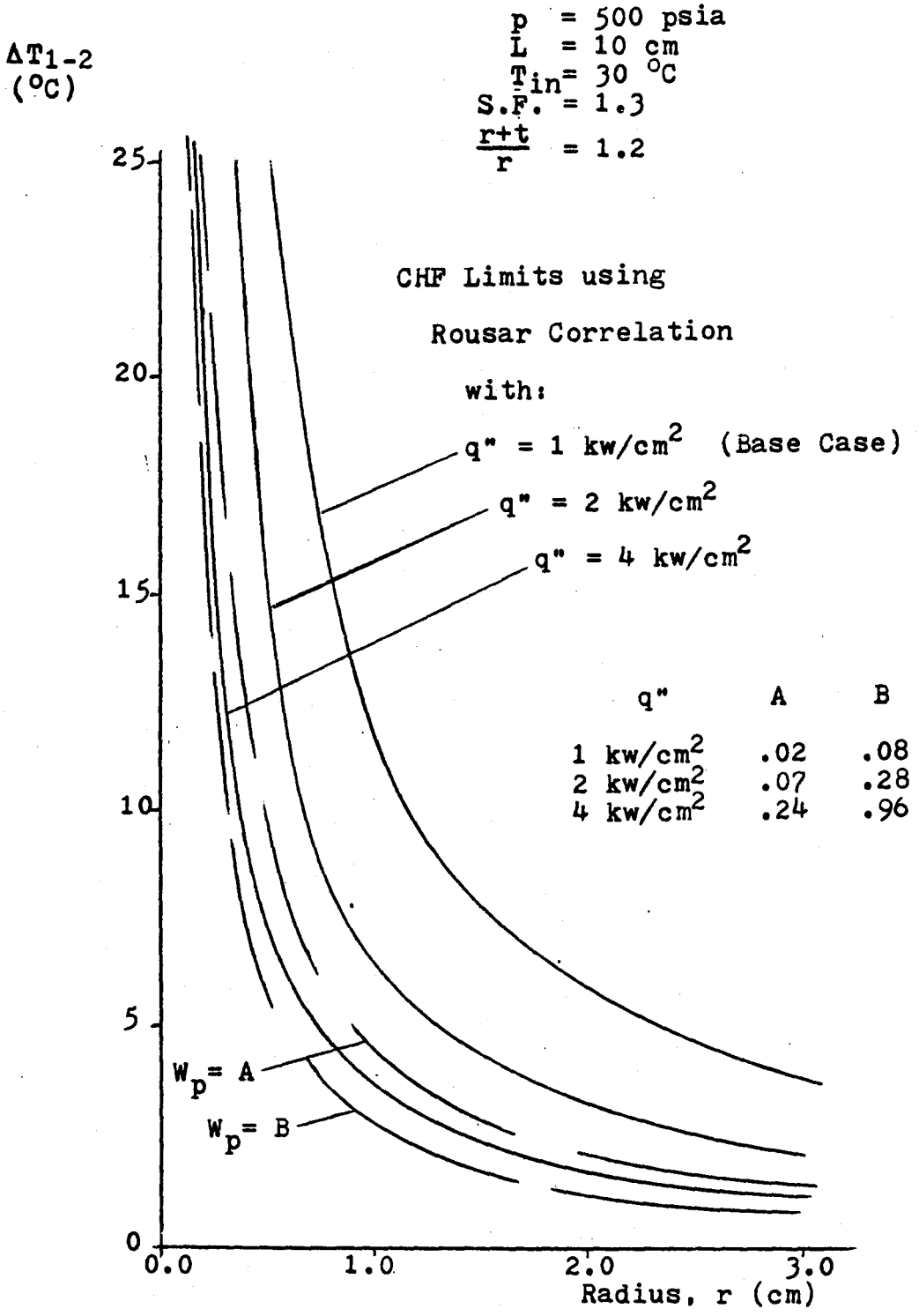

Figure VI-10: Effect of Raising Heat Flux on Design Window (Using Rousar Correlation)

VII. CONCLUSIONS

The conclusions of this investigation of solid divertor target options can be summarized as follows.

1. A hydraulic system using non-boiling highly subcooled water appears feasible to cool surface heat loads of 1 kw/cm^2 in the divertor target application. Intermediate pressures (200 to 500 psia) are required to provide adequate subcooling to avoid nucleate boiling. Channel lengths from 10 cm to 100 cm may be used.

2. Provision for handling hot spots and off-normal conditions with heat loads up to 2 kw/cm^2 may be made by operating the system with very high mass flux and high inlet subcooling. The pumping power to heat transfer ratio can be kept at 2%. Careful design will be necessary to avoid internal cavitation erosion.

3. The Saha-Zuber equation for "net vapor generation" compares favorably with existing CHF correlations in the range of variables pertinent to divertor applications. It provides a theoretical basis for predicting CHF and should prove valuable in extending CHF prediction beyond the ranges of existing data.

4. At high mass flux, the onset of fully developed nucleate boiling will increase the total pressure drop over the non-boiling case two to six times. This can be accomodated in channels of diameter greater than 4 mm and at

pressures of 500 psia with less than a 10% overall pressure drop. The likelihood of a pressure drop-flow rate instability in a bank of flow channels, however, remains an obstacle to operation in this regime.

5. The cyclic thermal loading and ion sputtering conditions currently envisioned at the divertor target surface limit the life of conventional tube or plate targets, for the eight candidate materials studied, to several months. Molybdenum Alloy (TZM), and Niobium Alloy (D-43) appear most promising from a materials standpoint, but may well quench the plasma unless ions sputtered from the target are effectively prevented from penetrating the plasma core. Beryllium appears most favorable among the low Z candidates, but can survive only one month without redeposition.

6. Development of a mechanically unbonded, thermally bonded laminated design would allow target life to be extended to 9 months.

7. A copper substrate protected from sputtering could be designed to survive the cyclic loading for well over one year.

8. Techniques for rapid remote replacement of the divertor target, in-situ recoating of the surface, reduction of the particle load, or steady state tokamak plasma operation appear essential to development of a solid divertor target capable of surviving for one year without plant shutdown.

VIII. RECOMMENDATIONS

The investigation of divertor target design and cooling herein described has revealed numerous areas in which further effort is necessary. The limits on lifetime and heat load predicted by this general approach impose severe restrictions on plant capacity factor, since with conventional tube or flat plate arrangements frequent plant shutdowns may be necessary to allow refurbishment. Methods of in-situ coating of the divertor target during rejuvenation periods, if developed, might greatly ease design by alleviating the wall thickness constraint due to sputtering. Without such a technique, the development of a laminated, thermally bonded, mechanically unbonded, actively cooled flat plate target should be emphasized as a promising solid target option. Targets mounted on central supports, with edges free to bend and expand, should be examined as a possible means of reducing thermal fatigue.

Areas of investigation necessary for improved evaluation of all solid target options include the following:

1. Validity of Saha-Zuber prediction of "net vapor generation" as an accurate forecast of CHF conditions over a broad range of variables.

2. Effect of non-uniform temperature distribution in coolant on fluid viscosity and overall pressure drop.

3. Understanding and correlation of subcooled boiling

pressure drop in coolant channels.

4. Thermal stresses at tube connections and plate edges.

5. Material properties at elevated temperatures, particularly modulus of elasticity.

6. Low-cycle fatigue life data verification for candidate materials at elevated temperatures.

7. Occurrence and behavior of redeposition after sputtering.

8. Aggregate effects of simultaneous sputtering and cyclic fatigue under surface heat loads. (Does sputtering promote or retard fatigue damage?)

9. Chemical erosion of graphite exposed to hydrogen plasma.

10. Transport of sputtered particles from target to plasma core.

11. Distribution of particle fluxes and energies across the target surface.

12. Techniques for helium, hydrogen, and impurity separation.

Areas of investigation specific to the suggested laminated target design are listed below:

13. Effect of released lithium on plasma burn.

14. Control of tritium generated in lithium layers.

15. Positive closure valves for lithium expansion ducts.

16. Mechanical behavior at constraining edges.

REFERENCES

1. Sanderson, A.D., and P.E. Scott, "Bundle Divertor for a Fusion Reactor", CLM-P 530, Culham Laboratory, Abingdon, England, 1978.

2. McDonnell-Douglas Aeronautics Corporation, "Developing Maintainability for Tokamak Fusion Power Systems-Phase II Report", US DOE Contract # EG-77-C-02-4184.A001, Nov 1978.

3. Lipov, M.Y., and E.V. Muraviev, "Design of High Efficiency Divertor Systems for Tokamak Power Reactors", Kurchatov Inst. of Atomic Energy, Translated from Russian, Beta Associates, Moscow 1979.

4. Luzzi, T., "Poloidal Divertor Target for SLPX", Grumman Research Report RE-606J, Bethpage, NY 1980.

5. Nygren, R.E.,"Plasma-Materials Concerns in ETF", Proceedings of the Workshop on Plasma Materials, Albuquerque, June 1980.

6. U.S. DOE, "U.S. Contribution to the International Tokamak Reactor Workshop, Phase 1", USA INTOR/80-1, June, 1980.

7. Gambill, W.R., et al., "Heat Transfer, Burnout, and Pressure Drop for Water in Swirl Flow through Tubes with Internal Twisted Tapes", ORNL 2911, 1960.

8. Yang, T.F., et al., "Reactor Application of an Improved Bundle Divertor", WFPS-TME-104, Westinghouse, Nov 78.

9. Winovich, Warren, and William C.A. Carlson,"The Giant Planet Facility", Ames Research Center, NASA, Moffett Field, California, 1979.

10. McDonnell-Douglas Aeronautics Corporation,"High Impact Pressure (HIP) Facility", Engineering and Research Technical Facility Description, St. Louis, Mo. 1979.

11. Harbaugh, Willis E., "Water Cooled D.C. Heat Sink Development", PO# 2660502, RCA Corp., Lancaster, PA, Sep 1977.

12. Hoffman, M.A., et al., "Fusion Reactor First Wall Cooling for Very High Energy Fluxes", Nuclear Engineering and Design, v. 36, 1976, pp.37-46.

13. Argonne National Lab, "STARFIRE-A Comprehensive Tokamak Fusion Power Plant Study", ANL/FPP/ 80-1, Sep 1980.

14. Hoffman, M.A., et al., "Review of Heat Transfer Problems Associated with Magnetically Confined Fusion Reactor Concepts", AIChE Symposium Series, No. 168, v 73, p.9, 1977.

15. Chao, Jiatsong,"Thermal-Hydraulic and Neutronic Considerations for Designing a Lithium Cooled Tokamak Blanket", PhD Thesis, Nuc. Engr. Dept., MIT, Dec 1978.

16. Rohsenow, Warren M., and Harry Choi, Heat, Mass, and Momentum Transfer, Prentice-Hall, Englewood Cliffs, NJ, 1961.

17. Bergles, A.E., et al., Two Phase Flow and Heat Transfer in the Power and Process Industries, Hemisphere Publishing Corp., Washington, 1981.

18. Tong, L.S., Boiling Heat Transfer and Two Phase Flow, John Wiley and Sons, New York, 1965.

19. Rousar, D.C., "Correlation of Burnout Heat Flux for Fluids at High Velocity and High Subcooling Conditions", MS Thesis, Dept of Mech Engr, U. C. - Davis, 1966.

20. Lowdermilk, Warren H.,et al.,"Investigation of Boiling Burnout and Flow Stability for Water Flowing in Tubes", NACA-TN 4382, Sep 1958.

21. Gambill, W.R., and N.D. Greene, " Boiling Burnout with Water in Vortex Flow", Chemical Engineering Progress, v.54, No. 10, p.68, Oct 1958.

22. Schaefer, John W., and John R. Jack, "Investigation of Forced Convection Nucleate Boiling of Water for Nozzle Cooling at Very High Heat Fluxes", NASA Tech. Note D-1214, May 1962.

23. Gierszewski,P.,et al.,"Property Correlations for Lithium, Sodium, Helium, Flibe, and Water in Fusion Reactor Applications", MIT, PFC-RR-80-12, Aug 1980.

24. Owens,W.L., and V.E. Schrock, "Local Pressure Gradients for Subcooled Boiling of Water in Vertical Tubes", ASME Paper 60-WA-249, 1960.

25. Tarasova, N.V.,et al.,"Pressure Drop of Boiling Subcooled Water and Steam Water Mixture Flow in Heated Channels", Proceedings, 3rd International Heat Transfer Conference, ASME, NY, pp. 178-183.

26. Mendler, O.J., et al.,"Natural Circulation Tests with Water at 800 to 2000 psia Under Nonboiling, Local Boiling, and Bulk Boiling Conditions", Trans. ASME, Journal of Heat Transfer, v.83, pp261-73, Aug 1961.

27. Martinelli, R.C., and D.B.Nelson, "Prediction of Pressure Drop during Forced Circulation Boiling of Water", Trans. ASME, v70, pp695-702, 1948.

28. Dormer, Thomas,Jr., and Arthur E. Bergles, "Pressure Drop with Surface Boiling in Small Diameter Tubes", MIT Dept of Mech Engineering Report No. 8767-31, Sep 1964.

29. Fraas, A.P.,"Comparative Study of the More Promising Combinations of Blanket Materials, Power Conversion Systems, and Tritium Recovery Systems", ORNL-TM 4999, Nov 1975.

30. Lopina, Robert, and A.E. Bergles, "Heat Transfer and Pressure Drop in Tape Generated Swirl Flow", Tech. Rpt.# 70281-47, MIT Department of Mechanical Engineering, June 1967.

31. Collier, J.G., Convective Boiling and Condensation, McGraw-Hill, London, 1972.

32. Kim, J., et al.," A Heat Transfer Study of Water Cooled Swirl Tubes for Neutral Beam Targets", 7th Symposium on Engineering Problems of Fusion Research, Knoxville, TN, Oct 1977.

33. Barrett,C.F.,et al.,"Atomic Data for Controlled Fusion Research", ORNL 5207, 1977.

34. Thomas, E.W.,et al.,"Atomic Data for Controlled Fusion Research, Revisions and Additions", ORNL 5207/R1, 1979.

35. Kummer, Donald L., "Conference Proceedings; Low Activation Materials Assessment for Fusion Reactors", EPRI-ER-328-SR, San Fransisco, CA, Feb 1976.

36. LaQue, F.L., and H.R. Cooper, Corrosion Resistance of Metals and Alloys, 2nd ed, Reinhold Publishing Corp., New York, 1963.

37. Knapp, Robert T.,et al.,Cavitation, McGraw-Hill, New York, 1970.

38. Rabinowicz, Ernest C., MIT Mechanical Engineering Department, Surface Effects Lab, Private Communication, 23 April 1981.

39. Harvey, John F., Pressure Component Construction, Van Nostrand Reinhold Company, New York, 1980.

40. Boley, B.A., and J.H. Weiner, Theory of Thermal Stresses, Wiley and Sons, Inc., New York, 1960.

41. Arpaci, Vedat S., Conduction Heat Transfer, Addison-Wesley Publishing Company, Reading, MA, 1966.

42. Yu, Ge Ping, "Properties (Unirradiated) for Mechanical Design for Candidate First Wall Alloys", Interim Fusion Materials Report, MIT Nuclear Engineering Department, February 1980.

43. Armbruster, Michael, "Effect of Some Types of Machining Processes on Beryllium Fatigue Strength Properties", 4th Int. Conf. on Beryllium, Royal Society, London, Oct 77.

44. Blackman, L.C.F., Modern Aspects of Graphite Technology, Academic Press, New York, 1970.

45. Schultz, Joel, "Preliminary Comments on Limiter-Limiter Pump Material Selection and Tabulated Figures of Merit", MIT-ETF Design Center, Sep 1980.

46. Schivell, J.F., and D.J. Grove, "Thermal Stress Problems in Tokamak Surfaces", Journal of Nuclear Materials, v.53, 1974, pp.107-110.

47. Norem, J. and D.A. Bowers, "Thin Low Z Coatings for Plasma Devices", ANL/FPP/TM-108, May 1978.

48. Ambartsumyan, S.A., Theory of Anisotropic Plates, Technomic Publiching Company, Stamford, CT, 1970.

49. American Society for Metals, Metals Handbook, 9th ed., v.2, "Properties and Selection - Non-ferrous Alloys and Pure Metals", Metals Park, OH, 1979.

50. Touloukian, Y.S., et al., Thermophysical Properties of Matter, v 1, Thermal Conductivity, Metallic Elements and Alloys, IFI Plenum, New York, 1970.

51. Bohdansky, J., et al., "An Analytical Formula and Important Parameters for Low Energy Ion Sputtering", Journal of Applied Physics, v 51, (5), May 1980.

52. Vosen, S.R., et al. "Mechanical Design Criteria for Continuously Operating Neutral Beams", Sixth Int'l. Conference on Fusion Technology paper, Lawrence Livermore Labs,

53. Yang, T.F., MIT Plasma Fusion Center, Private Communication, 28 Oct 1980.

54. Saha, P., and Zuber, N., "Point of Net Vapour Generation and Vapor Void Fraction in Subcooled Boiling", Fifth International Heat Transfer Conference, Tokyo, Paper B4.7, 1974.

55. McCracken, G.M., and P.E. Stott, "Plasma Surface Interactions in Tokamaks", Nuclear Fusion, v 19, (7), 1979, pp 889-981.

56. Kays, W.M., Convective Heat and Mass Transfer, McGraw-Hill, San Francisco, 1966, p 174.

57. El-Wakil, M.M., Nuclear Heat Transport, American Nuclear Society, Lagrange Park, Ill., 1978.

APPENDIX A: MATERIALS PROPERTIES

Table A-1 provides representative property values for the eight candidate materials in the range of operating temperatures indicated. Physical properties are evaluated at the midpoint of the temperature range for each material, except that strain and stress limits are taken so as to give a conservative bound over the entire operating temperature range. The improvement in material lifetime available from abandoning this conservatism is less than a factor of two.

Materials data is taken from References 36, 42, 43, 44, 49, and 50. Pertinent data for water and lithium is taken from References 23 and 57.

The development of the fatigue life versus thickness curves appearing in Figures V-2 and V-3 utilizes equation 26 and the maximum strain range data for fatigue life.

$$t \leq \frac{2\,k\,(1-\nu)}{\alpha\,q''}\,\Delta\epsilon_{max} \qquad (26)$$

As an example, substituting in property values for Nb and $q''=1$ kw/cm^2 yields $t \leq \frac{2(53)(.62)}{7.6\,(10)}\,\Delta\epsilon_{max} = .865\,\Delta\epsilon_{max}$. The following data points result.

Life	$\Delta\epsilon_{max}$(Nb)	t_{max}(mm)
10^4 cycles	.278	2.4
2×10^4 cycles	.210	1.9
4×10^4 cycles	.180	1.5
10^5 cycles	.160	1.4

Plotting these points on the life vs. thickness axes yields the fatigue curve for 1 kw/cm^2 of Figure V-3. Changing q" in the equation above provides the curve for different heat fluxes.

	Be	C_{gr}	Al	Ti	V	Cu	Nb	Mo
Operating Temp. Range (^oC)	200-800	400-2000	200-400	300-400	200-800	300-600	200-800	200-1000
Water Corrosion Temp. Limit (^oC)	300			360	360		330	360
Melt Temperature (^oC)	1290	3367	631	1668	1900	1085	2468	2610
k ($w/m-^oK$)	190	100	180	15	28	313	53	100
E (GPa)	290	10	48	75	109	108	63	249
α ($x10^{-6}/^oK$)	15.0	10.0	25.0	10.2	10.2	18.0	7.6	6.3
Poisson's Ratio, ν	.05	.10	.35	.30	.36	.36	.38	.32
Density, ρ (g/cm^3)	1.85	2.10	2.70	4.54	6.11	8.96	8.57	10.2
Atomic Weight, M	9.01	12.0	27.0	47.9	50.9	63.5	92.9	95.9
Allowable Stress Intensity (MPa)	93	20	52	203	109	39	68	207
Max Strain Range (%) for Fatigue Life:	*			*	*			
10^4 cycles	.116	.083	.063	.240	.614	.343	.278	.070
$2x10^4$ cycles			.073	.226		.290	.210	
$4x10^4$ cycles			.080	.220		.240	.180	
$5x10^4$ cycles					.421			
10^5 cycles	.091 *	.061	.089	.215 *	.376 *	.200	.160	.046

* indicates room temperature fatigue data; high temperature data not available.

Sputtering coefficients provided in Table III-1.

Table A-1: Representative Materials Properties

Property	=	=	
Heat Flux, q"	10 Mw/m^2	1 kw/cm^2	$3.17 \times 10^6 \frac{BTU}{hr\text{-}ft^2}$
Mass Flux, G	$10^4 \frac{kg}{sec\text{-}m^2}$	$10^3 \frac{g}{sec\text{-}cm^2}$	$7.37 \times 10^6 \frac{lbm}{hr\text{-}ft^2}$
Mass Flow Rate, $\dot{m}$	1 kg/sec	10^3 kg/sec	7920 lbm/hr
Volume Flow Rate	$472 \frac{cm^3}{sec}$	7.48 GPM	1 ft^3/min
Pressure, p	.1 MPa	750 torr	14.5 psia
Length, L	1 m	100 cm	3.281 ft
Mass, m	1 kg	1000 g	2.2046 lbm
Power, P	1 Mw	1000 kw	$3.41 \times 10^6 \frac{BTU}{hr}$
Density, ρ	1 g/cm^3	1000 kg/m^3	62.4 lbm/ft^3
Thermal Conductivity, k	$100 \frac{w}{m\text{-}^oC}$	$.239 \frac{cal}{sec\text{-}cm\text{-}^oC}$	$57.8 \frac{BTU}{hr\text{-}ft\text{-}^oF}$
Specific Heat, c_p	1 cal/g-^{o}C		1 BTU/lbm-^{o}F
Viscosity, μ	10 poise	1 kg/sec-m	2419 lbm/hr-ft

Table A-2: Conversion Equivalents

APPENDIX B: METHODOLOGY SUMMARY

This appendix summarizes the design window methodology used in this investigation. The primary analysis is done for parallel tube arrays exposed to particle and heat loads on one side only. The procedure is then modified to treat protective tiles and flat plates with internal channels.

The thermo-hydraulic constraints are first determined. Tube length and system pressure are selected and heat load is specified.

1. Critical heat flux is determined using the Lowdermilk correlation (Ref. 20) modified to account for varied subcooling, after Rousar (Ref. 19). A safety factor of 1.3 is applied to CHF.

$$G_{crit} = \frac{90\left[\frac{D^{.05}L^{.15}\ q''}{1077}\right]^2 + \left[\frac{5.2\,q''\,L\,(t+r)/r}{D\,c_p}\right]}{(T_{sat} - T_{in})} \qquad (7a)$$

* Note: The procedure of Saha and Zuber may be substituted here to predict CHF on a more theoretical basis. See Ref. 54.

2. Functional dependencies among variables are established by conservation of energy in the tube.

$$\Delta T_{1-2} = \frac{4\,q''\,L\,(t+r)/r}{\pi\,G\,D\,c_p} \qquad (4a)$$

3. The pumping power constraint is next established.

$$W_p = \frac{\Delta p}{\rho\,c_p\,\Delta T_{1-2}} \leq .02 \qquad (11)$$

The limit of 2% is a soft constraint, and may be exceeded if necessary for successful divertor operation.

4. The existence of subcooled boiling in the tube is evaluated using the Rohsenow-Bergles correlation for onset of nucleate boiling in water.

$$G = \frac{4\, q''\, L\, (r+t)/r}{\pi\, D\, c_p} \left[\frac{1}{(T_{sat}-T_{in}) - q''/h + \Delta T_{ONB}} \right] \quad (1)$$

with:

$$h = .023 \frac{k}{D} \left(\frac{G\, D}{\mu_b}\right)^{.8} \left(\frac{c_p \mu_b}{k}\right)^{.4} \left(\frac{\mu_w}{\mu_b}\right)^{.14} \quad (2)$$

$$\Delta T_{ONB} = \left[\frac{q''}{15.60\, p^{1.156}} \right]^{.435\, p^{.0234}} \quad (3)$$

5. If G is greater than the right hand side of equation 1, the pressure drop, Δp, is determined using the conventional Darcy-Weisbach approach with a viscosity correction for non-isothermal flow.

$$\Delta p_{nonb} = \frac{f\, L\, G^2}{2\, D\, \rho\, g_c} = \frac{.184\, \mu_b^{.2}\, L\, G^{1.8}}{2\, D^{1.2}\, \rho\, g_c} \left(\frac{\mu_w}{\mu_b}\right)^{.25} \quad (8,9)$$

* Note: The nature of this viscosity correction factor needs further refinement for the non-uniform temperature conditions found in the divertor target. See Ref. 56.

6. If G is less than the right hand side of equation 1, the location of ONB must be determined and the Mendler procedure for determining subcooled boiling Δp employed over the subcooled boiling length.

$$\Delta p_{scb} = \frac{G^2}{2\, g_c\, D} \int_{L_1}^{L_2} f_{iso} \left(\frac{f}{f_{iso}}\right)\left(\frac{1}{\rho_b}\right) dz \quad (8a)$$

with:

$$\frac{f}{f_{iso}} = (1 - .0025\, \Delta T_{J-L}) \left[1 + .76 (G/10^6)^{-2/3} \left(1 - \frac{\Delta T_{J-L}}{.766 (q''/h)}\right)\right] \quad (8b)$$

$$\Delta T_{J-L} = T_{sat} - T_{in} - \frac{4\, q''\, L\, (t+r)/r}{\pi G\, c_p\, D} + \frac{60\, (q''/10^6)^{\frac{1}{4}}}{\exp(p/900)} \quad (8c)$$

h is given in equation 2.

7. Equations 7, and 11 constitute the principal thermohydraulic constraints.

8. Thermo-mechanical constraints are next imposed. The sputtering erosion rate is determined.

$$\frac{\Delta t}{\Delta \tau} = \sum_i S_i J_i C \left(\frac{M}{\rho N_A}\right) \quad (13)$$

9. Adding a hoop stress constraint gives a minimum wall thickness requirement.

$$t \geq \frac{pr}{S_{mt} - p} + \Delta\tau S_i J_i C \left(\frac{M}{\rho N_A}\right) \quad (13a)$$

10. The fatigue constraint is found from the following equation, where $\Delta\epsilon_{max}$ varies with target life.

$$t \leq \frac{2\, k\, (1-\nu)}{\alpha\, q''} \Delta\epsilon_{max} \quad (26)$$

11. Solving 13a and 26 simultaneously for the design heat load determines the optimum life and wall thickness for the material. Varying radius changes the maximum life of the material. Fixing life provides an upper limit on tube radius.

12. Temperature limits are checked. These may pose an upper limit on ΔT_{1-2}.

$$T_{melt} - T_{in} \geq \frac{q''(r+t)}{k} \ln(1+t/r) + q''/h + \left(\frac{r+t}{r}\right) 2Lq''/\pi G c_p r \quad (27)$$

$$T_{corr} - T_{in} \geq q''/h + \left(\frac{r+t}{r}\right) 2Lq''/\pi G c_p r \quad (28)$$

13. If temperature limits do not restrict the design

window, limit practical inner radius size to 2 mm.

14. The fatigue-sputter life limits, the temperature limits, and the minimum tube radius limit constitute the thermo-mechanical design window constraints.

15. For flat plates with circular internal channels, the above procedure is also applicable, except that the quantity (t+r)/r does not vary as the plasma-facing thickness varies.

16. Protective tile which can expand axially but cannot bow, and which is not bonded to the substrate is subject to the same thermo-mechanical constraints as above. For the tile mechanically bonded to the substrate, the analysis of equations 33 to 40 provides the expected strain range for the material. Thickness may be varied until the expected sputtering life just equals the fatigue life corresponding to the strain range at that thickness. This provides the optimum life and thickness for the protective tile bonded to the substrate.

17. Material properties are input for average temperatures, except that mechanical limits are chosen to be conservative over the temperature range of interest. Fluid properties are evaluated at the bulk or wall temperatures using the fits of empirical data in Ref. 23.